Czech Technical University in Prague

Faculty of Electrical Engineering
Department of Circuit Theory

Image processing pipelines for analysis of clinical human MRI

Doctoral thesis

Ing. David Kala

Supervisor: Prof. Ing. Roman Čmejla, CSc.
Supervisor specialist: Prof. MUDr. Jakub Otáhal, Ph.D.
Branch of study: 2602V013 - Electrical Engineering Theory
Study program: P2612 - Electrical Engineering and Information Technology

Prague, October 2022

Abstract:
Magnetic resonance imaging (MRI) plays an increasingly important role in the study of brain pathologies as it allows in-vivo, non-invasive characterization of structural and functional alterations of the brain tissue. With routine usage of advanced MRI techniques during clinical examinations, high demand for reliable tools for processing and analysis of MRI data has emerged. This thesis is focused on three tasks for analysis of clinical MRI; 1) detection of lesion of cerebral ischemia, 2) assessment of blood-brain barrier (BBB) disruption, and 3) analysis of longitudinal variations in white matter neuronal tracts after cerebral ischemia.

Detection of tissue affected by cerebral ischemia is a crucial step in the analysis of the relationship between structural and (dys-)functional properties of the post-ischemic brain. As manual delineation of the ischemic lesion (the current golden standard) is a tedious and time-consuming task that is heavily biased due to a high level of subjectivity, one goal of this thesis is to develop a reliable, unbiased, semi-automated algorithm that will assist during the delineation process. The performance of the developed algorithm was tested with resulting 94% sensitivity and 70% precision.

BBB impairment plays an important role in the pathophysiology of several brain diseases, however, its exact effect on clinical outcome is still not clear. A novel algorithm for analysis of BBB disruption from contrast MRI was developed and used in our clinical study. The results provide valuable insight into the relationship between BBB impairment and other post-ischemic pathophysiological processes in the brain.

The third algorithm pipeline was tailored for the analysis of variations in neuronal tracts. Such changes show different aspects of brain processes and thus provide additional information to the global description of brain pathologies. The proposed algorithm was tested on human MRI and further used on artificially modified data to explore its behavior in non-standard conditions of brain pathologies.

Keywords: MRI, image analysis, cerebral ischemia, blood-brain barrier, tractography

Abstrakt:

Magnetická resonance (MRI) hraje v současné době klíčovou roli při studiu mozkových onemocnění, jelikož umožňuje neinvazivně in-vivo popsat strukturální a funkční změny mozkové tkáně. S nástupem pokročilých MRI měření v běžné klinické praxi se zvýšila poptávka po spolehlivých nástrojích na zpracování a analýzu MRI dat. Tato práce se zabývá třemi úkoly při analýze klinických MRI mozku; 1) detekce léze cévní mozkové příhody (CMP), 2) hodnocení poškození hematoencefalické bariery (HEB) a 3) analýzou časových změn nervových traktů.

Detekce léze CMP je zásadní krok při analýze funkčních vlastností mozku po CMP. Manuální označování léze (současný zlatý standard) je obtížný a časově náročný proces, který je navíc zatížen vysokou mírou subjektivity. Jedním z cílů této práce je vytvořit spolehlivý, objektivní, semi-automatický algoritmus schopný usnadnit manuální značení léze. Vyvinutý algoritmus byl testován na reálných datech a dosáhl 94% sensitivity a 70% přesnosti.

Druhý vyvinutý algoritmus byl navržený pro detekci poškození HEB, které hraje důležitou roli v patofyziologii mozkových onemocnění. Navržený algoritmus byl použit v naší klinické studii, kde poskytl cenné informace o vztahu poškození HEB k dalším procesům probíhajícím v mozku po CMP.

Třetí algoritmus vyvinutý v této práci slouží k sledování změn nervových traktů. Tyto změny ukazují procesy v mozku pod jiným úhlem než běžné klinické snímky, čímž poskytují cenné doplnění globálního pohledu na mozkové patologie. Vyvinutý algoritmus byl použit na reálných lidských MRI datech a rovněž otestován na uměle modifikovaných datech s cílem ověřit chování algoritmu v případě nestandartních situací mozkových patologií.

Klíčová slova: MRI, analýza obrazu, cévní mozková příhoda, hematoencefalická bariera, traktografie

Declaration

Hereby I declare, that this thesis entitled *Image processing pipelines for analysis of clinical human MRI* is my original work. All sources used in this work are listed in the end and are cited within the text itself.

In Prague …… ……

Ing. David Kala

Acknowledgment

It is a great pleasure to thank my supervisor Jakub Otáhal for all his advice and guidance. I would also like to thank other members of our research group from the Institute of Physiology CAS, namely Přemysl Jiruška, Jan Svoboda, Antonín Pošusta, Jan Kudláček, and Jan Chvojka for the friendly and inspirational working atmosphere. I thank collaborators from Motol Hospital for the acquisition of clinical MRI data, namely Petr Marusič, Aleš Tomek, Martin Kynčl, Vlastimil Šulc, Petr Jánský, Anna Olšerová, and Jan Šadna and collaborators from the Department of Circuit Theory, Czech Technical University, namely Roman Čmejla, Radek Janča and Petr Ježdík for their indispensable consultations in the matter of data analysis. And finally, I would like to thank my alma mater Czech Technical University for the opportunity.

The studies described in this thesis were supported by grant project no. 15-33115A from Czech Health Research Council, by project OPPK BrainView CZ.2.16/3.1.00/21544, by the Czech-BioImaging large RI project (LM2015062 funded by MEYS CR), by SGS15/198/OHK3/3T/13 and SGS18/137/OHK3/2T/13.

"The Universe is under no obligation to make sense to you"

Neil deGrasse Tyson

Table of contents

DECLARATION 4
ACKNOWLEDGMENT 5
TABLE OF CONTENTS 6
1. INTRODUCTION 8
Aim of the study 10
Structure of the thesis 10
2. GENERAL BACKGROUND 12
2.1. PATHOPHYSIOLOGY OF CEREBRAL ISCHEMIA 12
2.2. COMMON MRI SEQUENCES 15
2.3. TIME DEVELOPMENT OF STROKE MRI IMAGE 20
2.4. STATISTICS 21
3. DETECTION OF THE ISCHEMIC LESION FROM FLAIR AND DWI MRI SCANS 22
3.1. METHODS 23
3.2. RESULTS 30
3.2.1. Algorithm performance evaluation 31
3.2.2. Clinical study 1 - Volumetric analysis of the ischemic lesion 31
4. ASSESSMENT OF BLOOD-BRAIN BARRIER DISRUPTION 40
4.1. THEORETICAL BACKGROUND 40
4.1.1. Blood-brain barrier 40
4.2. METHODS 41
4.3. RESULTS 46
4.3.1. Clinical study 2 - Relationship of blood-brain barrier damage and stroke 46
5. ANALYSIS OF LONGITUDINAL VARIATIONS IN WHITE MATTER NEURONAL TRACTS 51
5.1. THEORETICAL BACKGROUND 52
5.1.1. Anisotropic diffusion in brain tissue 52
5.1.2. Diffusion-weighted imaging 52
5.1.3. Diffusion parameters (metrics) 52
5.1.4. Tractography – reconstruction of white matter tracts 56
5.1.5. A simplified description of tractography algorithm 57
5.2. METHODS 60
5.2.1. Diffusion MRI data preprocessing 60
5.2.2. Calculation of diffusion metrics 62

5.2.3. Tractography *62*

5.3. RESULTS 63

5.3.1. Evaluation of pipeline behavior in pathological conditions *63*

6. DISCUSSION 74

7. CONCLUSION 78

7.1. FUTURE WORK 79

8. REFERENCES 80

A. LIST OF ABBREVIATIONS ..... A

B. LIST OF FIGURES AND TABLES C

C. AUTHOR'S PUBLICATIONS ..... E

C.1. PUBLICATIONS RELATED TO THE THESIS TOPIC ..... E

C.1.1. Journal publications ..... *E*

C.1.2. Conference and workshop publications ..... *E*

C.1.3. Preprints and extended versions ..... *F*

C.2. PUBLICATIONS NOT RELATED TO THE THESIS TOPIC ..... F

C.2.1. Journal publications ..... *F*

D. CURRICULUM VITAE ..... G

1. Introduction

Magnetic resonance imaging (MRI) plays an increasingly important role in the study of brain pathologies (e.g. cerebral ischemia, epilepsy, traumatic injuries) including neurodegenerative diseases (e.g. Alzheimer's disease, schizophrenia, dementia), as it allows in vivo non-invasive characterization of structural and functional alterations of the brain tissue raised by these conditions. It is also the only non-invasive technique that can measure diffusion processes in the brain that are closely related to underlying cell physiology and tissue microstructure. Advanced MRI techniques have become a routine part of clinical examinations for both the diagnostic process and the monitoring of disease progression. This led to high demand for reliable tools for the processing and analysis of MRI data. Our goal in this thesis is to develop a set of algorithms and tools for the analysis of clinical MR images with a focus on three separate tasks:

- **segmentation of ischemic lesion**
- **detection of disruption of the blood-brain barrier**
- **analysis of neuronal fiber tracts**

Proposed tools are designed especially for our MRI datasets of patients suffering from cerebral ischemia or/and epilepsy.

Cerebral ischemia (also called stroke) is a cerebrovascular disease triggered by insufficient blood perfusion of the brain. According to severity, size, localization, or length of the hypoxia, stroke can causes many various physical or mental disorders. Together with cancer and heart attack is stroke the third most common cause of death and the most common cause of long-term disability worldwide (strokecenter.org, cited: 2.4.2020). Nowadays, MRI together with computer tomography (CT) is the most used technique for localization and diagnosis of stroke. Detection of tissue affected by cerebral ischemia is a crucial step in the analysis of the relationship between structural and (dys-)functional properties of the post-ischemic brain (Maier, Wilms, *et al.*, 2015). As manual delineation of the ischemic lesion in MRI images (the current golden standard) is a tedious and time-consuming task, the development of automatic segmentation techniques has been intensively pursued in the last two decades (Subbanna *et al.*, 2019). One goal of this thesis is to develop a reliable, semi-automated algorithm that will assist during manual delineation of the ischemic lesion in MRI scans. The performance of the

algorithm will be tested, and the developed algorithm will be used in our clinical study on real human MRI datasets.

The blood-brain barrier (BBB) is a functional structure separating vascular and neural brain compartments. It is responsible for maintaining the osmotic homeostasis in the neural space and thus ensures normal brain activity. Impairment of the BBB is a common phenomenon following cerebral ischemia. It is caused by the disruption of the vessel wall leading to an influx of blood compartments into the neural space followed by inflammatory and edematous processes. This state is called vasogenic edema. However, BBB impairment is intensively studied in both humans and animals, its role in post-ischemic processes and effect on the outcome of the disease is still not clear.

The second goal of this thesis is to implement an algorithm able to detect BBB disruption and assess its severity from contrast MR images. MRI with gadolinium (Gd) contrast agent can be used for the detection of BBB disruption. The contrast agent is intravenously administered before the measurement. In physiological conditions, the Gd contrast agent stays in blood vessels, however it leaks out when BBB is disrupted. In this thesis, the algorithm using MRI with contrast agent for detection of BBB impairment will be implemented and used in a clinical study on real human data. Moreover, its results will help in our future studies to describe the relationship between BBB impairment and other pathophysiological processes in the brain.

Diffusion-weighted MRI is an approach that can reveal underlying cell physiology and tissue microstructure. Brain tissue can be described by several parameters that represent the strength and directionality of diffusion of water molecules through the brain. Diffusion parameters can then serve for the description of brain tissues as well as for the identification of brain pathologies. Moreover, by following diffusion gradients white matter neuronal tracts can be reconstructed and their variability during or after brain pathologies can be analyzed. Both approaches are potent tools for the study of brain pathophysiology.

The last goal of this thesis is to implement a complex algorithm pipeline for diffusion MRI data preprocessing, reconstruction of white matter tracts, and for calculation of diffusion parameters along reconstructed tracts. The performance of the proposed pipeline will be tested on real human data.

Aim of the study

The aim of this thesis is to develop three separate pipelines of algorithms for **detection of lesion of cerebral ischemia, assessment of blood-brain barrier disruption, and for analysis of longitudinal variations in white matter neuronal tracts** from multimodal 3D MRI human scans and to apply developed pipeline to a dataset of patients hospitalized with cerebral ischemia.

Structure of the thesis

In the first chapter of the thesis, the *General background,* common theoretical information, and introduction into the pathophysiology of cerebral ischemia are summarized together with the current state of the art of its typical MRI examination protocols. The thesis further continues with three chapters, each dealing with a single algorithm pipeline developed here for a specific task. Besides a description of the developed algorithm, each chapter contains its own introduction to the topic and aditional theoretical background for the full understanding of the problem.

The first algorithm developed in this thesis designed for *Detection of the ischemic lesion from FLAIR and DWI MRI scans* is introduced in chapter 3. The algorithm itself is described in *Methods* (chapter 3.1) and its performance is tested in *Results* (chapter 3.2). Moreover, our algorithm was used in a clinical study that is fully described in subchapter 3.2.2.

The second algorithm, designed in this thesis for the *Assessment of blood-brain barrier disruption* is described in chapter 4. The *Theoretical background* of the anatomy and function of BBB is reviewed in chapter 4.1 followed by a description of the proposed algorithm in *Methods* (chapter 4.2) and application of the algorithm in a clinical study in *Results* (chapter 4.3).

The last fifth chapter, *Analysis of longitudinal variations in white matter neuronal tracts*, documents a pipeline tailored for segmentation and analysis of neuronal tracts. It discusses the physical principles of diffusion MRI, different approaches to tract reconstruction, and shows a simplified description of the used tractography approach in chapter 5.1. The body of the pipeline is shown in *Methods* (chapter 5.2) and consists of three parts; DWI processing in chapter 5.2.1, calculation of diffusion parameters in chapter 5.2.2, and tractography in chapter 5.2.3. The pipeline was then tested on artificially modified data to evaluate its behavior in non-standard conditions of brain pathology in *Results* (chapter 5.3) and based on this evaluation a proper interpretation of the results was suggested in chapters 5.3.1.

All three main parts of the thesis (three designed algorithms) are discussed together in the *Discussion* and summarized in the *Conclusion* where the *Future work* is also outlined.

2. General background

In this chapter, the general theoretical background common to all three tasks of the thesis is described. The chapter explains the pathophysiology of cerebral ischemia, its causes and consequences, MRI sequences commonly used for clinical examination of the ischemia, and image representation of the affected tissue in those sequences together with its time profile.

2.1. Pathophysiology of cerebral ischemia

Cerebral ischemia (stroke) is a disease that can affect human brain tissue by many different effects varying between individual patients. The pathophysiology of the disease and several related effects are described in this subchapter.

Cerebral ischemia or stroke is a situation when blood perfusion in the brain is dramatically decreased or suspended. According to severity, size, localization, or length of ischemia stroke can cause various physical or mental alterations. Together with cancer and heart attack, stroke is the third most common cause of death and the most common cause of long-term disability worldwide (strokecenter.org, cited: 2.4.2020).

Cerebral blood flow can be reduced due to several reasons finally leading to cerebral ischemia. According to the cause of blood flow reduction and scope of the resulting ischemia, stroke can be divided into several subtypes. Global cerebral ischemia is a pathophysiological state when the blood flow is reduced globally in the whole brain. It is caused mostly by heart failure or suffocation. On the other hand, focal cerebral ischemia is a state when the blood flow is reduced only in part of the brain. Mostly by blockade of one vessel (and its subsequent branches) by a blood clot (columbianeurosurgery.org, cited: 2.4.2020). Another type, hemorrhagic stroke, has a different origin. It is caused by the weakening of the wall of the blood vessel followed by its rupture. This type of stroke can cause massive bleeding into the brain or subarachnoid space (space between the brain and the skull). (stroke.org, cited 16.9.2020)

In this thesis, only patients with focal cerebral ischemia were analyzed.

Brain tissue needs constant access to oxygen for its metabolism.

Brain functions depend on constant energy supply which is provided by glucose and oxygen. A sudden hindrance of cerebral blood flow (CBF) affects energy metabolism pathways namely glycolysis and phosphorylation. Cerebral ischemia is a condition when the blood flow in the brain (or part of it) is significantly lowered and cannot provide enough oxygen for brain metabolism. Neurons can maintain their proper functions for approximately 2-3 minutes in total anoxia (no oxygen influx) (Srinivasan *et al.*, 2006). After this time, lack of oxygen leads to depletion of energy storages of neurons and consequent suspension of sodium pumps (Na^+/K^+-ATPase), these are no more able to maintain the pumping of Na+ ions out of the cells and K+ into the cells, which leads to a cumulation of ions inside cells. Molecules of water start to follow increased extra->intracellular osmotic gradient across the cell membranes causing intracellular swelling called cytotoxic (or metabolic) edema (O'Brien, 1979).

Brain extracellular swelling with intact blood-brain barrier

As the extracellular volume decreases due to cytotoxic edema osmotic gradient between extracellular space and vessels emerges. Water is pulled out from the vessels into the extracellular space but without prior damage to the blood-brain barrier (O'Brien, 1979). Volume changes in tissue (swelling) are caused mainly by the absorption of water from the vessels. This combined effect is called ionic edema (Simard *et al.*, 2007).

Disruption of the blood-brain barrier

Pathological processes in neurons are followed by structural changes of the affected tissue. Mechanical extension of the vascular wall leads to impairment of tight junctions, furthermore, cells damaged by cytotoxic edema necrotize and together with consecutive inflammation contribute to the disruption of the blood-brain barrier (BBB). Many mediators have been proposed as a possible cause of BBB disruption, *including reverse pinocytosis* (Castejón, 1984), *disruption of* Ca^{2+} *signaling* (Brown and Davis, 2002), *actin polymerisation-dependent endothelial cell rounding or retraction with formation of interendothelial gaps, uncoupling of tight junctions, and enzymatic degradation of basement membrane. Also formation of interendothelial gaps with many inflammatory mediators was reported* (Ahmmed and Malik,

2005) *including mediators up-regulated in cerebral ischaemia such as thrombin* (Satpathy *et al.*, 2004). (Simard *et al.*, 2007)

Vasogenic edema – extracellular swelling with impaired blood-brain barrier

When BBB is disrupted, higher hydrostatic pressure in blood vessels pushes water into the extracellular space along with blood proteins (albumin), which causes further osmotic disruption followed by a new influx into extracellular space driven by this strengthened osmotic gradient. This kind of swelling is termed vasogenic edema. *This form of edema spreads extensively through the brain, particularly in white matter, by bulk flow along hydrostatic pressure gradients faster than it would by diffusion according to diffusion coefficients* (O'Brien, 1979).

Vasogenic edema requires preserved blood flow and blood pressure strong enough to exceed extravascular pressure increased out of normal by swelling due to cytotoxic edema and by effects of ionic edema. Without enough pressure and blood flow, there is no hydrostatic motor driving influx of fluid out of the vessels into the extracellular space and thus no extravasating proteins, which would cause further osmotic imbalance. Therefore, in ischemic infarct core with no perfusion is vasogenic edema in the early hyperacute phase of ischemia (first 6 hours) is mostly not observed. Swelling by vasogenic edema either appears after reperfusion (either physiological or as a result of post-ischemic treatment - thrombolysis or mechanical thrombectomy) or can be spread by bulk flow through brain tissue from peripheral regions with better perfusion. (Simard *et al.*, 2007)

Time profile of blood-brain barrier impairment

BBB disruption was directly detected by contrast-enhanced MRI early after reperfusion in experimental models (Abo-Ramadan *et al.*, 2009). In humans, leakage of BBB was reported two days after ischemia using MRI (Hjort *et al.*, 2008; Durukan *et al.*, 2009; Tiwari *et al.*, 2017). However, the exact time profile of the development of BBB impairment in humans wasn't still completely described (Hu *et al.*, 2017).

In our study, BBB damage was assessed in the subacute phase of ischemia (7-12 days) when all acute post-ischemic processes are finished, and perfusion restored. It is important to

understand that BBB impairment can originate in the early phases of ischemia but is not observable till later phases after reperfusion. As post-ischemic brain tissue has fast dynamics and changes quickly, the condition of the tissue measured in the subacute phase might not correspond to the same condition in which BBB was originally disrupted.

2.2. Common MRI sequences

Magnetic resonance imaging (MRI) is a non-invasive technique commonly used for the examination of (post-)stroke brain tissue and related phenomena as edema, gliosis, hemorrhage, or blood-brain barrier breakdown. Various MRI sequences have various sensitivity to different tissue types or phenomena in the brain (e.g. ischemia, hemorrhage, blood vessels, cerebrospinal fluid, etc.). By combining information from a wider range of MRI sequences larger spectrum of information about patients and a better global view is achieved. Description of commonly used MRI sequences, their role in the visualization of stroke-affected tissue, and the time profile of its images during the disease progression is described in this subchapter. Exact MRI protocols and their parameters used in our clinical studies are described more in detail in individual chapters. This chapter refers to (Stark and Bradley, 1999; Mitchell and Cohen, 2004; Hagmann *et al.*, 2006; and radiopedia.org, cited: 3.4.2020).

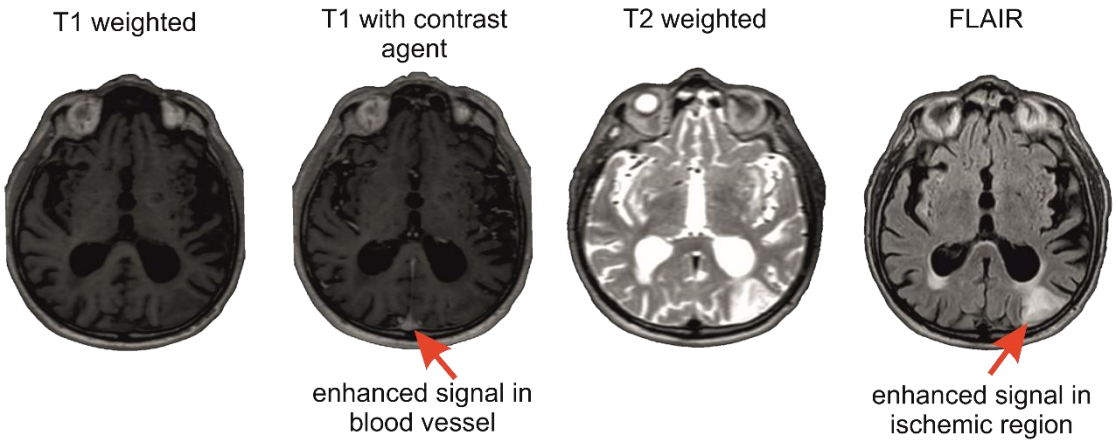

Figure 1. Four structural MRI sequences that are most commonly used for the examination of cerebral ischemia

T1 weighted image

MRI technique in general measures a reaction of hydrogen nuclei inside observed tissue to an external magnetic field (called B0) and/or external pulses. In the absence of such a field, hydrogen nuclei are in the tissue oriented randomly and the summation of their magnetic moments called the net magnetization vector is zero. When the external magnetic field is applied, nuclei became aligned within this field and the net magnetization vector became non-zero. Magnetization can be further modified by the application of other magnetic pulses, however, when the pulses are gone, magnetization tends to return to its initial state. This return is called magnetization decay or relaxation and it has various time courses based on the number of hydrogen nuclei in the tissue. Therefore, by measuring magnetization decay curves different tissues can be distinguished. Magnetization (or net magnetization vector) can be decomposed into two components, longitudinal and transversal magnetization, when the first is parallel and the second perpendicular to the external magnetic field.

T1 weighted image (T1w) MRI protocol is based on measuring the decay of the longitudinal magnetization after application of the 90° excitation radiofrequency pulse (RF pulse). The speed of the decay is defined by the T1 relaxation time constant. In simple terms, it describes how quickly protons in measured tissue recover from the direction of RF pulse to its ground state in direction of B0 (external magnetic field) magnetization. Objects in the T1w image are differentiated based on varying T1 time constants. The fastest T1 relaxation in the brain is observed in fat, therefore it appears brighter in the T1w MR image. On the other hand, water has a long T1 relaxation time and appears dark. Typical T1w MRI is shown in Figure 1.

T1 weighted image with a contrast agent

T1w image can be enhanced by adding a contrast agent. Generally, a contrast agent is a substance, that shortens the relaxation time of the tissue in which it is present and this shortening enhances the intensity of the MRI image of the corresponding tissue. In Figure 1., T1w image with contrast agent administered before the measurement into the blood is shown.

A common type of contrast agent is based on gadolinium. In this study, such a contrast agent (precisely contrast agent called Gadovist; Gd-DTPA chelate complex) was used for the detection of blood-brain barrier impairment. It is described more in detail in chapter 4.

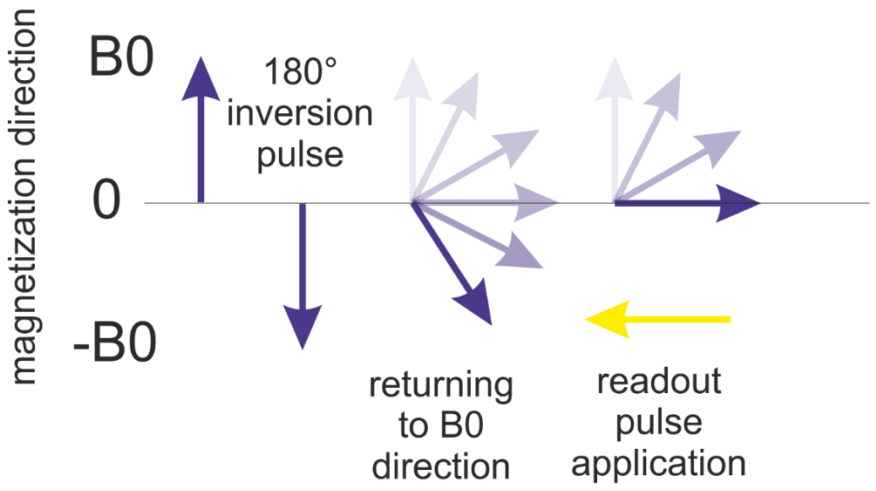

Figure 2. Scheme of inversion recovery method. The direction of protons magnetization is switched to a direction inverse to B0. Then it naturally starts to return to the B0 direction. Readout pulse is applied exactly at the moment when protons of desired tissue are in zero lateral direction and therefore is their signal omitted from resulting image

T2 weighted image

In T2 weighted (T2w) imaging, the 90° RF pulse is applied in a similar way as in the case of T1w. After application of the pulse, the main direction of hydrogen nuclei changes to transversal to the original B0 direction and they synchronize phases of their spin precession. Phase synchronization causes transversal magnetization that starts to decay in time. The time needed for the complete desynchronization is called T2 relaxation time and is defined by the T2 time constant. Water has fast T2 relaxation and therefore its T2w MR image has high intensity. In the brain, the highest intensity of T2w MRI scans is observed in the cerebrospinal fluid (as it contains the highest amount of free water). For the example of the T2w image see Figure 1.

FLAIR image

Fluid attenuation inversion recovery (FLAIR) is a member of a family of inversion recovery sequences. Inversion recovery sequences are used to selectively nullify signals from selected tissue. Additional 180° pulse which forces protons to change their direction from B0 to -B0 is applied before the 90° readout pulse. Particles tend to return to the B0 direction. Readout pulse is then applied exactly at the moment when protons of the tissue which should be nullified

reach zero points in longitudinal magnetization. The inversion recovery process is shown in Figure 2.

Fluid attenuation inversion recovery is set to remove the signal from the cerebrospinal fluid (CSF). In our protocol FLAIR is used to detect the ischemic region, which is hyperintense in FLAIR, therefore it can be easily distinguished from healthy brain tissue as is shown in Figure 1.

Diffusion-weighted imaging

Another MRI sequence commonly used in clinical practice is called diffusion-weighted imaging. It is based on the measurement of random Brownian motion of water molecules within a voxel of tissue. In the water solution, the Brownian motion is random in all directions. On the contrary, in most types of human tissue, this motion is usually prominent in a specific direction(s) due to the diffusion effect. The exact way how water molecules diffuse through the brain tissue relies on many aspects. In simplified terms, tissue with strong diffusion in a specific direction has a lower diffusion-weighted imaging signal in the comparison with homogenous tissue where water diffuses randomly in all directions. A diffusion-weighted image is a useful sequence for the detection of cerebral ischemia or identification of white matter neuron tracts.

A diffusion-weighted image consists of several T2w 3D scans from which the final information is reconstructed. Typical diffusion set contains one T2 volume acquired with zero *b* factor (parameter of MRI scan indicating the strength of diffusion effects on the tissue) and several volumes of the same subject with an extra added magnetic gradient from different directions as is shown in Figure 3. From the theory, only three additional volumes (called directions) have to be measured to reconstruct the diffusion image, however, in practice, at least fifteen directions are acquired to obtain reliable results (Jensen and Helpern, 2010).

Figure 3 also shows the three most common metrics that can be calculated from the diffusion-weighted images (for a detailed description of metric calculation see chapter 5.1). **Isotropic diffusion map (called DWI)** indicates the prominent direction of the diffusion. DWI has low values in tissue with free diffusion such as brain ventricles (filled with cerebrospinal fluid) and increases its intensity with stronger diffusion restriction. Therefore, DWI is bright in (post-) ischemic tissue.

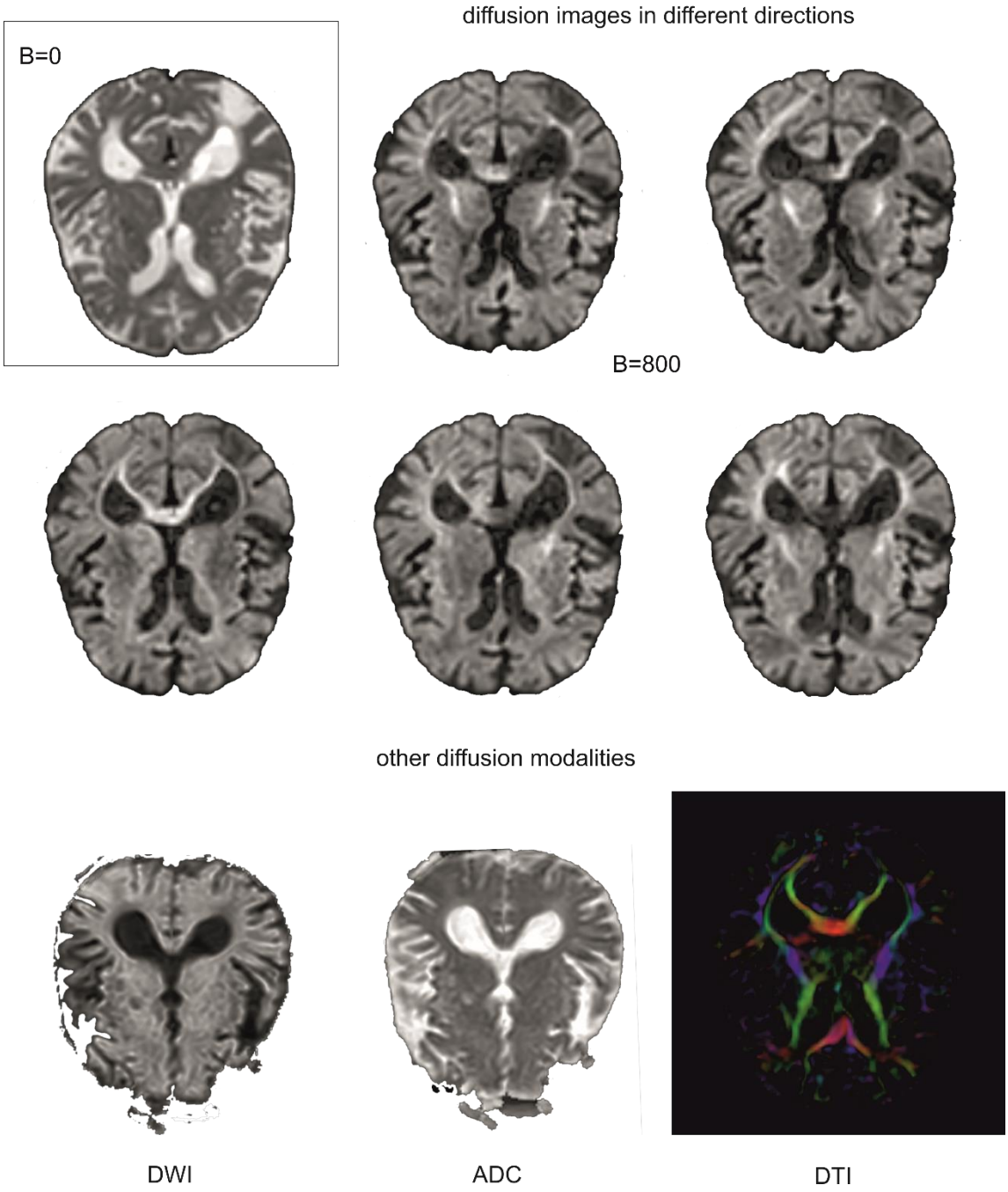

Figure 3. Diffusion-weighted image and its metrics. Above, one image with a *b* value set to zero and five with *b*=800 with a different phase direction is shown. The difference between directions is seen in the bottom corners of both ventricles. Part bellow shows three metrics reconstructed from the diffusion-weighted image. Isotropic diffusion map DWI, ADC correlates showing the magnitude of the diffusion and DTI demonstrates the direction of white matter neuron fibers

Apparent diffusion coefficient (ADC) is another commonly used metric of diffusion-weighted image. It shows the magnitude of the diffusion in its prominent direction. ADC is bright in regions with free diffusion (such as CSF) and dark where diffusion is restricted, i.e. has inverse behavior as DWI. It has also a different time curve than DWI during the development of

cerebral ischemia. Therefore, it is possible to determine the age of the ischemia by comparing DWI and ADC images.

The direction and strength of the diffusion can be expressed together in the form of a tensor. Such image is called **diffusion tensor image (DTI)** and is used in tractography, a mathematical operation used for the identification of white matter neuronal tracts. Tractography and other diffusion metrics and their calculation will be described in more detail in chapter 5.1.

2.3. Time development of stroke MRI image

Time development of the stroke in human patients is divided into several phases (originally defined in (Allen *et al.*, 2012):

- early hyperacute 0 to 6 hours
- late hyperacute 6 to 24 hours
- acute 24 hours to 1 week
- subacute 1 to 3 weeks
- chronic more than 3 weeks

As post-stroke changes in the brain progress in time, their MRI image varies simultaneously. Time development of post-stroke MR image in FLAIR, ADC, and DWI in human patients is described in this subchapter.

FLAIR, DWI, and ADC are the commonly used MRI sequences for the identification of ischemic lesion (tissue affected by the stroke). FLAIR is a sequence, that is sensitive to structural changes in tissue – extracellular swelling, gliosis, etc. On the other hand, DWI and ADC are sensitive primarily to diffusion changes in the tissue – intracellular swelling, restricted diffusion, etc. The ischemic lesion in FLAIR and DWI (both are based on T2 sequence) appears hyperintense in early hours after ischemia, on the contrary, in ADC is lesion hypointense.

T2 and FLAIR were reported to be significantly higher than control values for all time periods of the stroke.

DWI progressively increases during days 1-4, with consecutive stabilization (measured up to day 72) (Lansberg *et al.*, 2001). Lansberg *et al.* reported a progressive increase of DWI from

symptom onset up to 8-14 days when it reaches its maximum and starts to slowly decrease. (Lansberg *et al.*, 2001) The initial increase of DWI is according to Srinivasan *et. al* result of restricted diffusion (cytotoxic edema) however its prolongation after 14 days is caused due to T2 shine-through (increased intensity of T2). (Srinivasan *et al.*, 2006)

ADC hypointensity is observed as early as 30 min after stroke insult in humans. *The ADC continues to decrease further and reaches a nadir at approximately 3–5 days*. Then slowly progressively increases to reach pseudo-normal values approximately 7 days after stroke. (Srinivasan *et al.*, 2006)

2.4. Statistics

Following formulas were used for the evaluation of sensitivity and precision of the proposed method in chapter 3.2.

$$Sensitivity = \frac{TP}{P} \quad \text{(Equation 1)}$$

$$Precision = \frac{TP}{TP + FP} \quad \text{(Equation 2)}$$

Where P (positive) is the number of voxels labeled as lesional by manual delineation. TP (true positive) is the number of voxels correctly labeled as lesional by the proposed algorithm and FP (false positive) is the number of voxels that were labeled (falsely) as lesional by the algorithm but not by manual delineation.

3. Detection of the ischemic lesion from FLAIR and DWI MRI scans

Detection of tissue affected by cerebral ischemia (ischemic lesion segmentation) is a crucial step in the analysis of the relationship between structural and (dys-)functional properties of the (post-)ischemic brain (Maier, Wilms, *et al.*, 2015). Magnetic resonance imaging (MRI) is the most used technique for the identification of ischemic lesion nowadays. Because the golden standard of lesion segmentation, the manual delineation, is a time consuming and tedious task, that suffers from subjective differences, due to substantial individual variations in localization, size, and shape of the ischemic lesion, the development of automatic segmentation technique has been intensively pursued in last two decades. (Subbanna *et al.*, 2019)

Many algorithms for lesion segmentation were developed in the last years, using a variety of image analysis techniques and combinations of MRI sequences. For example, multiparameter unsupervised k-means (Jacobs *et al.*, 2000), region growing technique (Dastidar *et al.*, 2000), expectation-maximization algorithm (Rose *et al.*, 2004), probabilistic neural network (Bagher-Ebadian *et al.*, 2011), random forest algorithm on multimodal MRI (Mitra *et al.*, 2014), extra tree forest technique (Maier, Wilms, *et al.*, 2015), deep learning (Stier *et al.*, 2015), combination of supervised and unsupervised classification (Guo *et al.*, 2015), voxel-based Bayes classification (Griffis, Allendorfer and Szaflarski, 2016), random Markov fields (Subbanna *et al.*, 2019) and other algorithm were used. Automatic lesion segmentation was also the focal point of the Ischemic Stroke Lesion Segmentation Challenge (ISLES) in the years 2015-2017 (Maier *et al.*, 2017).

Most of the approaches were compared in Rekik's (Rekik *et al.*, 2012) and lately dated Maier's (Maier, Schröder, *et al.*, 2015) reviews. And also compared with the manual golden standard in (Ito, Kim and Liew, 2018). As a summary, some approaches achieved good results in a specific combination of conditions (specific dataset, lesion type, or the age of lesion), however, none of them performed stable segmentation across all variants of ischemic lesions. Thus, in the case of the use of currently available automatic algorithms, Ito suggests carefully tuning the algorithm precisely for conditions of an exact dataset and always visually controlling the results (Ito, Kim and Liew, 2018).

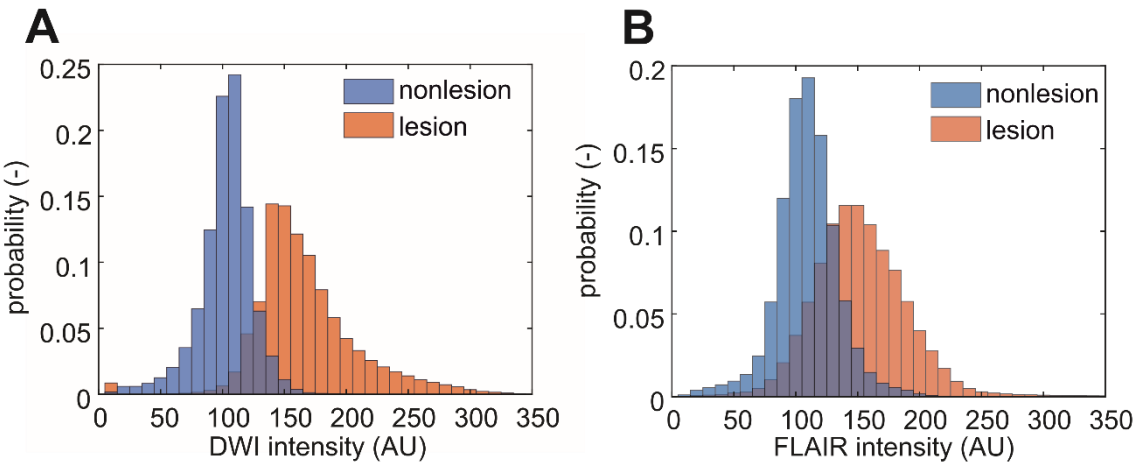

Figure 4. Mean probability histogram of intensities of lesional (ischemic) and non-lesional tissue in (A) DWI and (B) FLAIR MRI in 60 patients. Distributions of tissues are partly overlapped which complicates their separability by simple thresholding technique. Lesion was manually labeled for purpose of this comparison in 60 patients from our dataset

Based on those facts, we have decided to develop our own semi-automatic approach assisting during the manual delineation, instead of using a strictly automatic one. This approach is still time-consuming (although less than fully manual delineation) and still needs a skilled observer, however, obtained results are very reliable.

The proposed semi-automated approach of lesion detection as a pipeline of algorithm steps is described in this chapter. The approach is tested on real human MRI data and results are compared with the golden standard (full manual delineation). Moreover, the proposed pipeline was also proven useful in our clinical study that is described at the end of this chapter.

3.1. Methods

This chapter describes an algorithm pipeline developed as part of this thesis for the detection of the tissue affected by cerebral ischemia from FLAIR and DWI MRI scans.

Post-ischemic lesional changes manifest as hyperintensity in DWI (diffusion alteration due to edema) or FLAIR (structural changes of the tissue) MRI sequences (for more details see chapter 2.3). The idea behind the proposed algorithm is to separate those hyperintensities from the rest of the image as a mask of pathology.

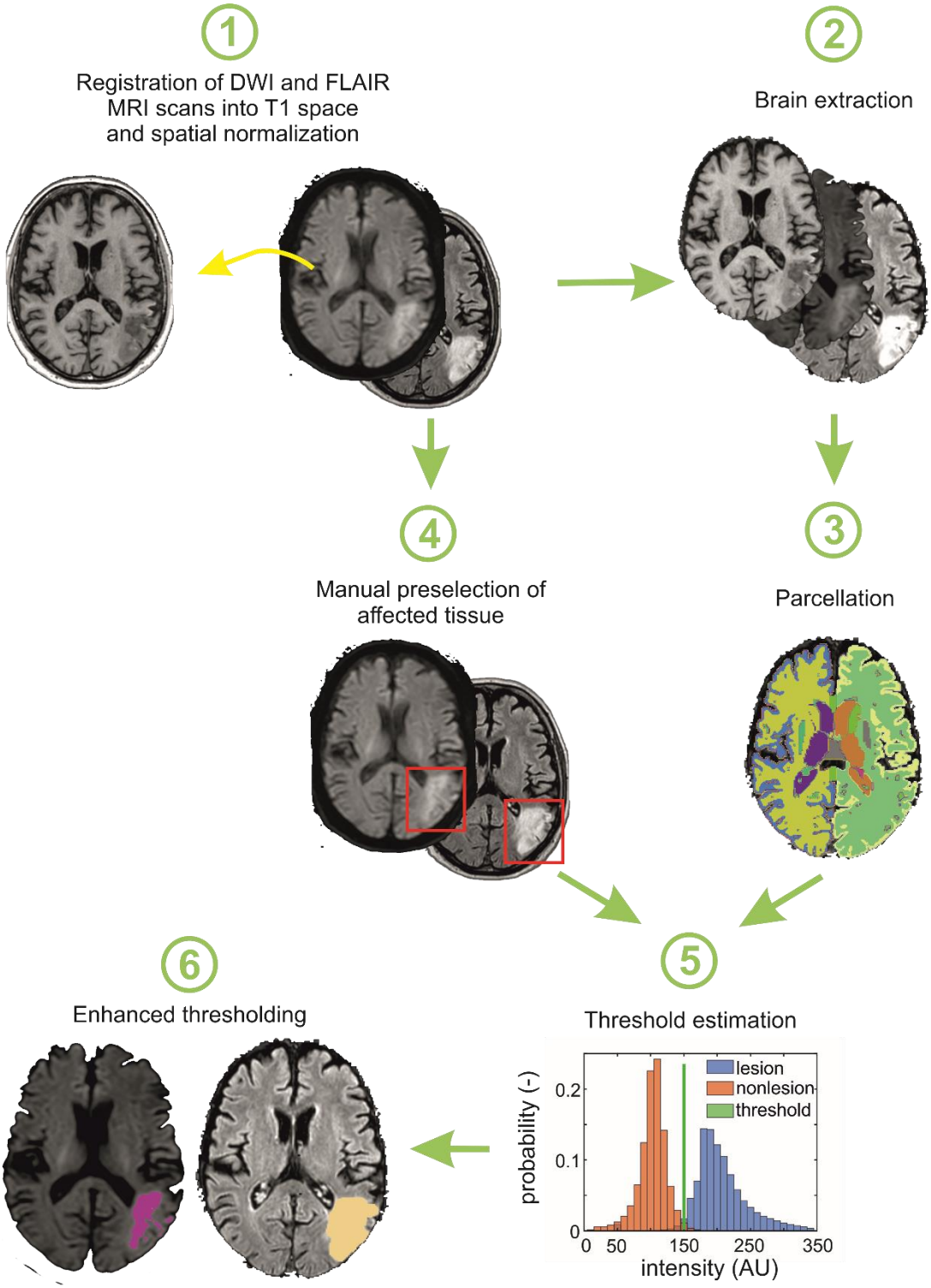

Figure 5. Scheme of the proposed algorithm for detection of the ischemic lesion from FLAIR (fluid attenuation inversion recovery) and DWI (diffusion-weighted isotropic maps) MRI

The image segmentation technique called basic thresholding uses a single threshold value to divide the segmented image into two parts; with image intensities lower or higher than the threshold. In an ideal scenario, intensity distributions of phenomena that we would like to separate (in our case lesional and non-lesional tissue) are far from each other with no overlapping and therefore can be easily separated by a single threshold value. However, in real brain MRI scans the distributions of lesional and non-lesional tissues are close to each other and often partly overlaps (see Figure 4). To overcome this problem and improve the efficiency of tissue separation, we propose the Enhanced thresholding technique in this thesis. The developed algorithm pipeline consists of 6 steps as is shown in Figure 5. Description of steps of proposed algorithm pipeline and comparison of its results with manual delineation (golden standard for stroke lesion detection) is presented in this chapter.

Step 1. - Image registration and spatial normalization

Image registration is a technique where all MRI images (modalities) are aligned into one common space. Voxels in one image are aligned with corresponding voxels in other images and thus multi-image comparison or multi-modality analysis can be reliably performed. Matlab SPM12 toolbox (Ashburner and Friston, 2005) is used for registration in this thesis. All MRI images (modalities) for single patients are coregistered with their T1w image – i.e into anatomical space. Image registration quality is then visually checked.

Spatial normalization is a preprocessing step, where all images of all subjects are registered into one general atlas space. The aim of the normalization is to reduce intersubjective variability of brain size and shape by deforming human brain scans so one location in one subject's brain corresponds to the same location in another subject's brain scan. Matlab SPM12 toolbox Normalization (Ashburner and Friston, 2005) to MNI (Montreal Neurological Institute) coordinate system is used in this thesis.

Step 2. - Brain extraction

Brain extraction (or skull-stripping) is a technique that removes all voxels corresponding to non-brain tissue i.e. skull, skin, muscles, or eyeballs. The result is an image containing only the brain tissue. Many software and tools provide brain extraction techniques e.g. 3D Slicer, FSL, Freesurfer. In this thesis SPM12 segmentation (Ashburner and Friston, 2005) is used because

of a good combination of quality and computation time. This tool is able to segment the image based on a mixture of Gaussians and nonlinear registration with tissue probability maps into several regions corresponding to grey matter (GM), white matter (WM), cerebrospinal fluid (CSF), bone, air, and background. The final segmentation mask of brain only (skull-stripped) tissue is obtained as the unification of grey, white matter, and CSF. The demonstration of segmentation and brain extraction is shown in Figure 6.

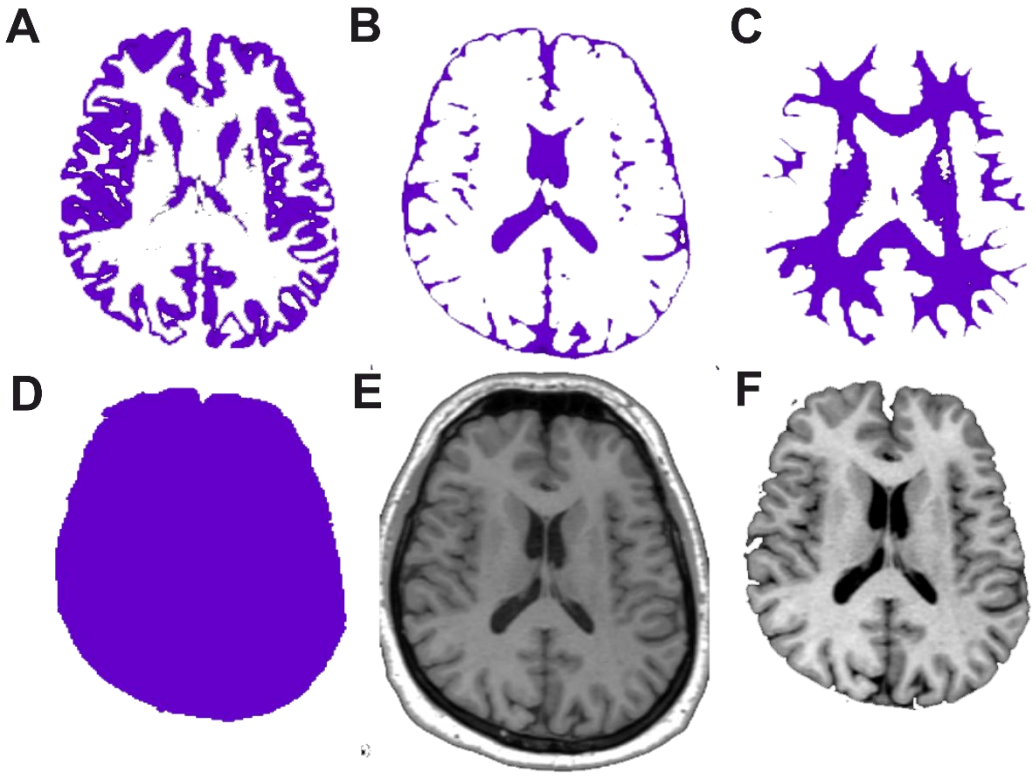

Figure 6. Demonstration of segmentation and brain extraction technique. (A-C) show maps of grey matter, white matter, and cerebrospinal fluid, respectively, obtained by SPM tissue segmentation. (D) A mask of the brain tissue is created as the unification of A, B, and C. (E) shows original T1w. (F) is the final image after brain extraction containing only the brain tissue

Step 3. - Brain image parcellation

Brain segmentation provided by the SPM tool (see above) divides MRI images into five parts (grey/white matter, cerebrospinal fluid, bone, air, and background). Although such coarse partition is sufficient for brain extraction, more detailed segmentation is necessary for the identification of other brain structures. For detailed segmentation (called parcellation) freely accessible software Freesurfer (http://surfer.nmr.mgh.harvard.edu/) is used in this thesis.

Freesurfer software is able to automatically parcellate brain volume into many anatomical segments according to the chosen atlas. It operates in two-step parcellation; subcortical and cortical parcellation. For subcortical parcellation atlas with 37 structures are used in our pipeline. For cortical parcellation, Desikan-Killiany atlas (Desikan *et al.*, 2006) with 64 cortical structures is used (see Figure 7). Desikan-Killiany atlas can segment the brain to the level of individual gyruses, therefore it provides a possibility to track neuronal fibers to/from very specific regions of the brain. Results of such parcellation can be thus used as input masks for tractography or calculation of structural/functional connectivity.

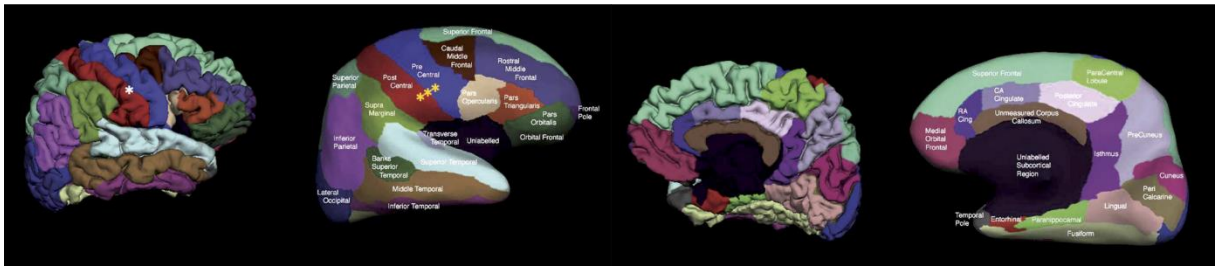

Figure 7. A precise atlas of cortical structures is used for parcellation in our pipeline. It allows tracking neuronal tracts to very specific regions of the brain. The picture was adopted from (Desikan *et al.*, 2006)

A problem occurs when we try to parcellate the brain with significant morphological changes as an effect of cerebral ischemia. When the impaired brain is significantly morphologically different than the healthy one, it does not agree with the used atlas (which was created from healthy brains) and the parcellation algorithm is not able to work properly. We have solved this problem by replacing the ischemic tissue in the T1 image with a homogenous region with intensity responding to subcortical tissue.

Deeper knowledge of spatial localization of important parts of the brain and precise position of individual functional regions of the cortex is important in further analysis of the brain such as tractography, voxel-based analysis, or most psycho-cognitive comparisons. Therefore, the inclusion of the parcellation step in the brain analysis pipeline is recommended. In our pipeline for detection of ischemic lesion, it is, however, not necessary and can be omitted, although its inclusion improves the quality of detection results.

In our proposed algorithm, parcellation is used for the selection of white or grey matter only. Other tissues as CSF, muscles, blood sinuses are masked out which further improves brain extraction described in the previous step. For a demonstration in FLAIR image see Figure 8.

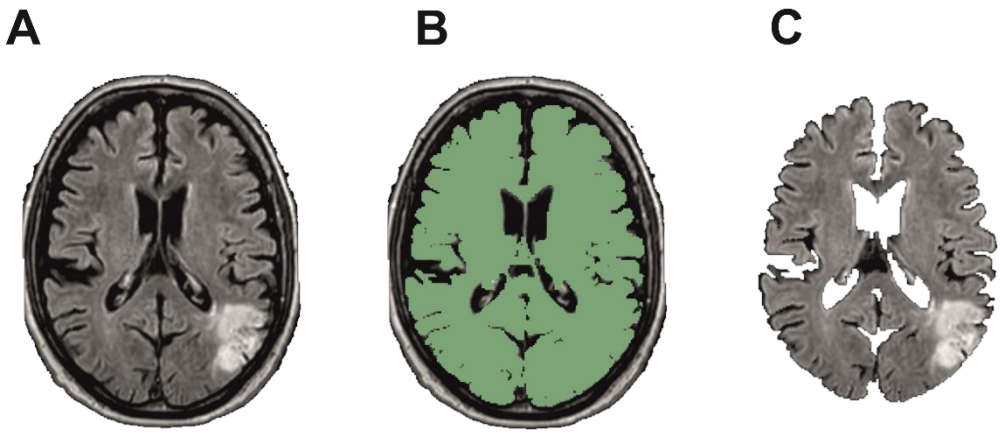

Figure 8. Usage of brain parcellation for improvement of brain extraction. (A) Raw FLAIR image, (B) the mask of gray and white matter only, and (C) extraction of only-brain tissue image

Step 4. – Manual preselection of affected tissue

Separation of healthy (non-ischemic) and ischemic lesional tissue from FLAIR and DWI using basic thresholding is problematic because the distance of MRI intensity distributions of both tissue types is either short or in worse case both distributions overlaps (see Figure 9 A). As a result of the overlapping, some brain regions are falsely labeled as lesional when basic thresholding is used.

After close inspection of overlapping parts of the distributions, we have seen that the right tale of non-lesional tissue distribution in DWI corresponds mostly to artifacts or non-brain tissue that sometimes occurs as an error of skull-stripping. In the case of FLAIR, the majority of overlapping parts belong to regions of older lesions, gliosis, or borders of ventricles. If those regions are not presented in the segmented image the distance of distributions is wider which results in lower false positivity of the whole separation. Some of those regions can be removed by brain extraction (that can be further improved by the use of brain parcellation) as described in previous steps.

To avoid the rest of the problematic voxels, only part of the brain consisting of the lesion was manually selected before thresholding as a cubic volume of interest (VOI). Distributions of image intensities in the whole brain and only in VOI are shown in Figure 9 (A) and (B), respectively. It is visible that preselection of VOI leads to shortening of the right tale of non-lesional distribution and thus to a reduction of the overlapping part of both distributions which finally results in lower false positivity of the segmentation.

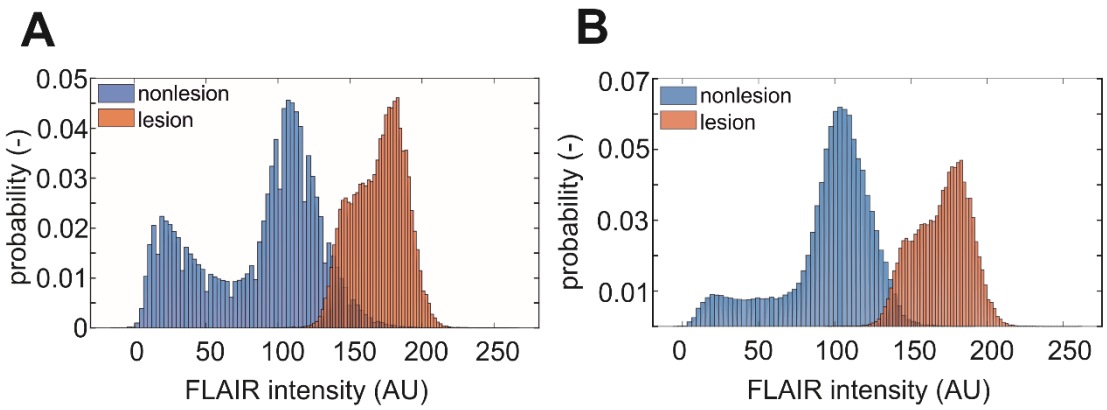

Figure 9. Distributions of MR image intensities for lesional tissue affected by cerebral ischemia and non-lesional tissue. (A) Distributions in the whole brain and (B) only in preselected VOI. Distance between distributions and the degree of their overlap have a crucial effect on the result of tissue segmentation using the thresholding technique

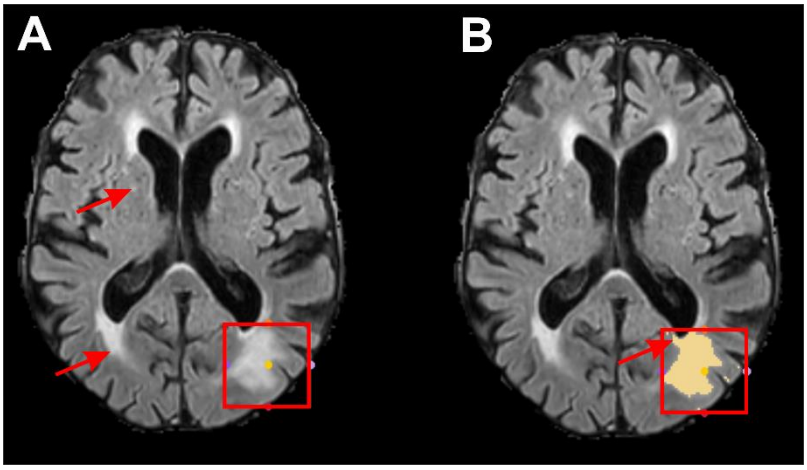

Figure 10. (A) manual preselection of part of the brain consisting of the lesion prior to thresholding to avoid false positive detection of tissue as gliosis or borders of ventricles (marked by arrows). (B) Result of thresholding after lesion preselecting. Although most false positive detections were suppressed by preselection, part of the posterior corner of the ventricle (marked by arrow) in the proximity of the lesion was not avoided. The figure shows operations in FLAIR MRI scans, the same steps are performed in DWI scans

The preselection of VOI is shown in Figure 10. Although, most problematic parts of the brain were avoided (older gliosis, ventricles, etc.), a small part of the ventricle with image intensity corresponding to overlapping parts of distributions was still false positively detected. Therefore, VOI should be selected with a special focus on the reduction of distributions overlap.

Step 5. – Threshold estimation

After selection of only brain tissue (in brain extraction and parcellation steps) and VOI with the lesion, an overlap of distributions of lesional and non-lesional image intensities is reduced and a threshold value is manually selected to separate individual types of tissue. Selection of threshold value is manually performed in freely available software 3D Slicer (http://www.slicer.org).

Step 6. – Image enhanced thresholding

The last step of the proposed pipeline is similar to basic thresholding. However, in our pipeline it is performed only in preselected volume (VOI) after all non-brain tissue is removed (by brain extraction and parcellation) and with the use of manually estimated threshold value. All steps are identical for the segmentation of FLAIR and DWI MRI sequences. An example of the results of the proposed algorithm is shown in Figure 11.

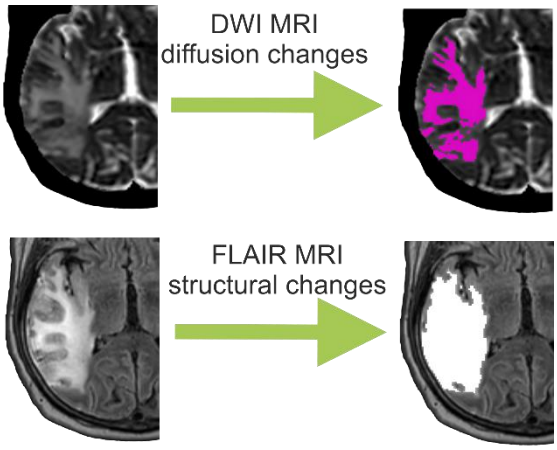

Figure 11. Resulting segmentation of ischemic lesional tissue using proposed algorithm pipeline from DWI and FLAIR MRI scans

3.2. Results

In this chapter, the performance of the developed algorithm pipeline is tested by comparing its results with the golden standard (manual delineation of the lesion). Furthermore, the proposed method is used in a clinical study and its results are presented.

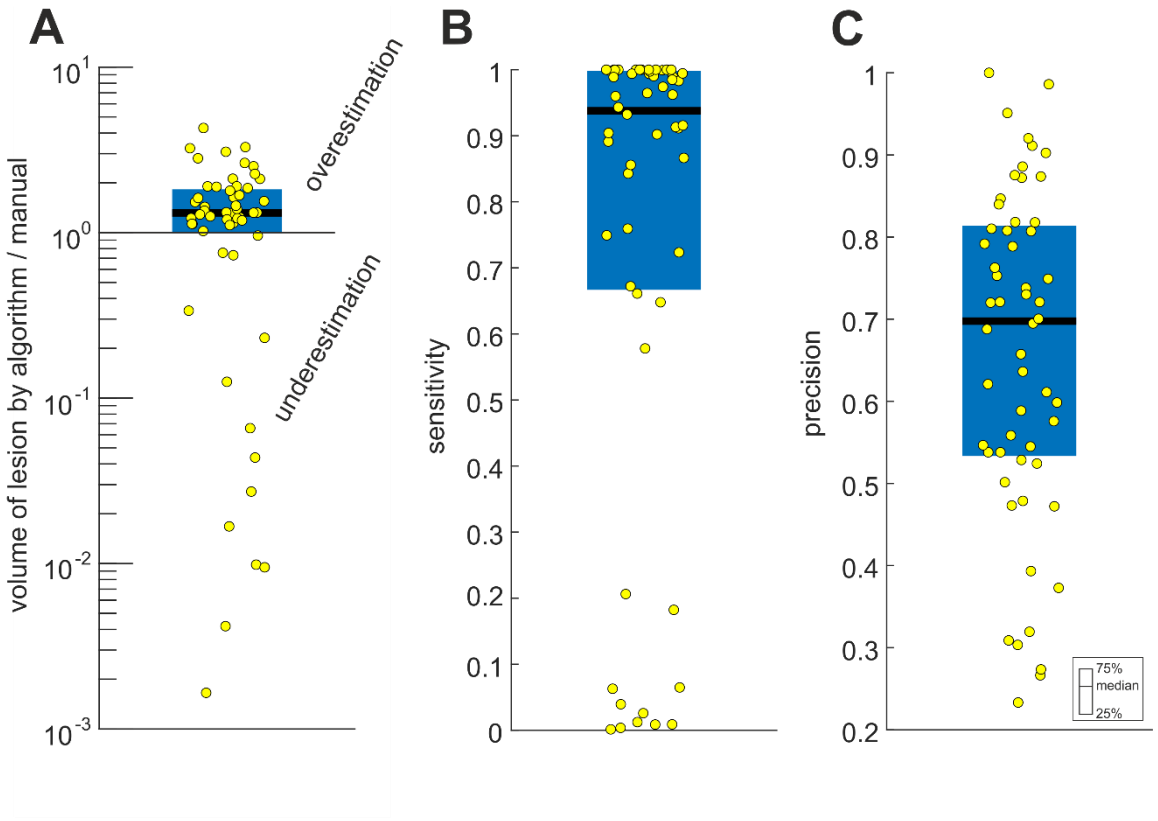

Figure 12. Comparison of the proposed method with manual delineation. (A) In 75 % of cases, the proposed method overestimates lesion volume rather than underestimates. The volume of the detected lesion was in median 1.3 (IQR 0.8) times larger than in the case of manual outlining. (B) sensitivity of the proposed method is 94 % (IQR 33 %) in the median with 70% (IQR 28 %) precision

3.2.1.Algorithm performance evaluation

Lesion detection by the proposed algorithm was compared with manual detection in 60 patients in this thesis. The volume of lesion detected by the proposed algorithm was in 75 % of cases larger (in median 1.3 times with IQR 0.8) than volume obtained by manual outlining – i.e. proposed method is likely to overestimate (Figure 12 A). This is in line with issues corresponding with the preselection of VOI with lesion described in previous paragraphs. The sensitivity of the proposed method is 94 % (IQR 33 %) in the median with 70% (IQR 28 %) precision (see Figure 12. B and C).

3.2.2.Clinical study 1 - Volumetric analysis of the ischemic lesion

The algorithm pipeline for the detection of ischemic lesion proposed in this thesis was used in one of our clinical studies. In this study diffusion and structural changes of brain tissue after cerebral ischemia were spatially described from MRI scans. Moreover, we have described

volumetric changes of ischemic tissue between acute (2-5 days) and subacute (7-12 days) phases of cerebral ischemia. Inclusion criteria, used MRI protocol, and clinical characteristics of included patients together with results of our clinical study are described in this subchapter.

Subjects recruitment

243 patients hospitalized with cerebral ischemia (stroke) were recruited in this study and underwent a battery of clinical examinations containing MRI measurement in the second week after ischemic insult (see the next chapter for exact measurement protocol). All patients were adequately informed and signed informed consent. The study was approved by the Ethics committee of University Hospital Motol (Ref. number: EK-1091/14). The study was conducted according to the Declaration of Helsinki ethical principles.

Inclusion criteria were age 18 years or older, supratentorial acute ischemic lesion on admission, and signed informed consent. Exclusion criteria were history of epilepsy or acute symptomatic seizure preceding current stroke, antiepileptic drug treatment extending the period of two weeks after current stroke, history of clinical stroke, and contraindication of gadolinium administration.

All patients were treated according to standard clinical practice, except for the addition of contrast MRI scans into the diagnostic protocol. Head CT was performed in all cases as is a clinical standard. Angio CT was performed in all cases with exception of iodine allergy or symptoms onset longer than 3 days. Patients within the time frame of acute intervention and clinical symptoms of acute stroke (sudden onset speech impairment, unilateral arm, leg, or face weakness) were given appropriate treatment (intravenous thrombolysis or/and mechanical thrombectomy) based on the decision of an on-call stroke specialist. Thirty-eight percent of patients (93 from 243) received intravenous thrombolysis and seventeen percent (41 from 234) mechanical thrombectomy. Eleven percent (27) of patients received both treatments.

Figure 13 summarizes the clinical characteristics of the recruited data set. The average age of included patients was 68 ± 12 years, with a higher representation of men (61 %). The severity of stroke was measured by NIHSS (National Institute of Health Stroke Scale, (Brott *et al.*, 1989)) scoring system at admission - average value 6.6 ± 5.6, after 24 hours - average value 4.3 ± 5.3 and on discharge from hospital - average value 2.7 ± 3.5. By mRS (modified Ranking Scale, (van Swieten *et al.*, 1988)) at admission – average value 1.6 ± 1.6 and on discharge from hospital -

average value 1.4 ± 1.3 and by ASPECTS (Alberta Stroke Program Early CT Score, (Mokin *et al.*, 2017)) - average value 9.0 ± 1.6. Post-stroke epilepsy risk SELECT score (Galovic *et al.*, 2018) was 3.6 ± 1.7. Patients stay in hospital 10.4 ± 5.6 days on average.

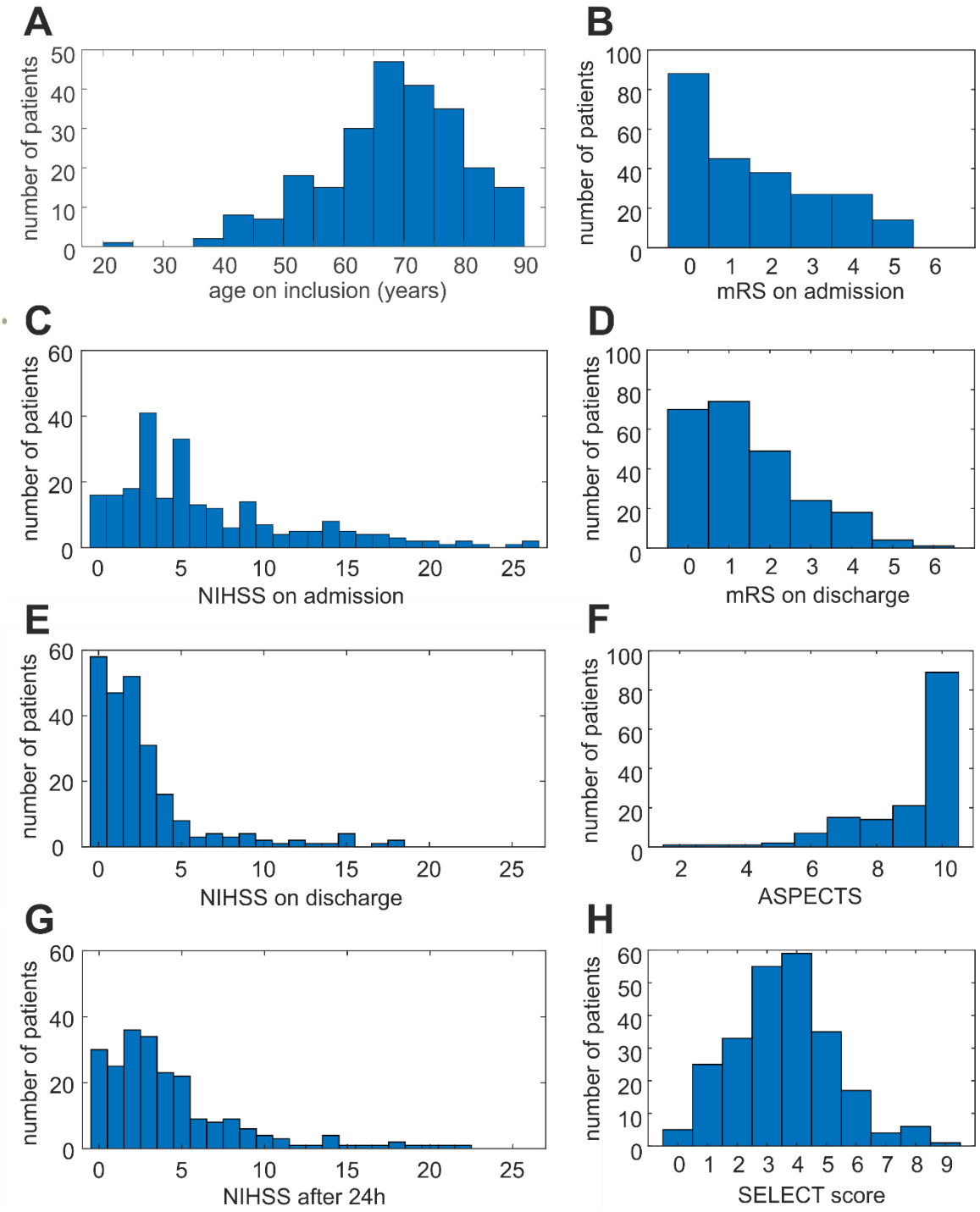

Figure 13. Clinical characteristics of 243 recruited patients. (A) Histogram of patient age at the time of stroke insult. (B) mRS (modified Ranking Scale) on admission, (D) on discharge from hospital. (C) NIHSS (National Institute of Health Stroke Scale) on admission, (E) after 24 hours, and (G) on discharge from hospital. (F) Histogram of ASPECTS (Alberta Stroke Program Early CT Score) and (H) SELECT score

MRI data acquisition

MRI sequences were measured between 7 and 12 days from symptoms onset in all 243 patients. This window was considered to be clinically relevant regarding blood-brain barrier changes.

MRI sequences were performed on Phillips Ingenia, 1.5T (Philips Medical Systems) and were acquired in the following order with the following parameters: 3D T2w (weighted) (TR 3200 ms, TE 263 ms, FA 90°, acquisition matrix 228x227, voxel size in mm 1.1x1.1x1.1), FLAIR (TR 4800 ms, TE 342 ms, acquisition matrix 208x172, voxel size in mm 1.2x1.2x1.2), DWI (TR 3751 ms, TE 93 ms, FA 90°, acquisition matrix 124x78, voxel size in mm 2.05x2.56x5.0), SWI (TR 35 ms, TE 50 ms, FA 15°, acquisition matrix 256x207, voxel size in mm 0.9x0.9x1.0), 3D T1w (TR 25 ms, TE 4.6 ms, FA 30°, acquisition matrix 220x198, voxel size in mm 1.1x1.1x1.1), DTI (TR 3157 ms, TE 94 ms, FA 90°, acquisition matrix 92x90, voxel size in mm 2.5x2.49x2.3, 32 directions), post-contrast 3D T1w with same parameters as 3D T1w. The total duration of scanning was 25 to 30 minutes.

To evaluate the integrity of the blood-brain barrier (BBB) a contrast agent (Gadovist, Gd-DTPA, Bayer Pharma AG, Germany) was injected intravenously as a bolus approximately 3 minutes (duration of previous DTI sequence) before the start of contrast T1w sequence acquisition (7.5 mL for bodyweight below 75 kg, 10 mL for the bodyweight of 75 kg and higher; corresponding to 0.1-0.15 mmol/kg of bodyweight.

If there was a clinical indication for an out of protocol MRI (such as differential diagnosis, clinical worsening, suspicion on brain stem involvement) an additional MR was included in the study. Additional MRI sequences were acquired either at Phillips Ingenia, 1.5T (Philips Medical Systems) or Siemens MAGNETOM Avanto, 1.5T (Siemens Healthineers). These sequences varied based on clinical requirements but always included DWI, axial FLAIR and T2w, coronal T1w, and sagittal T2w sequences (with TR, TE parameters set based on a used machine, with a thickness of 3-5mm and pixel size from 0.45x0.45 to 0.75x0.75 mm).

In 11 patients, additional MRI was performed in a time window 2-5 days from symptoms onset that corresponds to the acute phase of the ischemia. Those extra acute images were used in this study for the description of volumetric changes of the ischemic lesion between the acute and subacute phases.

Results of the clinical study

For further localization and analysis of ischemic lesion in recruited patients two MRI sequences were used; FLAIR (fluid attenuation inversion recovery) and DWI (isotropic diffusion map), (for the description of sequences see chapter 2.2). In 30 patients one (or both) of those sequences was either missing (patient wasn't able to undergo the whole examination properly) or heavily affected by artifacts (mostly because of the patient's movement). Those patients were excluded from further analysis. The second exclusion criterion was the absence of an ischemic lesion in both (FLAIR and DWI) MRI sequences by visual examination. Thirty-eight patients were further excluded by this selection to a total number of 175 patients selected for further analysis (see summary in Table 1).

Table 1. Number of patients selected for the study of ischemic lesion

Subgroup criteria	Number of patients
Recruited patients	243
Sufficient quality of MRI data	213
Presence of ischemic lesion in FLAIR and DWI by visual examination	**175**

175 patients (selection criteria described above) with positive ischemic findings in FLAIR and DWI MRI performed 7-12 days after ischemic insult were used for detailed analysis of ischemic lesion.

Two MRI sequences were used for localization and description of the ischemic lesion. FLAIR (Fluid Attenuation Inversion Recovery), which is sensitive preferably to structural changes in brain tissue and DWI (Diffusion-Weighted Imaging) manifesting diffusion properties of water through the brain tissue. Regions with ischemic alteration either in FLAIR or in DWI were further considered as a lesion.

ADC (apparent diffusion coefficient - another metric of diffusion-weighted image commonly used for identification of ischemic lesion) is in the time-point where our data were acquired (7-12 days after ischemia) already pseudo-normalized (for more details about ADC image and its time development see chapter 2.3). Therefore, we were not able to use ADC for the detection of ischemic lesion in our patients. Also, without the knowledge of ADC status, we were not

able to assess if hyperintensity in DWI is due to the T2 shine-through effect or due to restriction of the diffusion caused by cytotoxic edema. However, the lack of this information does not change the rationale behind our definition of the ischemic lesion as hyperintensity in FLAIR or DWI.

Regions affected by ischemia were outlined by the proposed algorithm (description of the algorithm in chapter 3.1) in both FLAIR and DWI MRI sequences. Regions with hyperintensity in FLAIR are termed in this thesis as FLAIR+, regions with hyperintensity in DWI as DWI+. Isointense regions on FLAIR or DWI are termed as FLAIR- or DWI-, respectively.

For a better spatial understanding of characteristics of affected tissue, the image of the lesion was further parcellated into three volumes of interest according to a logical combination of FLAIR+ and DWI+ volumes (FLAIR+DWI+, FLAIR+DWI-, FLAIR-DWI+). Volumes where none of the sequences was positive (FLAIR-DWI-) is termed as perilesional or non-lesional. (See Figure 14)

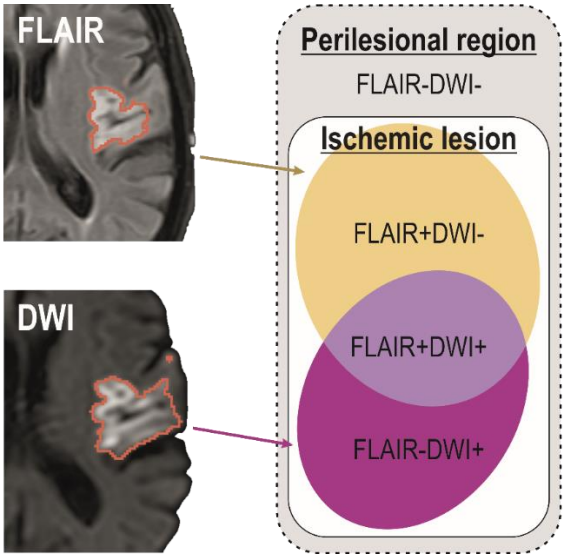

Figure 14. Image of lesional tissue was further parcellated according to alterations in intensities in either FLAIR, DWI, or both. We defined four volumes of interest as a logical combination of these two sequences. FLAIR+DWI+ as the unification of both. FLAIR-DWI+ and FLAIR+DWI- as intersection and FLAIR-DWI- as the perilesional or non-lesional region

The median volume of the ischemic lesion was 14.7 mL (IQR 43.9 mL, Figure 15. A). The ischemic lesion extended over FLAIR+DWI- (48 % in median), FLAIR+DWI+ (39 %), and FLAIR-DWI+ (13 %) regions (Figure 15. B). Median volumes of individual regions were 6.3 mL (IQR 20.1 mL) for FLAIR+DWI-, 5.1 mL (IQR 13.3 mL) for FLAIR+DWI+ and 1.5 mL (IQR 4.6 mL) for FLAIR-DWI+.

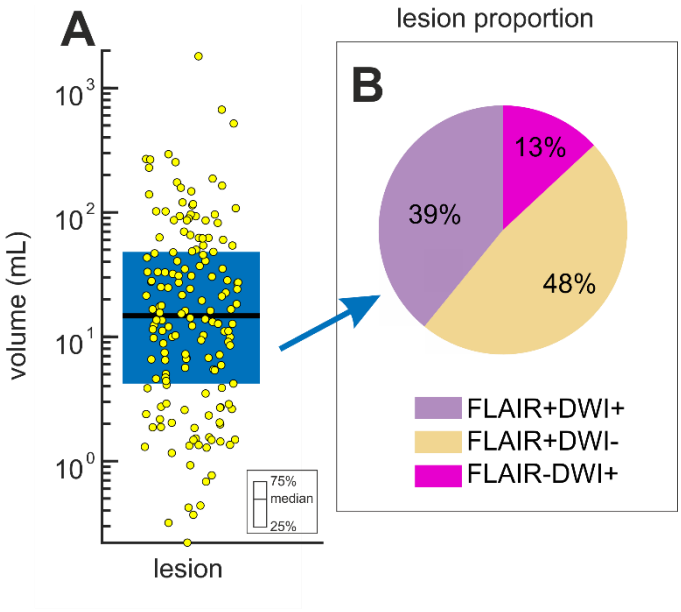

Figure 15. (A) Size of the ischemic lesion in 175 patients. (B) The median proportion of the lesion according to FLAIR and DWI

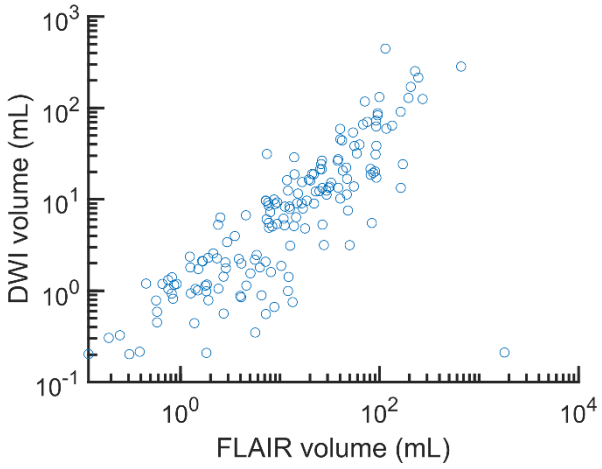

Figure 16. Correlation of volume of FLAIR and DWI regions

The volume of FLAIR+ and DWI+ regions were highly correlated by Spearman correlation (0.84 $p<0.001$) but showed only weak linear dependency by Pearson correlation (0.30 $p<0.001$) (See Figure 16).

The volumetric characteristic of the lesion in the subacute phase of ischemia (7-12 days) was described in the previous paragraph. However, we were further curious about what is happening with lesions between ischemic insult and subacute phase (individual phases of ischemia are described in more detail in theoretical chapter 2.1). 11 of recruited patients were examined also in the acute phase (2-5 days) due to clinical purposes in addition to previously described measurement in the subacute phase (7-12 days) of ischemia. Change of volume of

the ischemic lesion between acute and subacute phase in these 11 patients is described in this subchapter and documented in Figure 17.

The volume of the ischemic lesion (FLAIR+ or DWI+) in the acute phase was 15.2 mL (IQR 11.9 mL) and 21.6 mL (IQR 25.3 mL) in the subacute phase, respectively. This increase (15% in median, IQR 40.9 %) was statistically significant with p=0.024.

The region with diffusion alterations as represented by hyperintensity in DWI (DWI+) exhibited no significant change in volume (p=0.520, -3% IQR 49.5 mL) between acute (11.8 mL, IQR 12.4 mL) and subacute phase (11.31 mL, IQR 11.14 mL).

Structural maturation of the ischemic lesion proceeded between acute and subacute phase by means of 20% increase (IQR 96 %) in FLAIR+ region from 10.2 mL (IQR 7.8 mL) in acute to 14.5 mL (IQR 24.9 mL) in the subacute phase. However, this change did not reach the level of statistical significance (p=0.206).

While volume of FLAIR+DWI+ (6.7 -> 6.7mL, IQR 7.7 mL) and FLAIR-DWI+ (4.5 mL, IQR 2.7 mL -> 1.6 mL, IQR 3.1 mL) regions expressed no significant alteration (p=0.413 and p=0.279, respectively), the expansion of FLAIR+ region was due to 88% increase (IQR 48.8 %, p=0.019) in FLAIR+DWI- region (2.8 mL, IQR 1.5 mL -> 5.2 mL, IQR 16.3 mL).

Conclusion of the clinical study

In this clinical study, we have characterized ischemic lesion in 175 patients after cerebral ischemia in means of changes in structure and diffusion parameters of the affected tissue. We have also described the maturation of ischemic lesion between the acute and subacute phases of ischemia. We have reported growth of structural changes (in FLAIR) without volume alteration of diffusion changes (in DWI).

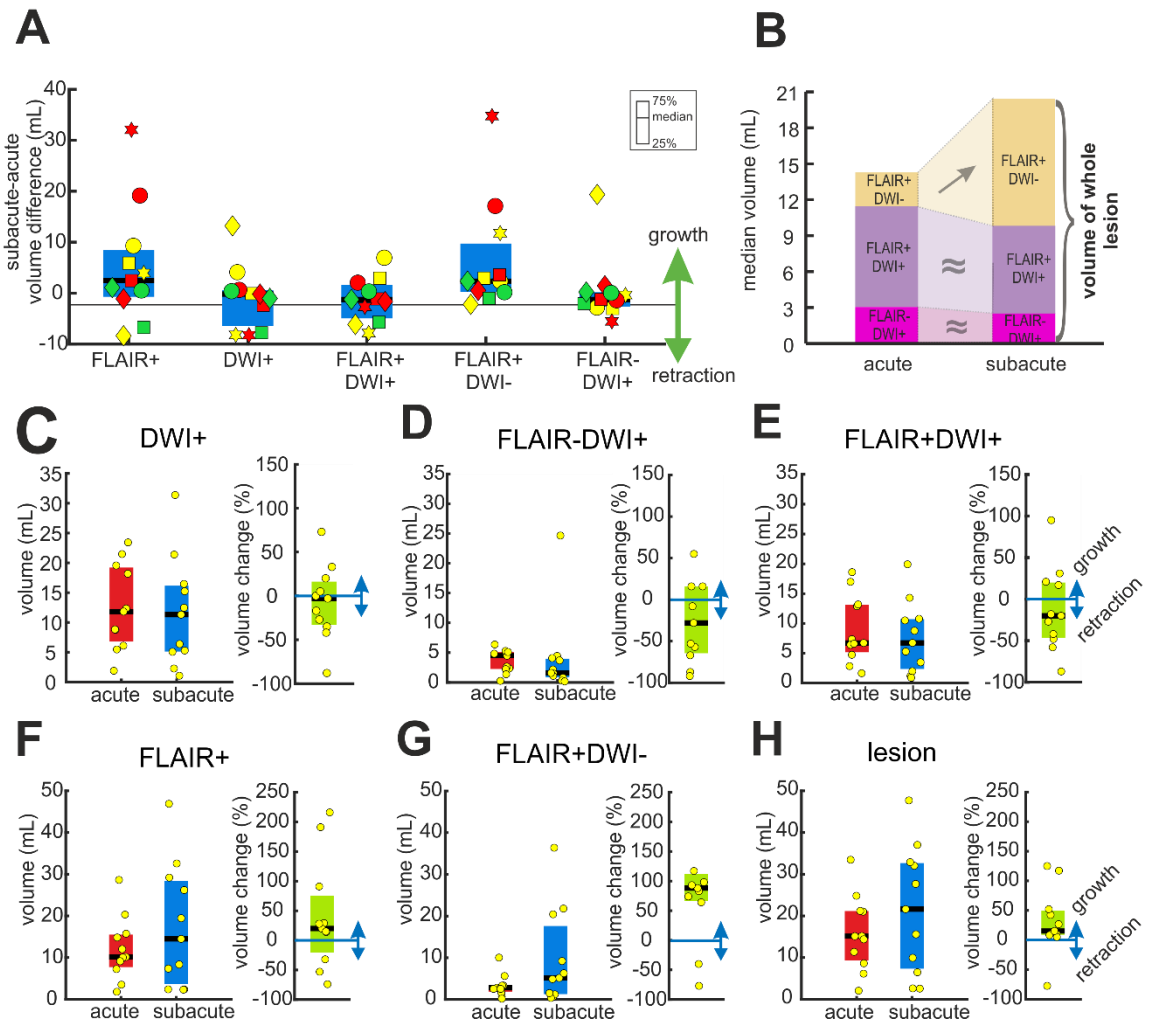

Figure 17. Our data shows time dynamics in the volume of defined VOIs in 11 patients (A) individual volume changes– every patient is defined by a unique marker. (B) median change of lesion size and its composition (≈ p=0,05-1, ↑ p<0,05). (C-G) volume changes in individual VOIs: (H) volume of the whole lesion was significantly increased (p=0.024) by 15%. (G) the increase was also observed in FLAIR+DWI- region (p=0.019). Other regions DWI+ (p=0.520), FLAIR+ (p=0.206), FLAIR+DWI+ (p=0.413) and FLAIR-DWI+ (p=0.279) exhibited no significant change

4. Assessment of blood-brain barrier disruption

Impairment of the blood-brain barrier (BBB) is a common phenomenon following cerebral ischemia, however, its role in post-ischemic processes and effect on the outcome of the disease is still not clear (for more details see chapter 2.1). An algorithm developed for the assessment of BBB impairment in post-ischemic human patients is described in this chapter together with part of our clinical study, where the algorithm was used.

For identification of regions with impaired BBB and for assessment of its severity a modified clinical MRI protocol with Gadovist (gadolinium contrast agent Gd-DTPA) is used in our pipeline. Intravenously administered chelated organic gadolinium complexes enhance nuclear relaxation rates and increase contrast in MRI because of their paramagnetic properties. Gadovist does not cross BBB in healthy tissue while in regions with the compromised barrier it leaks to the brain tissue and increases signal intensity. Thus, regions with a significantly higher signal after Gadovist injection are considered as tissue with compromised BBB.

MRI data are processed by an adopted detection algorithm originally published by (Chassidim *et al.*, 2013) in our protocol. The entire procedure is summarized and graphically presented in Figure 18. The method is based on the comparison of two consecutively recorded T1w (weighted) MR images of the head; native MRI and MRI with contrast agent (Gadovist).

4.1. Theoretical background

4.1.1. Blood-brain barrier

The blood-brain barrier (BBB) is an anatomical structure separating vascular and neural brain compartments. Its proper function is essential for normal brain activity because it maintains the homeostasis of the brain microenvironment (Araque and Navarrete, 2010). This is accomplished by the unique properties of the microvasculature of the central nervous system. Brain microvessels are formed by tightly connected (tight junctions) endothelial cells, astrocytes, and pericytes, that together provide a mechanism able to precisely control the exchange of substances between the brain and the blood (Abdullahi, Tripathi and Ronaldson, 2018). Disruption of the BBB is observed in many different neurological disorders including cerebral ischemia, epilepsy, or traumatic brain injuries (Daneman and Prat, 2015).

Loss of BBB integrity leads to extravasation of plasma proteins into the neuronal tissue and vasogenic brain edema (Stanimirovic and Friedman, 2012). Defective BBB can persist for a long time and may cause secondary inflammation and neuronal dysfunction (Abbott and Friedman, 2012; Vezzani, Friedman and Dingledine, 2013). Several plasma proteins including albumin and thrombin (Friedman, 2011; Maggio *et al.*, 2013) as well as inflammatory cytokines have been shown to trigger both acute epileptiform activity (acute symptomatic seizures) and epileptogenesis (Ivens *et al.*, 2007; Marchi *et al.*, 2007). Conversely, experimentally induced epileptic seizures in animal models transiently compromise BBB (Zimmermann, Domoki and Bari, 2008; Danjo *et al.*, 2013).

4.2. Methods

A pipeline developed as part of this thesis for the assessment of blood-brain barrier disruption is described in this chapter. The algorithm consists of six steps described in the following subchapters and graphically shown in Figure 18. This part of the thesis was published in the Clinician and technology journal (Kala *et al.*, 2017) and the whole detection algorithm was implemented as a software *Gd-Tracker*, which is freely accessible on http://bbb.biomed.cas.cz.

Step 1. - Registration, spatial normalization, and brain extraction

For images registration, normalization to MNI coordinates space, and brain extraction (skull-stripping) SPM12 Matlab toolbox (Ashburner and Friston, 2005) is used in the proposed pipeline. These steps are similar to those described in the algorithm for detection of the ischemic lesion (for more details see chapter 3.1).

Step 2. - Looking for significant changes of intensity after Gd contrast injection

The intensity of post-contrast T1w MRI scan against native T1w MRI is enhanced in regions where a contrast agent is presented (vessels and regions with impaired BBB). On the contrary, no enhancement is presented in regions without contrast agent (healthy tissue), thus native T1w and post-contrast T1w exhibit the same intensity in the healthy tissue. This step is based on the identification of pixels where significant intensity change between native and post-contrast images is present.

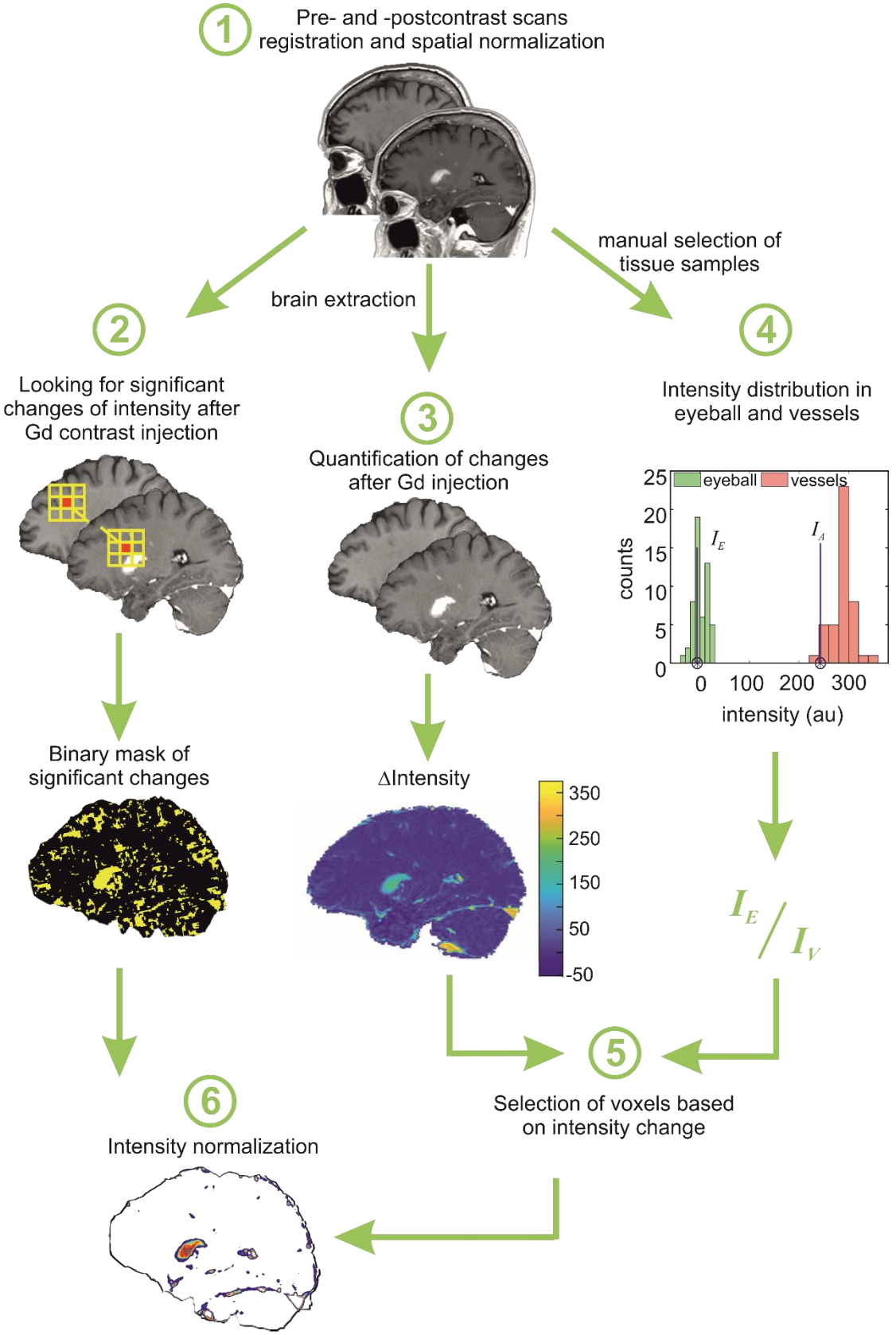

Figure 18. Scheme of the proposed algorithm for detection and assessment of blood-brain barrier impairment. Individual steps are described in detail in the following subchapters

First, for each pixel (all algorithms are 2D - each slice of 3D volume is computed individually, thus we use term pixel instead of voxel here) of pre- and post-contrast images surrounding the 3x3 area are selected for comparison. The reason why 3x3 neighborhood is used instead of comparing single pixels is an effort to suppress possible inaccurate registration. During the image registration, one image is spatially transformed to exactly match another image. Some pixels do not have perfect alignment and the false-positive difference between such pixels can be observed. This effect is decreased by using a matrix of surrounding pixels and its statistical comparison (as originally proposed in (Chassidim *et al.*, 2013)).

Each pair of two corresponding 3x3 areas (from pre- and post-contrast images) is compared using paired t-test to determine changes between pre- and post-contrast images. Pixels (represented by its 3x3 neighborhoods) with P-values smaller than 0.05 are considered to be statistically significant and are used for the construction of the binary map, where significant pixels are represented by 1 and nonsignificant by 0. FDR (false discovery rate) statistical correction is used to suppress the impact of multiple comparisons.

Step 3. - Quantification of changes after Gd injection

The difference between pre- and post-contrast images is calculated by (Equation 3). The difference corresponds to the amount of contrast agent in the tissue.

$$\Delta I(x,y,z) = I_{post}(x,y,z) - I_{pre}(x,y,z) \qquad \text{(Equation 3)}$$

Where ΔI (au) is intensity difference and I_{pre} and I_{post} are MRI image intensities of pre- and post-contrast images, respectively.

Step 4. - Calculation of intensity distribution in eyeball and blood vessels

To obtain reference values for further tissue selection (Step 5) and intensity normalization (Step 6) several pixels representing eyeball and vessels are manually selected in this step. A larger area (9x9 pixels) is repeatedly selected (two or three different places for one tissue) instead of representing tissue intensity by one value from a single pixel. Significant outliers due to various artifacts or other disturbances coming from the measurement of data acquisition are often presented in our datasets. These outliers are excluded to obtain homogenous datasets.

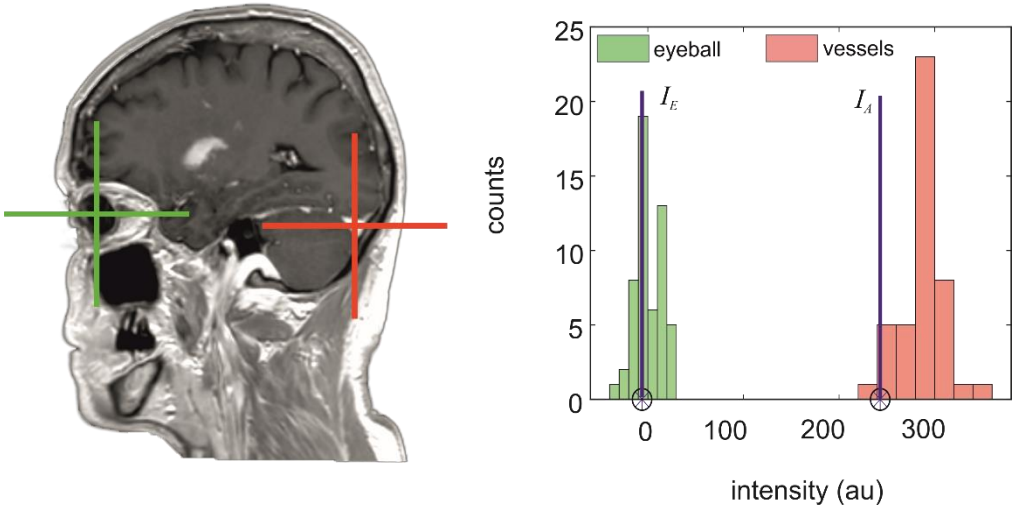

Figure 19. Manual selection of eyeball and vessel and corresponding histograms. Quantiles I_E and I_A are used for voxel selection and normalization

Intensity distribution (histograms) are calculated from selected tissue samples as shown in Figure 19 and reference values (IE and IV for eyeball and vessels, respectively) are calculated as quantiles of those distributions according to (Equation 4) and (Equation 5).

$$I_E = Quantille\ (eyeball, 0.25) \quad \text{(Equation 4)}$$

$$I_V = Quantille\ (vessels, 0.05) \quad \text{(Equation 5)}$$

Step 5. - Selection of voxels based on intensity change

In the next step, ΔI map is masked by a series of conditions (see (Equation 6) and (Equation 7)) to avoid either noise (or tissue with minor post-contrast changes) or large vessels. Only pixels satisfying both conditions are selected for final normalization.

$$\Delta I(x, y, z) < I_V \quad \text{(Equation 6)}$$

$$\Delta I(x, y, z) > I_E + (I_V - I_E) \cdot 0.25 \quad \text{(Equation 7)}$$

Pixels with intensity change higher than I_V (intensity change observed in vessels) are removed by application of (Equation 6). These pixels correspond mostly to other vessels. Pixels with minor intensity change (noise, artifacts, small vessels) are removed by (Equation 7).

Step 6. - Intensity normalization

The intensity of raw MRI data is dependent on many physical factors (setting of magnetic coils, room temperature, magnetization, etc.) and varies between individual measurements. To establish a stable processing method independent of measurement variability and to ensure intersubjective comparability a normalization of all scans to a common scale based on two reference values is used. Value in the eyeball is considered as minimal (0) because the Gd contrast agent does not leak to the vitreous body of a healthy eyeball. On the other hand, intensity in dural venous sinuses (sinus sagittal superior, transverse, or rectus) is considered as maximal (1), because the highest concentration of contrast agent is in the blood.

In the last step of the proposed algorithm, modified ΔI map (after application of (Equation 6) and (Equation 7) in the previous step) is combined with the mask of significant changes (Step 2) and normalized to a common scale, where quantiles calculated in Step 4 are used as reference values - I_E (eyeball) as minimal value (0) and I_V (vessels) as maximal (1).

Figure 20 shows an example of the detection of BBB disruption by the described algorithm.

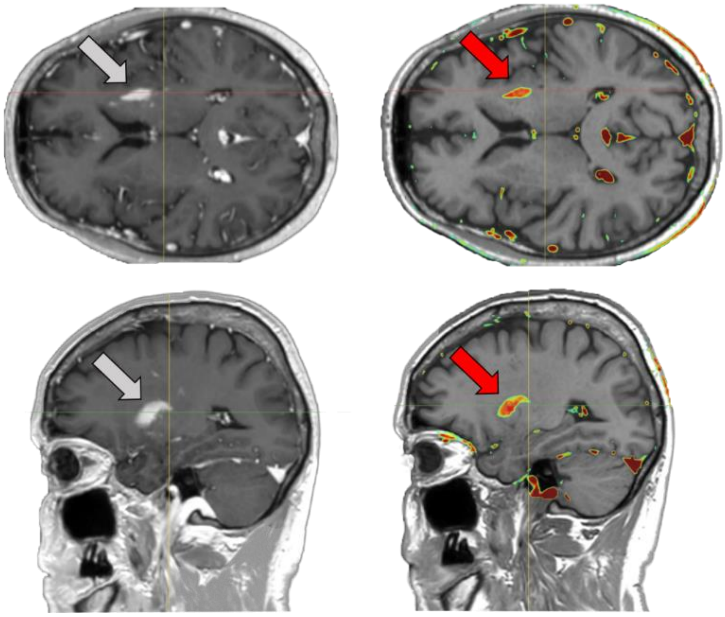

Figure 20. Detection of blood-brain barrier disruption by the proposed algorithm

The Extravasated Gd – parameter for a description of disrupted BBB

For a quantitative description of BBB impairment and comparison of BBB impairment in different tissues of interest a parameter called *the Extravasated Gd* was invented. It denotes the percentage of Gd (gadolinium-based contrast agent) extravasation into the brain tissue and is calculated by following formulas.

$$\Delta Intensity = Intensity_{post-contrast} - Intensity_{native} \quad \text{(Equation 8)}$$

$$Extravasated\ Gd = \frac{\sum^{VOI} \Delta Intensity}{\sum^{whole\ brain} \Delta Intensity} \cdot 100 \quad \text{(Equation 9)}$$

Where *Intensities* (au) are values of MRI image (T1w and T1w after contrast admission), *VOI* is calculated volume of interest (lesional tissue, FLAIR+ tissue, etc.). Parameter *the Extravasated Gd* represents a fraction of Gd extravasation into the studied region versus all contrast agents extravasated into the brain. The parameter is used in our clinical study in the next chapter.

4.3.Results

A developed pipeline for the assessment of BBB disruption was used in a clinical study. The whole study, its design, and results are described in this chapter.

4.3.1. Clinical study 2 - Relationship of blood-brain barrier damage and stroke

Cerebral ischemia is often followed by impairment of the blood-brain barrier (BBB). It is characterized by extravasation of water and blood elements to extracellular space across a vessel wall, which can further affect lesional tissue (disruption of homeostasis, inflammation, neuronal loss, etc. For further details see Chapter 2.1). BBB disruption is the main topic of many studies, however, its role in post-ischemic processes and effect on the outcome of the disease is still not clear.

Several results from our clinical study describing spatial dependencies of BBB impairment and ischemic stroke are summarized in this chapter. For the detection of BBB impairment, the algorithm pipeline proposed in this thesis was used.

Subject and data acquisition

The same patient cohort and same MRI protocol as described in chapter 3.2.2 were used in this part of the study. From 243 recruited patients hospitalized with cerebral ischemia in 16 patients was MRI sequence was either missing (patient wasn't able to undergo the whole examination properly) or heavily affected by artifacts (mostly because of patient movement). These patients were excluded from this part of the study. From the remaining 227 patients in 167 (74 %) BBB impairment was observed.

Further analysis of blood-brain barrier impairment was performed at a subgroup of 60 patients with the longest follow-up time and published in (Kala et.al., under revision). The subgroup was representative of the whole dataset. Our goal in this part of the study was to qualitatively and quantitatively assess BBB disruption in our patients and spatially correlate it with the ischemic lesion.

Table 2. Number of patients selected for the study of blood-brain barrier impairment

Subgroup criteria	Number of patients
Recruited patients	243
Measured MRI data in proper quality	227
Presence of blood-brain barrier impairment	167 (74 %)
Patients with the longest follow-up time used for further analysis	**60**

Results of the clinical study

To evaluate the integrity of the blood-brain barrier (BBB) a T1w MRI with intravenously administered gadolinium (Gd) contrast agent was measured 7-12 days after stroke in 60 patients. The tissue was BBB was compromised was identified by the algorithm proposed in this thesis and the volume of such tissue was compared with the volume of ischemic tissue.

Median volume of tissue with detected gadolinium contrast agent extravasation (7.76 mL, IQR 16.13 mL) was compared with the volume of the lesion (21.6 mL, IQR 25.3 mL) detected in FLAIR or DWI in all 60 patients. The comparison showed a strong uphill correlation (Pearson coefficient 0.74, $p<0.001$. See Figure 21).

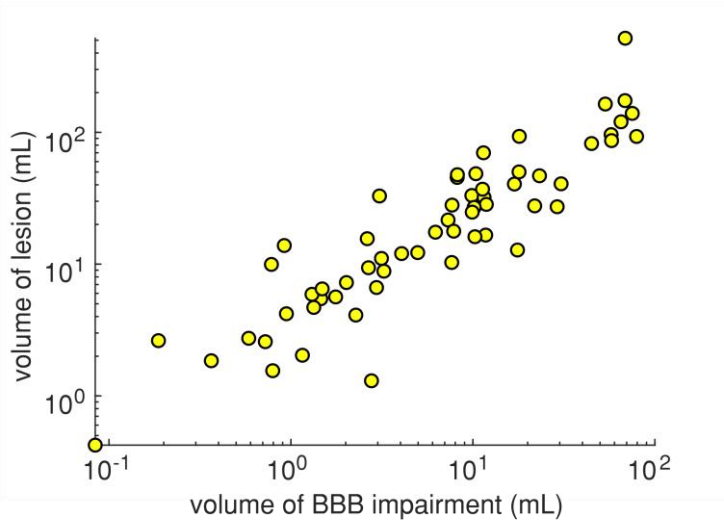

Figure 21. Strong uphill correlation (Pearson coefficient 0.74, $p<0.001$) between the volume of ischemic lesion and volume of blood-brain barrier impairment

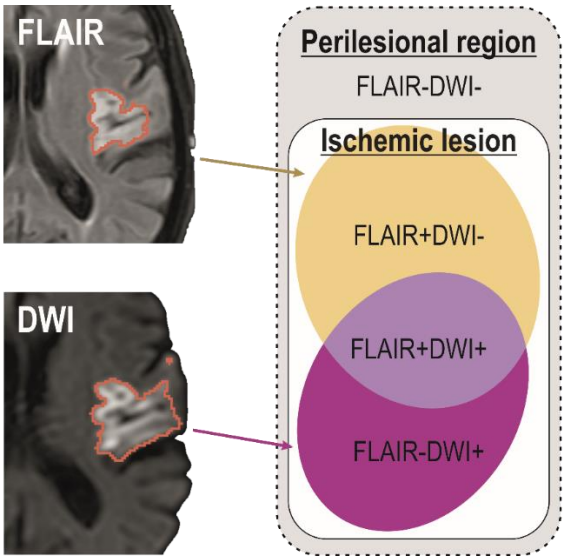

Figure 22. Image of lesional tissue was further parcellated according to alterations in intensities in either FLAIR, DWI, or both. We defined four volumes of interest as a logical combination of these two sequences. FLAIR+DWI+ as a unification of both. FLAIR-DWI+ and FLAIR+DWI- as intersection and FLAIR-DWI- as the perilesional or non-lesional region (copy of Figure 14, chapter 2)

The Extravasated Gd was assessed in three subregions of the ischemic lesion. Subregions were defined according to FLAIR and DWI MRI images. In short, tissue with the hyperintense image in FLAIR MRI (FLAIR+) suggests structural changes of the tissue, however, hyperintensity in DWI MRI (DWI+) shows changes in diffusion properties of the tissue. Subregions were defined as a logical combination of FLAIR+ and DWI+ volumes (FLAIR+DWI+, FLAIR+DWI-, FLAIR-DWI+) as shown in Figure 22. For more details see chapter 2.

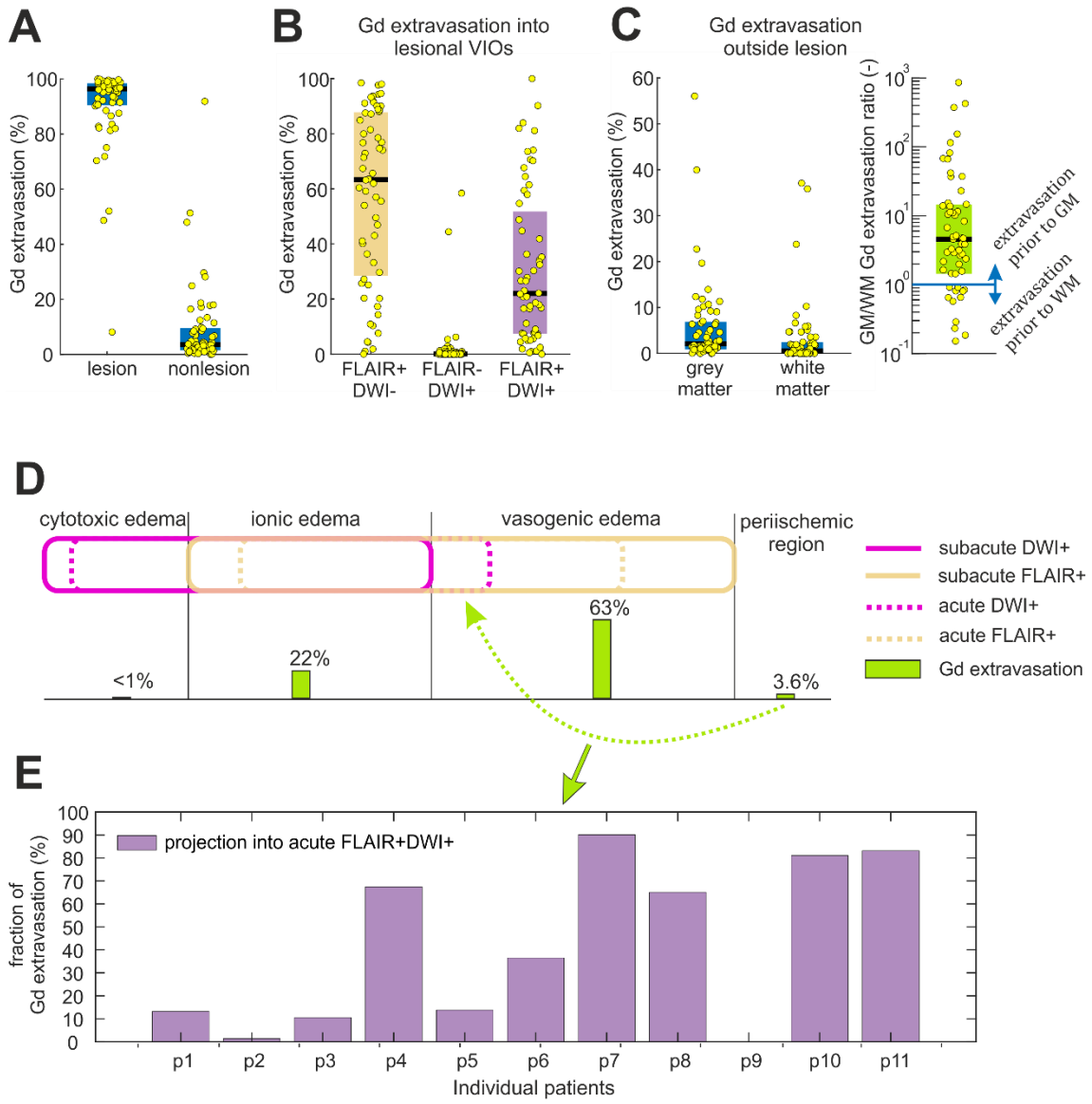

Figure 23. (A) Distribution of the Extravasated Gd between lesional and non-lesional brain tissue and into different brain regions (B) inside or (C) outside lesion in 60 patients in the subacute phase of ischemia (7-12 days). (D) Scheme of volume changes in brain regions measured in 11 patients in subacute (solid line) and acute (2-5 days, dashed line) phase of ischemia. Gd extravasation was measured only in the subacute phase. Data shown in (D and E) are median values in 11 patients. Subacute Extravasated Gd was spatially registered with acute MRI and projected into regions of interest in the acute phase of ischemia. (E) fraction of peri-ischemic Extravasated Gd that spatially correlates with acute FLAIR+DWI+ region

96 % (IQR 8.1 %) of all extravasated Gd contrast agent was observed inside the lesion. 63 % (IQR 59.4 %) of Gd was localized in FLAIR+DWI- region, 22 % (IQR 44.3 %) in the FLAIR+DWI+ region. Only a small amount of Gd (<1%) was observed in the FLAIR-DWI+ region (see Figure 23 A-B).

Spatial analysis of Gd leakage revealed that **part (3.6 %, IQR 8.1%) of the Extravasated Gd is located in the region (0.6 mL 2.2 mL IQR) outside detected an ischemic lesion** in MRI. The Extravasated Gd in this region was significantly higher ($p<0.001$) in grey matter (2 %, IQR 6 %) in comparison to white matter (0.5 %, IQR 2.4 %). (Figure 23 C)

As described above, 3.6 % of Gd extravasates in the subacute phase of ischemia (7-12 days) outside lesion - i.e to the tissue that in FLAIR and DWI does not suggest any pathological changes. It seems unlikely that the blood-brain barrier happened to be impaired without the presence of structural or diffusion changes (observable in FLAIR or DWI MRI). Likely, such changes manifest earlier and in time of Gd measurement (7-12 days) are already pseudo-normalized in FLAIR and DWI MRI. To verify this hypothesis, we have used 11 recruited patients that were examined also in the acute phase (2-5 days) due to clinical purposes in addition to measurement in the subacute phase (7-12 days) of ischemia. For those 11 patients, subacute measurement was spatially registered with acute (2-5 days) MRI and subacute Gd extravasation was projected into regions of interest in acute measurement in 11 patients.

In 5 from 11 patients more than 60 % of **Gadolinium that subacutely extravasated outside lesion was acutely part of the lesion, more precisely it spatially corresponded with FLAIR+DWI+ regions, i.e. region affected by ionic edema.** (See Figure 23 D). It is important to stand out that Gd extravasation was measured only in the subacute phase and to acute ischemic regions only virtually projected.

Conclusion of the clinical study

In this part of our clinical study, we have shown that blood-brain barrier impairment strongly positively correlates with the volume of the ischemic lesion in patients after cerebral ischemia. We have described the spatial distribution of BBB impairment in subregions of the ischemic lesion. 63 % of the Extravasated Gd was observed inside FLAIR+DWI- subregion, i.e. tissue affected by vasogenic edema, however only 22 % was localized in FLAIR+DWI+ subregion. A minimal amount of Gd was reported in tissue without FLAIR correlate- i.e. in the FLAIR-DWI+ region. Further, we have examined the Gd extravasation outside the ischemic lesion and reported, that majority of Gadolinium that subacutely extravasated outside lesion was in earlier phases of the deceased part of the lesion. However, we must stand out, that in this study Gd extravasation was measured only in the subacute phase and to acute ischemic regions only virtually projected. Thus, the results must be interpreted cautiously.

5. Analysis of longitudinal variations in white matter neuronal tracts

White matter fiber tract segmentation enables detailed analysis of individual white matter tracts. It helps to characterize the healthy brain and identify areas containing abnormal morphology in diseased brains. (Wasserthal, P. Neher and Maier-Hein, 2018)

Diffusion magnetic resonance is the most common approach for white matter tract segmentation. A computational technique where tracts are reconstructed from the diffusion MR is called tractography and has been intensively developed and improved in the last two decades. It is based on uneven diffusional properties of the brain tissues, where the most prominent diffusion is observed along white matter axons. The directional distribution of the diffusion can be assessed as a diffusion tensor and serves further as input for tractography.

Besides the reconstruction of neuronal tracts, diffusion MRI and its parameters (metrics) have proved to be useful in the study of brain pathologies as it can reveal pathological phenomena normally invisible in common anatomical MRI (as T1w, T2w, FLAIR, etc.). Diffusion MRI is routinely used for example in the diagnosis of brain edema or identification of ischemic stroke age. Diffusion parameters are usually observed in the whole brain (voxel-wise analysis), however, a study of diffusion parameters along individual neuronal tracts (tract-wise analysis) can further contribute to a deeper understanding of processes behind brain pathologies. Calculation of diffusion parameters along reconstructed neuronal tracts is called tractometry.

A complex algorithm pipeline for diffusion MRI data preprocessing, tractography, and tractometry along reconstructed tracts was tailored in this thesis and is described in this chapter. Our aim is to provide a complete and fully free solution for the analysis of diffusion MRI by means of tractography.

Principles of diffusion MRI in human brain tissue, description of diffusion parameters (metrics), and basics of tractography and TractSeg algorithm are described as Theoretical background in this chapter. It is followed by a full description and documentation of the proposed algorithm pipeline and, in the last part of this chapter, by the test of algorithm behavior and performance in a non-standard situation (as in presence of cerebral ischemia lesion).

5.1. Theoretical background

5.1.1. Anisotropic diffusion in brain tissue

It is well known, that structure of the material is reflected by anisotropic (uneven) diffusion of particles through the material. The more complex the structure is, the more anisotropic is the diffusion. The human brain is a well-organized structure with a high number of different compartments (neurons, glial cells, vasculature, CSF, …), therefore it is defined by high variability in diffusion anisotropy. The diffusion-driven motion of water molecules inside human brain tissue is hindered mostly by cell membranes and vice versa is most "free" in fluids like blood and CSF. White matter neuronal fibers (long tracts of myelinated axons) have high directionality, therefore high anisotropy of water diffusion as was reported already in (Chenevert, Brunberg and Pipe, 1990). This fact is used for the identification of white matter tracts from diffusion-weighted magnetic resonance in a technique called tractography.

5.1.2. Diffusion-weighted imaging

Diffusion parameters of the tissue are measured by an MRI sequence called diffusion-weighted images. Commonly, a diffusion-weighted image consists of several T2w 3D scans with an extra magnetic gradient from at least three different directions and at least two different b values (parameter of MRI scan indicating the strength of diffusion effects on the tissue). From a diffusion-weighted image, several diffusion metrics can be calculated. The most common metrics, DWI and ADC, were already described in chapter 2.2. In the following chapter, the calculation of those parameters is described in detail together with other diffusion metrics.

5.1.3.Diffusion parameters (metrics)

Variable diffusion behavior of the tissue can be described by several parameters; called diffusion metrics. Different values of those parameters suggest variances in the tissue. This is commonly used in a method called tractography, where white matter neuronal fibers can be identified as tissue with the fastest diffusion. The variance of diffusion parameters can be also useful for the identification of abnormal/pathological tissue in the brain such as post-ischemic tissue, focal cortical dysplasia, or various types of edema. On the other hand, observation of diffusion parameters in the tissue affected by pathology can bring novel insight into the pathophysiology of the disease or post-pathological reparative processes in the brain. Diffusion metrics used in our study are described in this subchapter and shown in Figure 24.

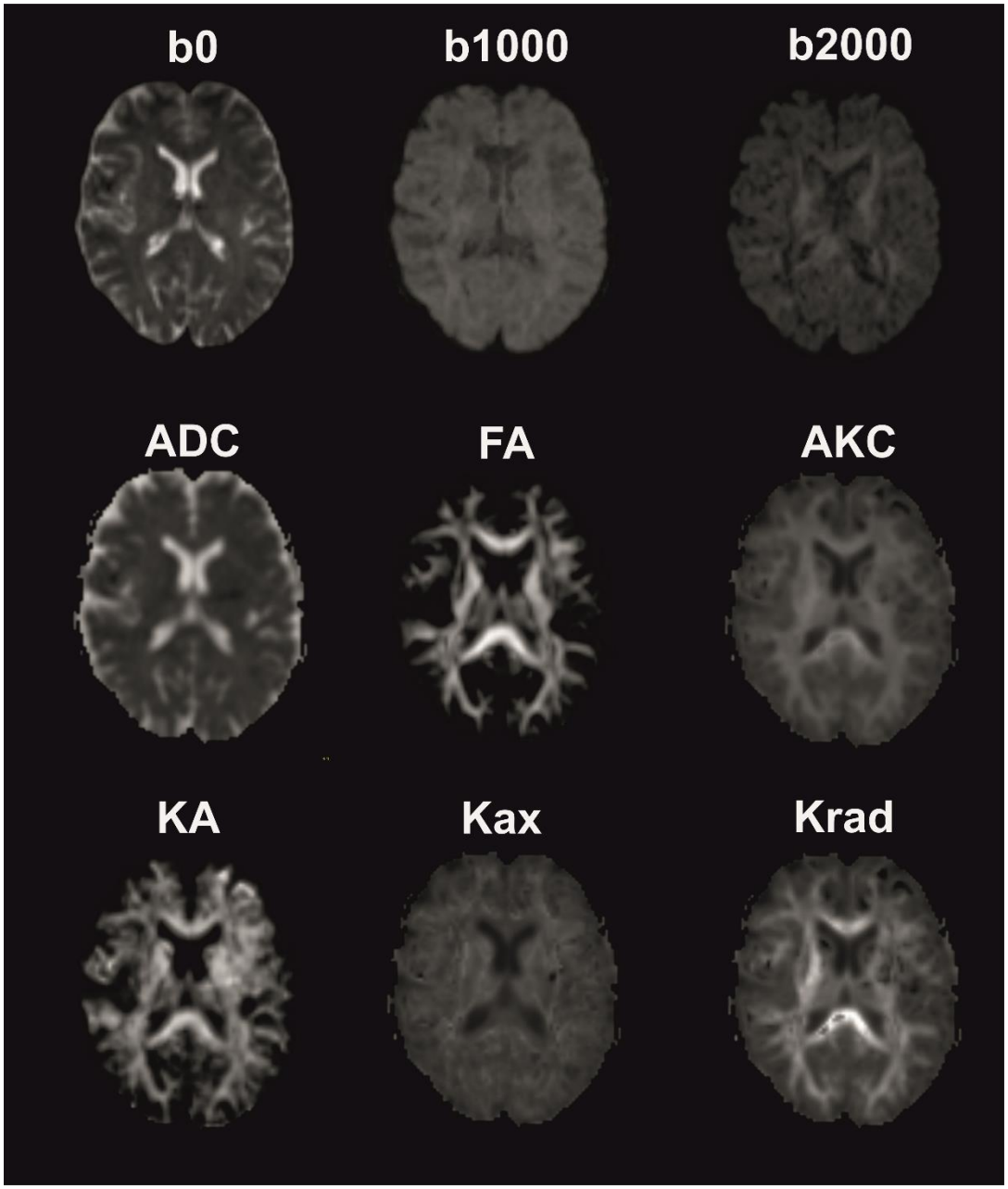

Figure 24. Metrics of diffusion-weighted image. Above, diffusion images with an extra gradient with b-value 0, 1000, and 2000, respectively. Apparent diffusion coefficient (ADC), Fractional anisotropy (FA), Apparent kurtosis coefficient (AKC), Kurtosis anisotropy (KA), Axial kurtosis (Kax), and Radial kurtosis (Krad)

Isotropic diffusion map (DWI)

Isotropic diffusion map (usually called DWI) is one of the two most basic diffusion parameters. It is calculated as a mean of individual directions of diffusion in the tissue and shows a prominent direction of the diffusion. As DWI is reconstructed from T2 images, the effect of T2 itself propagates into diffusion image. This effect is called T2 shine-through.

DWI has low values in tissue with free diffusion such as brain ventricles (filled with cerebrospinal fluid (CSF)) and increases its intensity with an increase of diffusion restriction. DWI is bright in post-ischemic lesional tissue and suggests the presence of cytotoxic edema or in later phases of ischemia (3rd week) T2 shine-through effect (for more details see chapter 2.3).

Apparent diffusion coefficient (ADC) = Mean diffusivity (MD)

The second most common diffusion parameter is the apparent diffusion coefficient (ADC) also called mean diffusivity (MD). ADC is dimensionless and shows the magnitude of the diffusion in the most prominent direction and is calculated by (Equation 10).

$$ln\left(\frac{S_{DWI}}{S_0}\right) = -b \cdot ADC \qquad \text{(Equation 10)}$$

Where S_{DWI}(-) is diffusion-weighted image signal, S_0 (-) is called baseline signal measured with b=0, and b (s/mm²) is a parameter of diffusion MRI measurement called b-value that represents the strength of the effect of diffusion on MRI image. Division of DWI signal by baseline signal suppresses the effect of T2 sequence and thus avoids T2 shine-through issue. (Stejskal and Tanner, 1965)

ADC has inverse behavior than DWI metric. It is bright in regions with free diffusion (such as CSF) and dark where diffusion is restricted.

DWI and ADC parameters have different time curves during the development of cerebral ischemia. Therefore, it is possible to determine the age of the ischemia by comparing DWI and ADC images. (see chapter 2.3)

Fractional anisotropy (FA)

FA represents diffusion asymmetry within a voxel. It varies between 0 (perfect isotropic diffusion) and 1 (one-directional anisotropic diffusion). It is calculated from diffusion tensors eigenvectors by the following formula.

$$FA = \sqrt{\frac{(\lambda_1 - \lambda_2)^2 + (\lambda_2 - \lambda_3)^2 + (\lambda_1 - \lambda_3)^2}{2 \cdot ({\lambda_1}^2 + {\lambda_2}^2 + {\lambda_3}^2)}} \qquad \text{(Equation 11)}$$

Where $\lambda_1, \lambda_2, \lambda_3$ are eigenvectors of diffusion tensor (main axes of diffusion ellipsoid). In an isotropic environment, diffusion ellipsoid is a sphere, all eigenvectors are equal, and FA = 0. With progressive anisotropy, the diffusion sphere becomes more elliptical and the FA value increases. (Minati, We and Glarz, 2007)

As a result, FA of CSF is zero, however, it increases along highly-oriented neuronal tracts.

Apparent kurtosis coefficient (AKC) = Mean kurtosis (MK)

Figure 25 demonstrates that the single exponential diffusion model as used in the calculation of ADC metric (Equation 10) does not represent real observation. Therefore, a second parameter called kurtosis was added to the model as is shown in (Equation 12).

$$ln\left(\frac{S_{DWI}}{S_0}\right) = -b \cdot ADC + \frac{1}{6} \cdot b^2 \cdot ADC^2 \cdot AKC \qquad \text{(Equation 12)}$$

The formula is similar to (Equation 10) with extra element AKC (-), which is apparent kurtosis coefficient (also called mean kurtosis (MK)). To solve the equation, measurement with at least two *b*-values has to be acquired. (Lu *et al.*, 2006)

Radial and axial kurtosis

Diffusional kurtosis is in practice defined as a tensor reconstructed from many multi-directional measurements. Mean kurtosis is then acquired by averaging diffusional kurtosis over all of the directions and thus is directionless. However, information about directionality turned out to be useful for the differentiation of various tissue types in the human body. Metric called axial kurtosis shows diffusional kurtosis in the direction of the highest diffusion and radial kurtosis in the perpendicular direction. (Tabesh *et al.*, 2011)

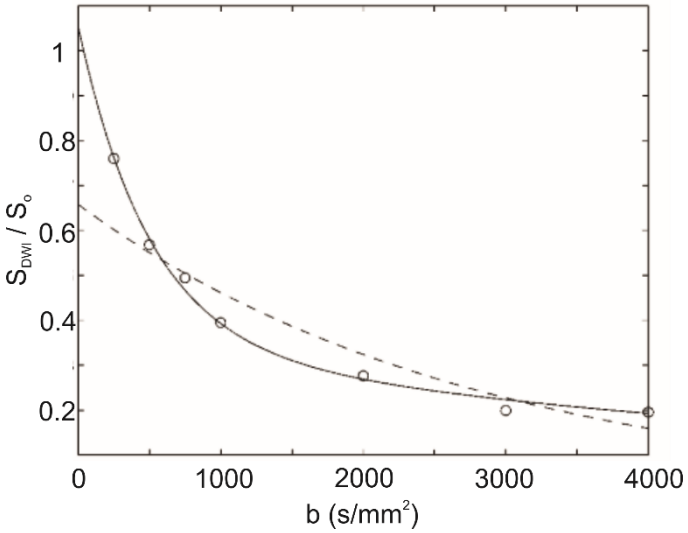

Figure 25. Signal decay curve from white matter tissue. Empty circles represent real measurement, dashed line corresponds to the exponential fitting of the ADC model according to (Equation 10). The solid line represents bi-exponential fitting by kurtosis model according to (Equation 12). The kurtosis model represents real measurement better. The graph was adopted from (Minati, We and Glarz, 2007)

Kurtosis anisotropy (KA)

Similar to fractional anisotropy, kurtosis anisotropy (KA) represents the asymmetry of diffusion kurtosis within a voxel of a tissue and is calculated by the following formula.

$$KA = \sqrt{\frac{3}{2}}\sqrt{\frac{(K_1 - K_2)^2 + (K_2 - K_3)^2 + (K_1 - K_3)^2}{({K_1}^2 + {K_2}^2 + {K_3}^2)}} \qquad \text{(Equation 13)}$$

Where $K_1, K_2, K_3$are eigenvectors of diffusion kurtosis tensor (main axes of diffusion kurtosis ellipsoid). (Glenn *et al.*, 2015)

5.1.4. Tractography – reconstruction of white matter tracts

Many algorithms were developed to reconstruct neuronal tracts from diffusion MRI. The most common approach is to calculate the dominant direction(s) of diffusion in every voxel of the brain and then connect those voxel-wise directions into tracts (or bundles of tracts) with continual directionality. This is not an easy task and it has many pitfalls. A lot of basic approaches tend to fail in regions containing more than one dominant fiber per voxel (i.e. fiber crossing). Other different techniques were developed to overcome the fiber crossing issue. In this thesis, we have used a method proposed by (Tournier *et al.*, 2004) and implemented in

MRtrix software (Tournier *et al.*, 2019), that uses spherical constrained deconvolution of signal to distinguish different tracts within a single voxel.

5.1.5. A simplified description of tractography algorithm

As was already described, tractography (reconstruction of white matter tracts) is based on the identification of the dominant direction of water diffusion using diffusion-weighted MRI. Assuming all fibers in the brain have the same absolute (omitting directionality) effect on diffusion, the diffusion-weighted signal from a single coherently oriented fiber population can be represented by the general response function *R(h)* with a specific orientation. However, in voxels where more tracts with different directions are presented, diffusion signal is formed as summation (more precisely convolution) of several response functions and their orientations. Spherical deconvolution is therefore applied to distinguish the effects of different fiber tracts (Tournier *et al.*, 2004). The result of such deconvolution is called fiber Orientation Density Function (fODF) (Tournier, Calamante and Connelly, 2007).

Calculated fODFs are used as an input for tractography itself. *The most commonly employed approach for segmenting white matter tracts is virtual dissection: streamlines that correspond to anatomically well-defined tracts are manually extracted from a tractogram using combinations of inclusion and exclusion of regions-of-interest (ROIs).* (Wasserthal, P. Neher and Maier-Hein, 2018). However, such an approach is tedious, time-consuming, skilled expert requiring and nevertheless sensitive to subjective bias. Therefore, a variety of automatic approaches were developed. TractSeg toolbox (Wasserthal, P. Neher and Maier-Hein, 2018) claiming fast and accurate white matter tract segmentation was used in this study.

TractSeg uses an atlas of 72 anatomically well-known white matter tracts and a fully convolutional neural network (FCNN) to segment tracts directly using their fiber orientation distribution function (fODF, see above). Using this approach, we are able to avoid common problematic parts of preprocessing such as registration with an atlas or anatomical parcellation. FCNN processes fODF with prior knowledge of typical trajectories of individual tracts and extract a list of Tract Orientation Maps (TOM). Each TOM is a representation of one specific tract and each of its voxels contains only one respective orientation vector. Thus, successive tractography is not affected by the crossing of fibers in different directions. (Wasserthal, P. F. Neher and Maier-Hein, 2018)

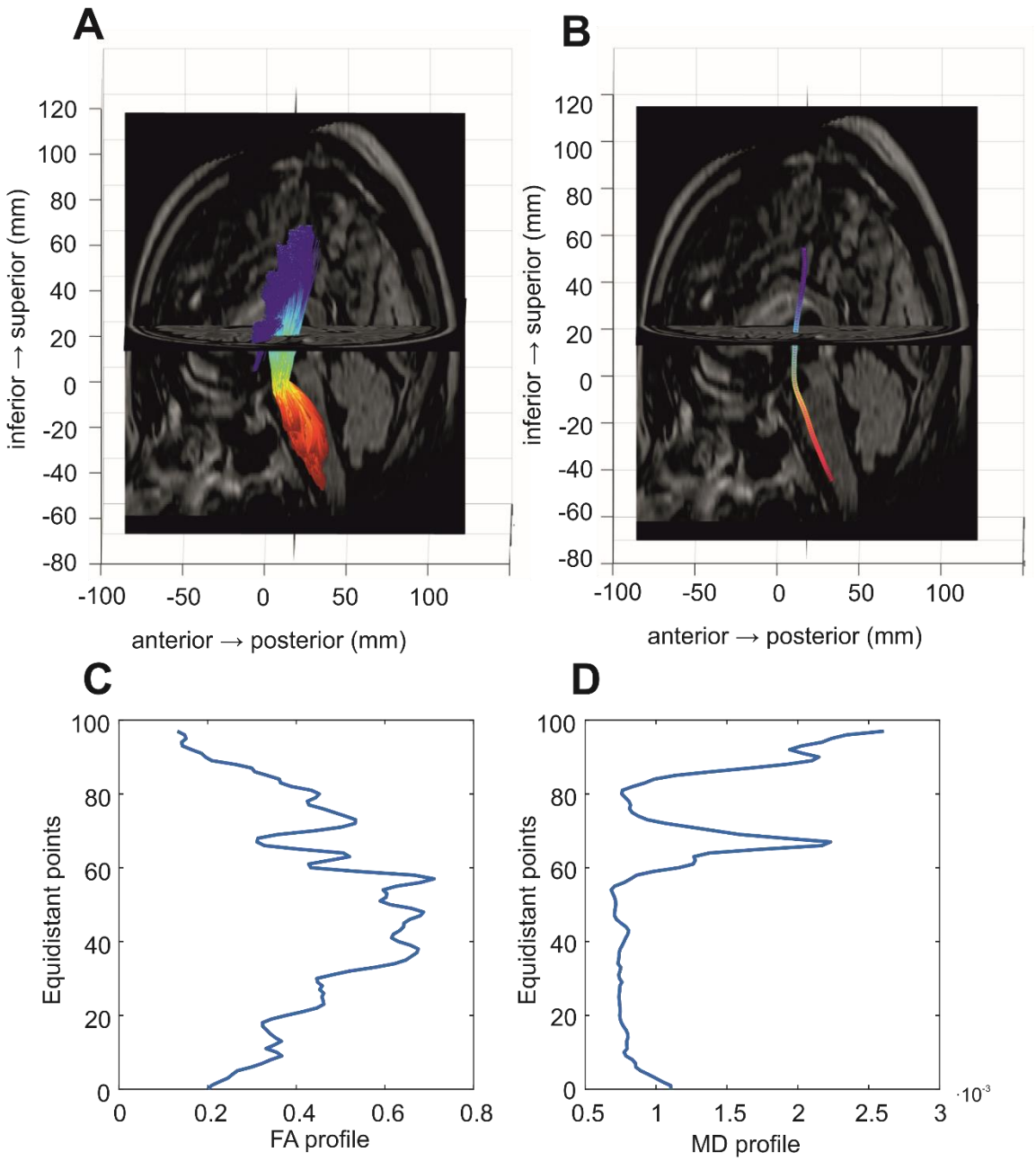

Figure 26. (A) bundle of 5000 fibers as a representation of cerebrospinal neuronal tract. Fibers were seeded from the cortex (superior end of the tract, in blue). (B) The average trajectory of the tract is represented by one centroid fiber. Two metrics were calculated along with centroid (C) fractional anisotropy FA and (D) mean diffusivity MD

Another feature of the TractSeg algorithm is the implementation of the tractometry approach. This is a technique used for the calculation of profiles of diffusion metrics (like FA, MD, kurtosis parameters, etc.) along the tracts. This is especially useful for the identification of any changes in white matter (either across patient groups or longitudinally). In the first step of tractometry algorithm, all fibers (components of tract bundle) are resampled to the equal number of segments. In the second step, mean trajectories of individual tracts called centroids

are found and each segment of each streamline is assigned to the closest segment of the centroid. Selected metric(s) is then averaged across all assigned segments. Reconstruction of the human cerebrospinal neuronal tract and tractometry using TractSeg software is shown in Figure 26.

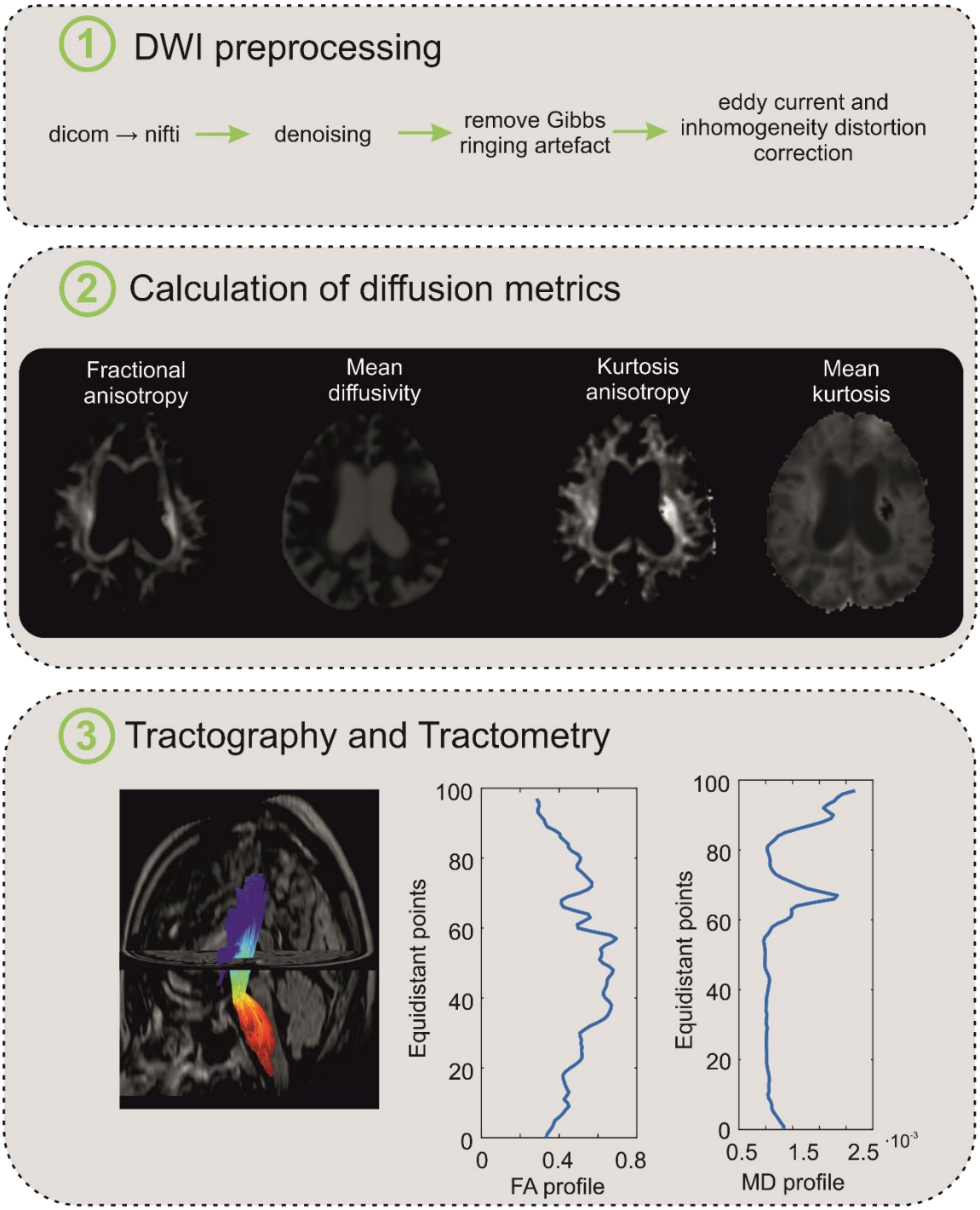

Figure 27. Scheme of proposed algorithm pipeline for analysis of variations in white matter neuronal tracts

5.2.Methods

Our pipeline proposed for the analysis of white matter tracts variations is described in this chapter. The proposed pipeline consists of three main blocs (see Figure 27); diffusion MRI preprocessing, calculation of diffusion metrics, and tractography together with tractometry. Diffusion data with at least three b-values (b0 + two other) is needed as an input for the algorithm. Outputs of the pipeline are maps of 7 diffusion metrics (see above), 72 reconstructed tracts, and profiles of all metrics along each tract. The list of Linux OS commands used in the algorithm is shown in Figure 28 as an example.

5.2.1.Diffusion MRI data preprocessing

Diffusion-weighted MRI data are preprocessed in 5 consecutive steps before tractography.

Conversion to NIfTI

MRI images are converted from Dicom to NIfTI data format using the freely available tool dcm2niix (Li *et al.*, 2016). Data quality is visually checked before further analysis and substandard images (or whole patients) are excluded from further analysis. The reason for exclusion is in majority of cases lack of patient cooperation during the measurement leading to severe motion artifacts.

Denoising

Denoising and removal of Gibbs ringing artifact are performed using free software MRtrix (Tournier *et al.*, 2019).

Noise reduction in the MRtrix tool is based on lowering redundancy in the image using principal component analysis (PCA). It uses methods of matrix theory and prior knowledge that the eigenspectrum of random covariance matrices is described by the universal Marchenko-Pastur distribution. For more details see the official MRtrix documentation at https://mrtrix.readthedocs.io/en/latest/dwi_preprocessing/denoising.html (cited: 19.6.2020).

```
dcm2niix -o outputDirectory dicomDirectory                                  # conversion from dicom

mrconvert dwi_rawData.nii dwi_rawData.mif -fslgrad bvecs bvals              #conversion to .mif

dwidenoise dwi_rawData.mif 01_denoise.mif                                   #denoising

mrdegibbs 01_denoise.mif 02_gibbs.mif -axes 0,1                             #gibbs art. removal

dwipreproc -pe_dir PA -rpe_none -eddy_option " --slm=linear" 02_gibbs.mif 03_preproc.mif   #MRtrix preprocessing

mrconvert 03_preproc.mif -export_grad_fsl bvecs_eddy bvals_eddy 03_preproc.nii.gz          #conversion to nifti

bet 03_preproc.nii.gz 04_preproc_bet.nii.gz -f 0.2 -m -F                    #brain extraction

calc_FA -i 04_preproc_bet.nii.gz -o 05_FA.nii.gz --bvals bvals_eddy --bvecs bvecs_eddy --brain_mask 04_preproc_bet_mask.nii.gz   #calculation of FA map

flirt -ref MNI_FA_template.nii.gz -in 05_FA.nii.gz -out 06_FA_MNI.nii.gz -omat FA_2_MNI.mat -dof 6 -cost mutualinfo -searchcost mutualinfo   #calculation of transformation from diffusion to MNI space

flirt -ref referenceAtlas -in 04_preproc_bet.nii.gz -out 07_DWI_MNI.nii.gz -applyisoxfm 1,1,1 -init FA_2_MNI.mat -dof 6 -interp spline   #tranform. to MNI

flirt -ref referenceAtlas -in 04_preproc_bet_mask.nii.gz -out 07_brainmask_MNI.nii.gz -applyisoxfm 1,1,1 -init FA_2_MNI.mat -dof 6 -interp nearestneighbour   #transform of brain mask to MNI

rotate_bvecs -i bvecs_eddy -t FA_2_MNI.mat -o bvecs_MNI                     #transform bvecs to MNI

#===========metrics calculation============================

#bvecs must be transposed to DKE format

./run_dke.sh <mcr_directory> <argument_list>                                #run DKE, create metrics maps


#===========tractography=====================================

TractSeg -i DWI_MNI.nii.gz --bvals bvals_MNI --bvecs bvecs_MNI --brain_mask brainmask_MNI.nii.gz -o tractseg_output --raw_diffusion_input --output_type tract_segmentation   #peak FODs calculation

TractSeg -i tractseg_output/peaks.nii.gz -o tractseg_output --output_type endings_segmentation   #ending/begin. masks

TractSeg -i tractseg_output/peaks.nii.gz -o tractseg_output --output_type TOM   #TOM calculation

Tracking -i tractseg_output/peaks.nii.gz -o tractseg_output --nr_fibers 5000 --tracking_format tck   #fiber tracking

Tractometry -i tractseg_output/TOM_trackings/ -o tractseg_output/Tractometry_metric.csv -e tractseg_output/endings_segmentations/ -s dtifit_MNI/dti_metric.nii.gz --tracking_format tck   #tractometry
```

Figure 28. List of commands used in the algorithm for analysis of white matter tracts (syntax for Linux OS)

Removal of Gibbs ringing artifact

Gibbs ringing artifact (or truncation artifact) appears in MRI image as a series of lines (echoes) parallel to high contrast boundaries as brain-skull interface. It is the result of finite sampling

of MR image unable to catch high frequencies of fast intensity changes. Ringing artifacts appear in both phase-encode and frequency-encode directions. Gibbs artifact can be removed by the method of local subvoxel-shifts which is implemented as part of MRtrix free tool. For more details see the official MRtrix documentation at https://mrtrix.readthedocs.io (cited: 19.6.2020).

Eddy current and field inhomogenity distortion correction

Eddy currents are loops of electrical current that are induced in the brain tissue as a result of changing magnetic field. Eddy currents lead to spatial distortion of MR images in the direction of the current. For distortion correction, MRtrix command *dwifslpreproc* is used in this pipeline. It unifies two main algorithms for distortion correction, *eddy_correct* and *topup* from FSL tool. Six pairs of b0 images measured in opposite phase encoding are used for field inhomogenity correction. For more details see the official MRtrix documentation at https://mrtrix.readthedocs.io (cited 19.6.2020).

Spatial normalization to MNI space

All diffusion images are normalized to MNI (Montreal Neurological Institute) coordinate system in this pipeline. This step is necessary for further analysis using the TractSeg tool. Map of fractional anisotropy (FA) of DWI scans is aligned with FA atlas from human connectome project (http://www.humanconnectomeproject.org/) by *FLIRT* FSL command. The resulting transformation matrix is applied to all diffusion scans then.

5.2.2. Calculation of diffusion metrics

Seven diffusion metrics (see Figure 29); isotropic diffusion map (DWI), fractional anisotropy (FA), mean diffusivity (MD), diffusion kurtosis anisotropy (KA), and mean, radial, and axial diffusion kurtosis (MK, Kax, Krad, respectively) are calculated in this step of the proposed pipeline using Diffusion Kurtosis Estimator (DKE) free software (Tabesh *et al.*, 2011). For more details about used diffusion, metrics see chapter 5.1.3

5.2.3.Tractography

Tractography followed by tractometry of 72 neuronal tracts (list of tracts at https://github.com/MIC-DKFZ/TractSeg, cited 24.6.2020) is performed by TractSeg software

(Wasserthal, P. Neher and Maier-Hein, 2018). The resulting tractography of the fronto-pontine neuronal tract and tractometry profiles of six diffusion metrics are shown in Figure 30.

5.3.Results

The behavior of the established pipeline was tested on both artificial and real human data. The results are described in this chapter.

5.3.1. Evaluation of pipeline behavior in pathological conditions

TractSeg tool works well in healthy patients, however, its performance in patients with brain pathologies was not yet reported. It was crucial to explore and evaluate its behavior in non-standard or pathological conditions to be sure with clinical interpretations based on TractSeg outputs in our study. We have performed several tests on human brain MRI scans that were either artificially modified or affected by real pathology. Based on these tests, we have described the behavior of TractSeg software in an environment of non-standard (ischemic) brain data.

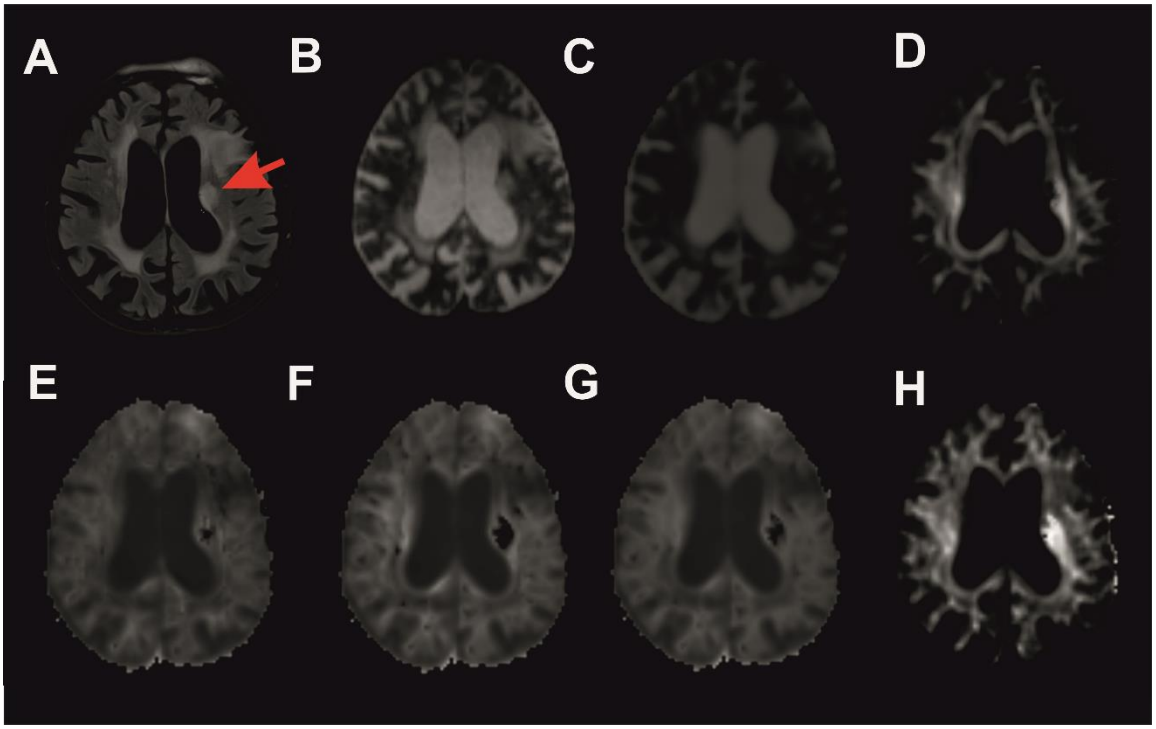

Figure 29. Diffusion metrics of a patient with cerebral ischemia (ischemic lesion is marked by an arrow). (A) structural FLAIR image with a visible ischemic lesion, (B) b0 diffusion image and metrics of (C) mean diffusivity, (D) fraction anisotropy, (E) axial kurtosis, (F) radial kurtosis, (G) mean kurtosis, (H) kurtosis anisotropy

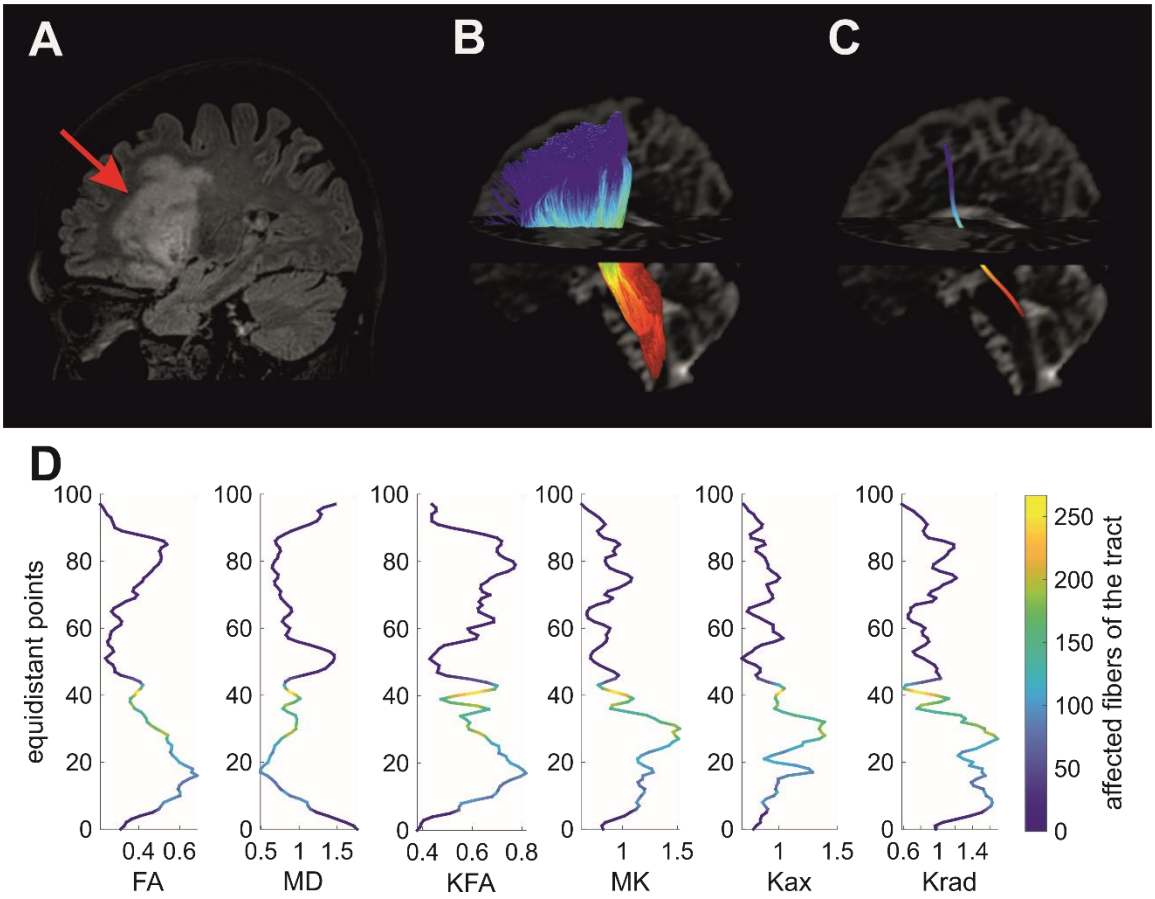

Figure 30. Result of proposed pipeline applied at a patient with cerebral ischemia. (A) anatomical FLAIR MRI of the patient with severe cerebral ischemia (marked by an arrow). (B) Reconstruction of fronto-pontine tract going through brain regions affected by ischemia. (C) Reconstruction of centroid as the mean trajectory of the tract. (D) Tractometry – profile of six diffusion metrics along the tract centroid (MD mean diffusivity, FA fraction anisotropy, Kax axial kurtosis, Krad radial kurtosis, MK mean kurtosis, KFA kurtosis fraction anisotropy). Colormap shows how severely was individual parts of the tract affected by cerebral ischemia (the total number of fibers in the tract was 5000)

Tested neuronal tracts

The right fronto-pontine tract (FPT) and right inferior longitudinal fasciculus (ILF) were used for further testing of the algorithm. Both are long fascicles that are not crossing between hemispheres. Therefore, they can be easily disrupted by artificial obstruction. Both tracts have also well-defined beginnings and ends. ILF is localized occipitotemporally. It starts in the anterior temporal lobe and ends in the occipital lobe, running along the lateral ventricle. FPT starts in the brainstem and climbs diagonally to the frontal cortex. Reconstruction of both tracts in healthy human control is depicted in Figure 31.

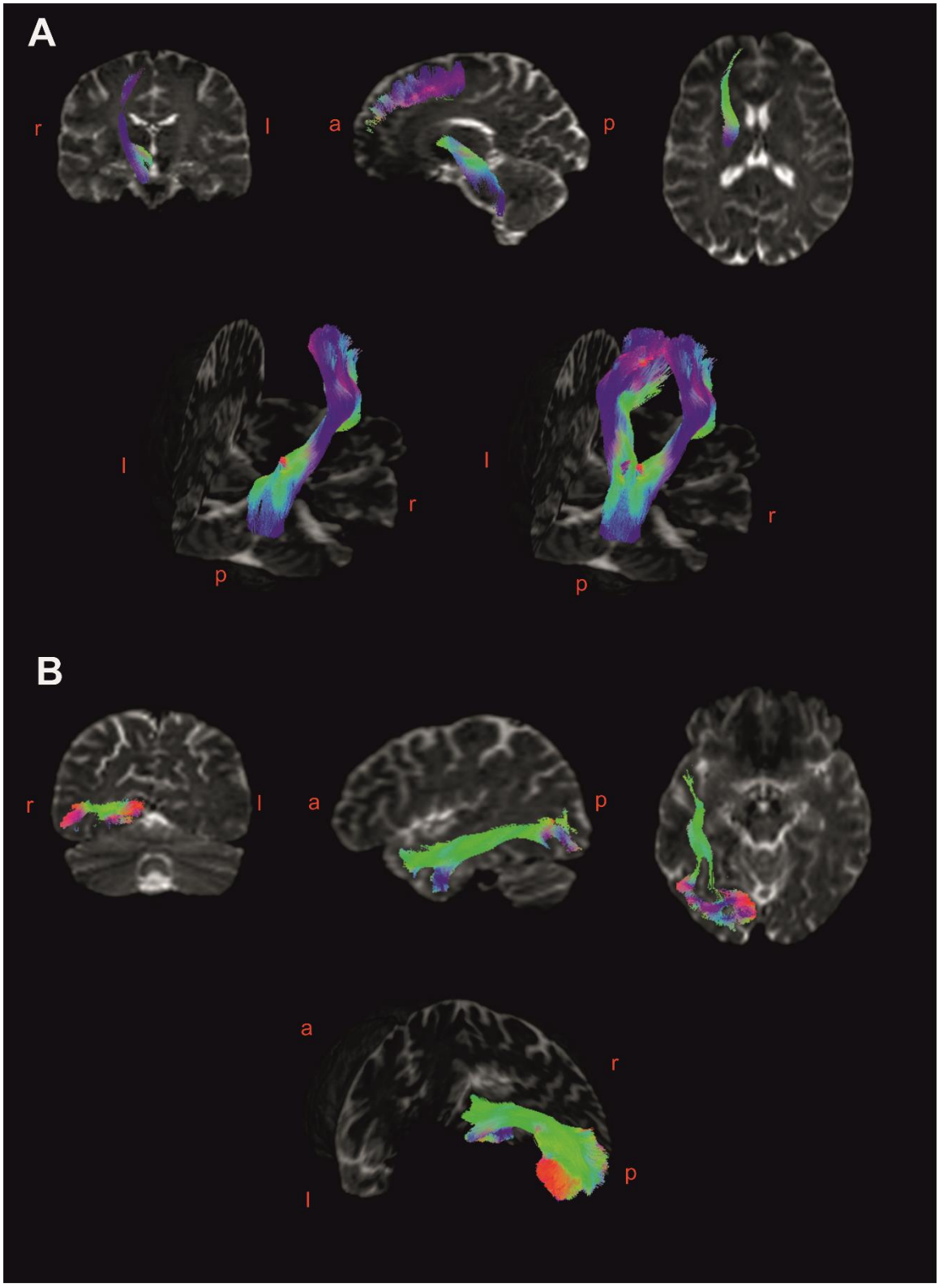

Figure 31. (A) reconstruction of right fronto-pontine white matter tract (in the last image right FPT together with left FPT) and (B) right inferior longitudinal fasciculus in healthy human control. Anatomical directions r = right, l = left, a = anterior, p = posterior. Color codes directionality of the fibers (red for right-left, blue for dorsal-ventral, and green for anterior-posterior orientation)

Peaks

Fiber Orientation Density Function (fODF) are the results of spherical deconvolution (see chapter 5.1.5) characterizing the direction of diffusion in the tissue. fODF serves as direct input to Tract Orientation Mapping (TOM) tractography, a technique used in our study for white matter reconstruction. fODF is usually depicted as a single vector called peak for every voxel in the brain. Every peak is described by orientation, length, and color. Length of the vector demonstrates the strength of the diffusion in a direction corresponding with the direction of the fODF and marked by a specific color of the vector (in color code system where red is for right-left orientation, blue for dorsal-ventral, and green for anterior-posterior orientation). In case that more than one dominant direction of the diffusion within a single voxel is detected, more peaks are grouped in this voxel. An example of fODF peaks is shown in Figure 32 A. Its directionality is visible in the right detailed view with highly oriented red peaks corresponded to fibers coming out of the corpus callosum.

To explore how the TractSeg technique can deal with non-physiological obstacles, we have manually added a circular region with homogenous intensity into healthy diffusion MRI image. The resulting peaks are shown in Figure 32 (B-D). When data from the artificial region were removed completely (changed to zero) no peaks were created (Figure 32 D). In Figure 32 B, a homogenous region with high intensity was artificially inserted. High-intensity values mimic an image similar to the ischemic lesion, however, the real ischemic lesion is, in general, less homogenous. The resulting peaks describe an absolutely anisotropic environment, as it points to all three main directions with the same magnitude. In Figure 32 C, an obstacle with an intensity equal to the mean intensity of the brain tissue was used. In this case, peaks manifest similar behavior as in the high-intensity region, however, they are less intense in the anterior-posterior (green) direction.

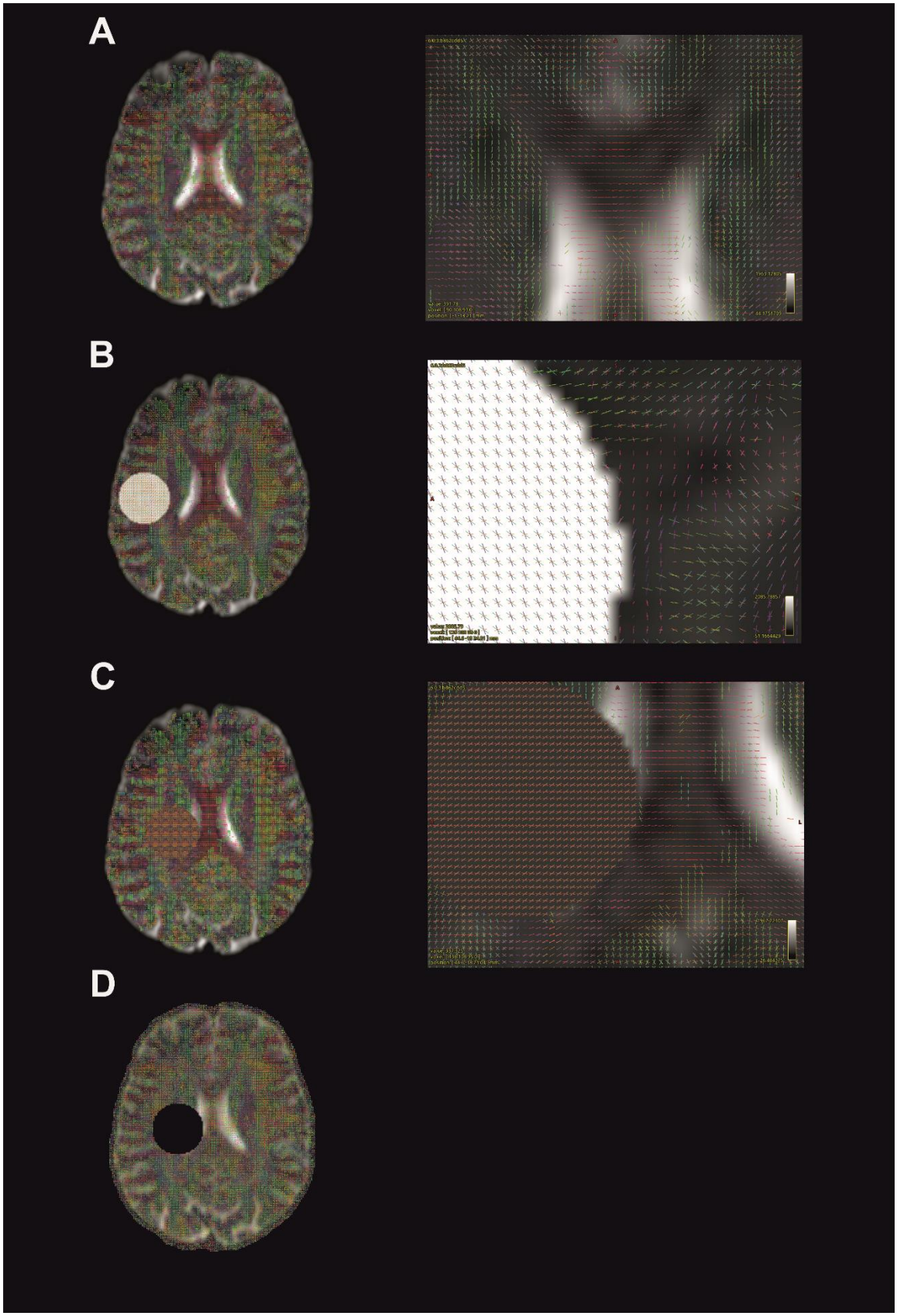

Figure 32. fODF peaks in (A) healthy control, (B) homogenous region with high-intensity values, and (C) homogeneous region with intensity values corresponding to common brain tissue. (D) In the case of the region with missing data (zero intensity), no peaks were created

An artificial obstacle in tract trajectory

To assess the behavior of the TractSeg algorithm in presence of non-physiological anomalous tissue in the trajectory of the reconstructed tract an artificial obstacle was added. The obstacle has a form of a "wall" (entire image slice or slices in the coronal plane) of variable thickness and with constant image intensity set to zero, mean intensity of the brain tissue, and abnormally high intensity, respectively (same as tested above in Figure 32).

The artificial obstacle was put in the middle of the trajectory of fronto-pontine tract. The results of the test are shown in Figure 33. In the case of thin obstacle (5 mm thick, Figure 33 A-C) no effect on tract reconstruction was observed. TractSeg algorithm was able to bridge the obstacle maintaining the physiological trajectory of the tract and continue on the other side in the same way as in a healthy control brain (see Figure 31 A for comparison).

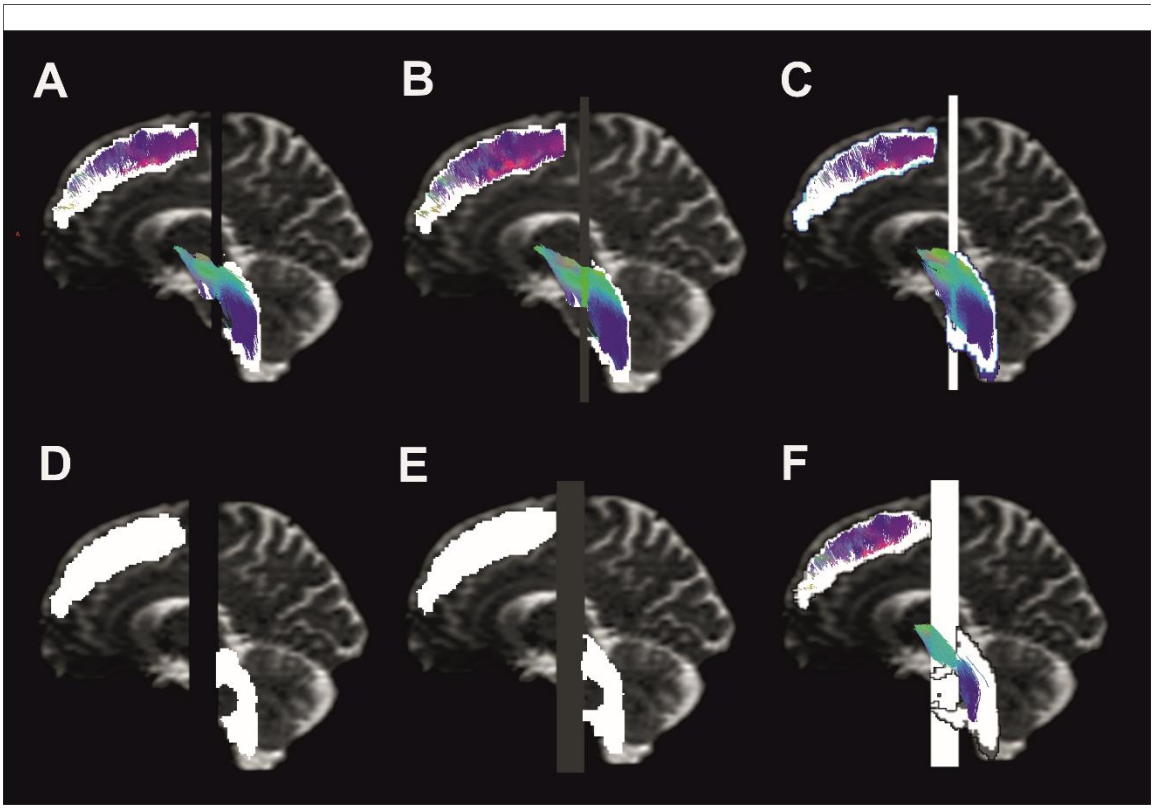

Figure 33. An artificial obstacle in the shape of a "wall" in the trajectory of fronto-pontine tract. Image intensity of the obstacle was set to zero, mean intensity of brain tissue and abnormally high intensity, respectively. Beginning and ending masks for tract reconstruction are indicated by white regions in the brain stem and the cortex, respectively. (A-C) 5 mm thick obstacle does not affect tract reconstruction, which was performed without disruption in the same way as in healthy control (see Figure 31 A) for all three intensities. (D-E) 15 mm thick obstacle with zero and mean image intensity interrupts tract reconstruction entirely. (F) In contrast to (D) and (E), TractSeg was able to reconstruct the tract across a 15 mm thick obstacle with abnormally high image intensity. The amount of fibers overcoming an obstacle is lower than in healthy tractography, however, the trajectory of the tract was sustained

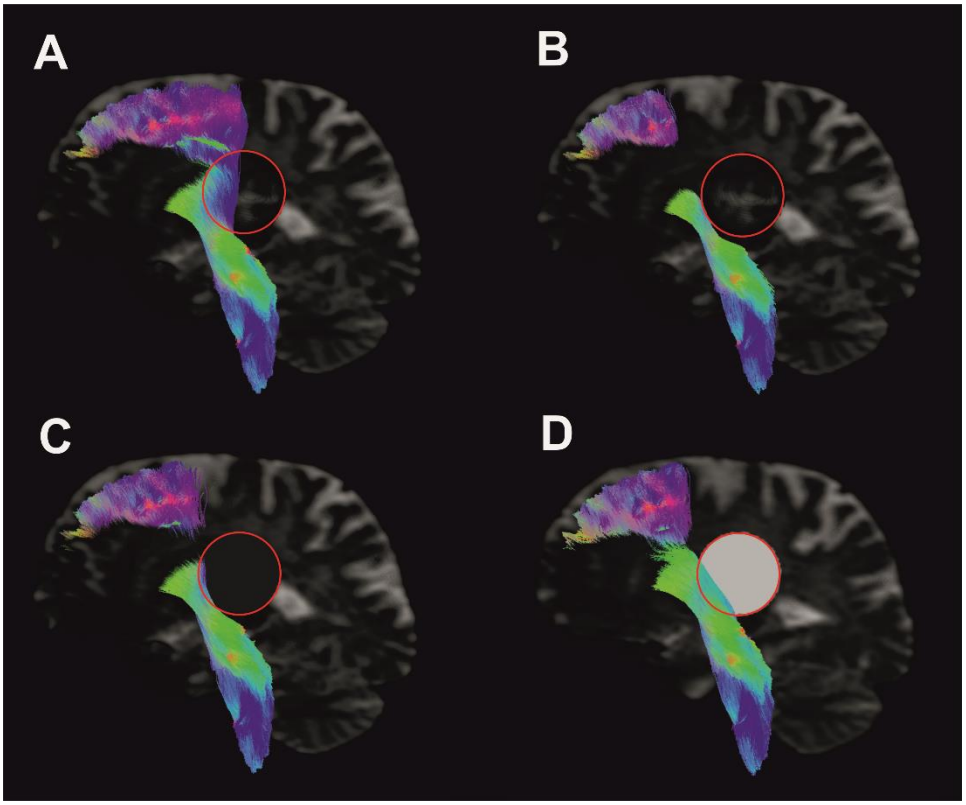

Figure 34. TractSeg behavior during the reconstruction of fronto-pontine tract in presence of an obstacle in the shape of a sphere (marked by a red circle). (A) Reconstruction in healthy control without obstruction. The spherical obstacle with (B) zero image intensities, (C) mean brain intensity, and (D) abnormally high intensities, respectively

In case of a more severe 15 mm thick obstacle (Figure 33 D-E) algorithm was able to finish reconstruction only in case of the obstacle with abnormally high image intensity, where the physiological trajectory of the tract across the obstacle was sustained, however, the number of reconstructed fibers was lower than in healthy tractography. In the cases of obstacles with zero or mean intensities, TractSeg wasn't able to reconstruct any tract.

Similarly, TractSeg behavior during the reconstruction of FPT in presence of an artificial obstacle in the shape of a sphere was tested. The spherical obstacle was manually put into diffusion MR image into the trajectory of FPT. In case of an obstacle with zero image intensity (Figure 34 B) reconstructed tract avoid the artificial region completely and thus it wasn't able to reach parts of the cortex "behind" (from the perspective of tract trajectory heading from the brain stem to the cortex) the obstruction. In the case of the sphere with intensities similar to the mean intensities in the brain tissue (Figure 34 C), TractSeg was able to generate tract fibers across the surface of the obstacle (1-2 mm) but avoid deeper parts of the sphere. In the case of the sphere with abnormally high intensities (Figure 34 D), reconstructed fibers cross the obstacle also in deeper layers but not completely. By comparing the results in Figure 34 it is

obvious that deeper penetration into the obstacle means a higher chance to navigate fibers into parts of the cortex that are hidden behind the obstacle.

Figure 35 shows TractSeg results for input image with an obstacle in the shape of a ring instead of a filled sphere. Such shape is closer to real ischemic lesions, which are often composed of inner parts with anisotropic diffusion and outer glial scar with restricted diffusion. We have used two different thicknesses of the ring wall. In the case of a thinner ring with a 5 mm thick wall, almost no change in tractography was observed. However, the thicker ring with a 10 mm wall prevents the reconstruction of the fibers leading to part of the cortex behind the obstacle. This behavior is consistent with results for other types of obstacles described above.

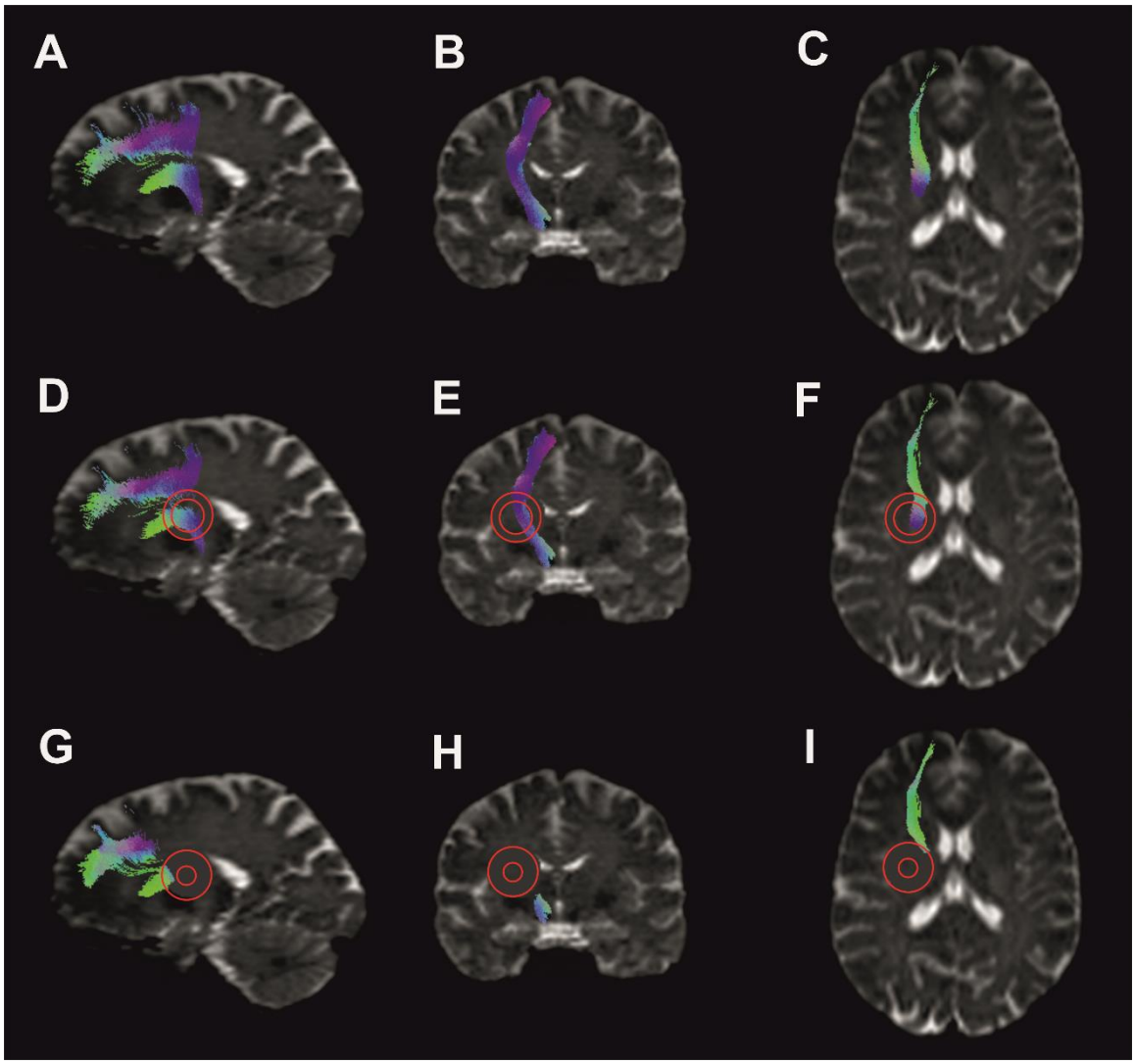

Figure 35. Reconstruction of fronto-pontine tract in (A) healthy control, (B) with an artificially added obstacle in the shape of a ring with 5 mm thick wall, and (C) 10 mm wall. The thinner ring has almost no effect on tractography, however, the thicker one prevents the reconstruction of the fibers leading to part of the cortex behind the obstacle

Location of the obstacle matters

A crucial step in the TrackSeg tractography algorithm was so far omitted in our testing. Before Tract Orientation Maps (TOMs) are calculated from peaks (voxel-wise fODF – fiber oriented distribution functions), masks of probable trajectories of individual tracts are assessed based on anatomical atlas. The probable trajectory is estimated between the anatomically defined mask of tract beginning and ending (for example FPT stars in the pons Varoli and ends in the frontal cortex). During tract reconstruction step mask of beginning serves as a seed for fiber tracking (all tract fibers must start here) and the ending mask serves as a termination (only fibers that reach the ending mask are included as a result of the reconstruction). Location of pathological obstacle in tract pathway in relation to beginning/ending mask plays a crucial role in the result of the tractography. There are three possible relations between masks and obstacles; 1) Obstacle is inside begging mask. I.e. part of the mask is behind the obstacle, part ahead (from the perspective of tract trajectory), 2) obstacle is between the beginning and ending mask, or 3) obstacle is localized inside the ending mask.

TractSeg tract reconstruction algorithm behavior according to the position of the obstacle was tested. Figure 36 (B-C) shows reconstruction in presence of a 5 mm thick obstacle in two different positions. In the first case (Figure 36 B), the obstacle completely separates the begging and ending mask of the tract and thus completely interrupts the whole reconstruction of the tract. In the second case (Figure 36 C), the obstacle leads through the middle of the beginning mask and thus split the mask into two parts, one separated from the ending mask by the obstacle and one not. In this second scenario, reconstruction from the not-separated part was performed in the same way as in healthy control. Moreover, the algorithm was able to calculate tract fibers also from the separated part of the beginning mask, i.e. across the obstacle. The same behavior was observed also in the case of a 5 mm thick obstacle with image intensity equal to mean values of the common brain tissue and abnormally high values (data not shown).

Different behavior was observed in presence of the thicker (15 mm) obstacle. Reconstruction was completely interrupted when obstacle separates beginning and ending masks (same case as Figure 36 B) regardless of obstacle intensity (zero, mean or high values). In the case of obstacle with zero (Figure 36 D) and mean (Figure 36 E) intensity leading through the beginning mask, tract fibers were reconstructed only from a non-separated part of the mask while the separated part remain unconnected. Only in the case of the thick obstacle with high intensities (Figure 36 F), the algorithm was able to calculate also tract fibers crossing the obstacle. Tractogram

(profile of Fraction Anisotropy (FA) and Mean Diffusivity (MD) along reconstructed tract) resulting from such reconstruction is shown in Figure 36 I. It contains information from both the obstacle together with information from a healthy part of the tract. The high intensity of the obstacle manifests in the tractogram as low FA and high MD, suggesting high isotropy of diffusion in the corresponding part of the tract.

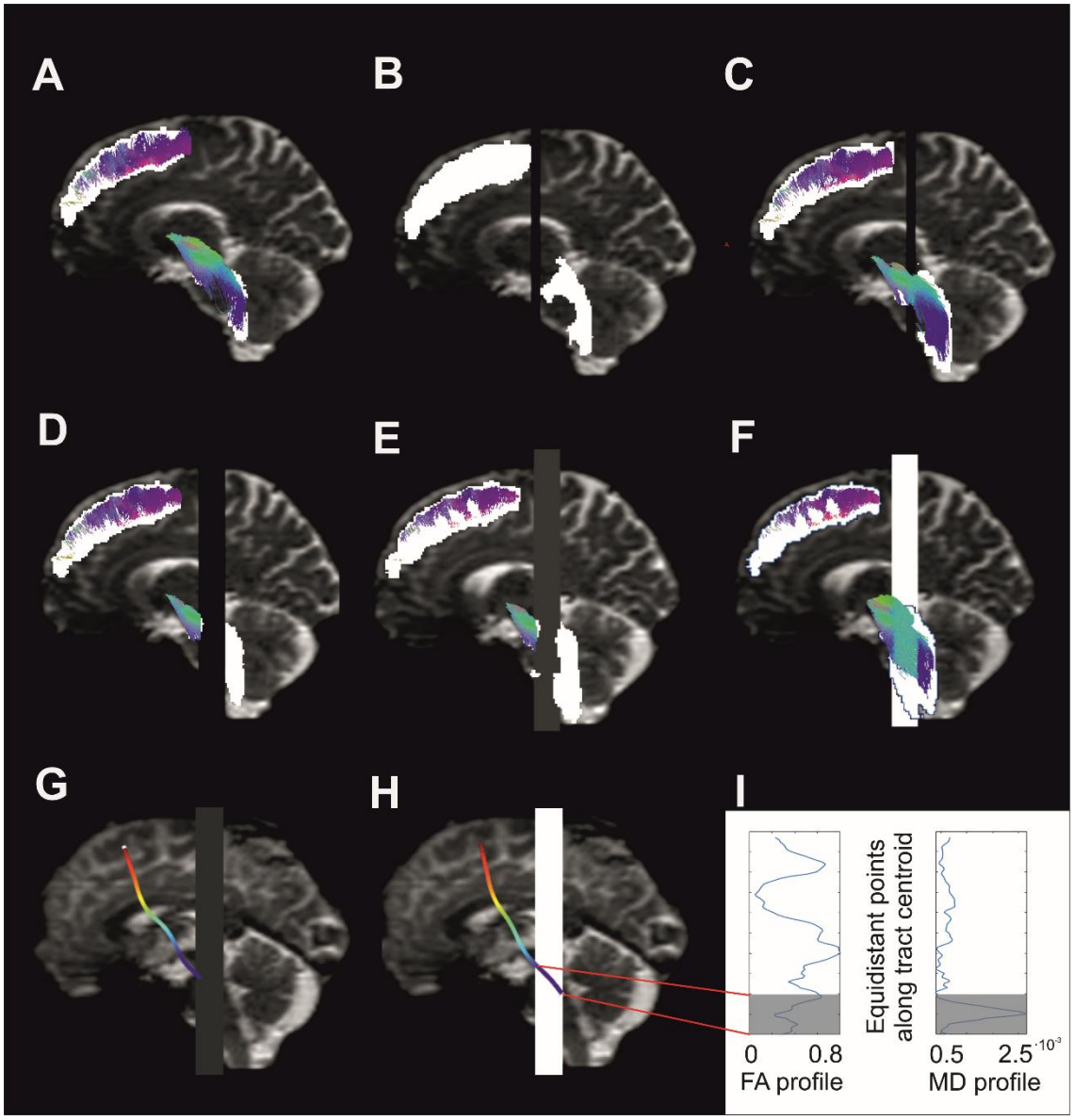

Figure 36. Demonstration of TractSeg behavior according to the location of the artificial obstacle. (A) Fronto-pontine tract (FPT) reconstruction in healthy control. (B-C) 5 mm thick obstacle artificially inserted into MR images. (B) obstacle completely separates the beginning and ending masks of the tract and thus completely interrupts the whole reconstruction of the tract. (C) obstacle leads through the middle of the beginning mask and thus split the mask into two parts. No effect of the obstacle on the tract reconstruction was observed in this scenario. (D-F) FPT reconstruction in presence of 15 mm thick obstruction with image intensity equal to (D) zero, (E) mean value of common brain tissue, and (F) abnormally high value. (G-H) Centroid (mean trajectory) of reconstructed tracts. (I) Tractogram of FPT tract leading across the high-intense obstacle

Conclusion of the algorithm behavior test

Several important notes about the TractSeg algorithm behavior that should be taken into account during the interpretation of algorithm results were revealed by our tests. Firstly, it is important to pay close attention to the location of the ischemic lesion in relation to the beginning/ending masks of studied tracts. When part of the beginning mask is affected by an ischemic lesion (or any other pathological anomaly), the TractSeg algorithm is likely to ignore this part placing the beginning of the tract behind it. It might be misinterpreted in a way, that no neuronal fibers remained in the affected region and tract was shortened due to the pathology, however, the algorithm itself doesn't provide any proof for such a statement. Similar misinterpretation can be made when the ischemic lesion is located directly in the way of the reconstructed tract (or its part). In the case when the algorithm can't "bridge" such pathology towards the side of the ending mask of the tract, it might completely omit tract fibers behind pathology (in the imaginary shade of the pathology). This could be falsely interpreted as a reduction of neuronal fibers, however, such results only show the inability of the algorithm to mathematically connect separated regions.

Tests with the use of the obstacles in the shape of the wall reveal an issue with an opposite impact to data interpretation. TractSeg algorithm tries to reconstruct tracts following the pattern defined by an anatomical atlas from healthy brains. When the obstacle (or pathological anomaly as an ischemic lesion) has high intensities in diffusion images and is not too wide, the algorithm, in a pursue to follow the given pattern, can bridge the problematic part ignoring the pathology and thus information about tract interruption can be omitted. Therefore, it is always recommended to compare tractography results with real diffusion parameters with consideration of pathology location.

Only fronto-pontine tract and inferior longitudinal fasciculus were used for demonstration of TrastSeg behavior in this chapter, however, other brain tracts were also tested and similar behavior as described in the case of FPT and ILF was observed.

6. Discussion

The aim of this thesis was to develop a battery of tools for the analysis of our clinical MRI data. Three main objects of interest were followed in this study; 1) Development of a semiautomatic algorithm for detection of lesion of cerebral ischemia, 2) design and implementation of a method for assessment of blood-brain barrier (BBB) impairment from a contrast MRI, and 3) tailoring, adaptation, and testing of a pipeline for analysis of longitudinal variations in white matter neuronal tracts from diffusion MRI.

The first part of this thesis (chapter 3) is focused on the detection of lesion of cerebral ischemia from conventional anatomical MRI sequences; FLAIR and DWI. Such segmentation is a crucial step in the analysis of the relationship between structural and (dys-)functional properties of the post-ischemic brain and is an indispensable prerequisite for any correlation between ischemia and other phenomena in the brain such as edema, hemorrhage, localization of epilepsy, BBB dysfunction, neuronal loss, etc. Many algorithms for automatic detection of the ischemic lesion were already developed (for more details see 3), however, with the increasing complexity of the used algorithm more caution to the interpretation of the results must be paid as more "black-box" operations are presented in the algorithm. Also, all of the currently available algorithms should be specially tuned for individual datasets (Ito, Kim and Liew, 2018). Based on those facts, we have decided to develop our own semi-automated approach assisting during the manual delineation, instead of using a fully-automatic approach. Our approach is still time-consuming (although less than fully manual delineation) and still needs a skilled neurologist, however, obtained results are reliable and the interpretation of the results is straightforward. Nevertheless, the development of a fully automated approach tuned and tested for our dataset would be extremely beneficial, as it would shorten the time necessary for the segmentation and lower the workload of neurologists. This provides a huge space for further improvement of the proposed method.

Results of the proposed detection algorithm were compared with manual delineation (current golden standard) in 60 patients from our dataset in subchapter 3.2.1. The comparison shows that the proposed algorithm has 94 % sensitivity but rather overestimates the volume of the lesion (in median 1.3 times) resulting in lower (70 %) precision. This is caused by algorithm step 4, where VOI with lesional tissue is preselected before segmentation. When the lesion is

located in the proximity of brain ventricles, the surface of the brain, or other tissue with hyperintense MR image (as older lesions or gliosis) such tissue is false positively detected as part of the lesion. The gravity of this overestimation can be reduced by manual correction of algorithm results. The effect of the overestimation is also often further reduced during consecutive image processing. Our studies are often focused on specific brain structure (such as cortex, basal ganglia, thalamus, etc.) that is specifically masked out from the rest of the brain using the results of brain parcellation. False-positively detected tissues not belonging to the studied structure are therefore removed as a result of such masking.

The proposed algorithm was used in the analysis of 175 patients suffering from cerebral ischemia from our clinical cohort. The algorithm was able to detect an ischemic lesion in all patients and the ischemic lesion was characterized based on algorithm results. We have demonstrated the spatial distribution of structural versus diffusional changes of the tissue over the lesion Moreover, we have described volumetric changes of the lesion between the acute and subacute phases of ischemia and reported growth of structural changes (in FLAIR) without volume alteration of diffusion changes (in DWI) (chapter 3.2.2). The proposed algorithm has proven to be useful in the analysis of cerebral ischemia from MRI as it can help uncover unknown phenomena behind the disease.

The second part of the thesis (chapter 4) describes an algorithm for the assessment of blood-brain barrier (BBB) disruption in the brain using MRI with a gadolinium contrast agent. The algorithm was adopted from (Chassidim *et al.*, 2013) and modified for the purpose of our dataset. This part of the thesis was published in (Kala *et al.*, 2017). The performance of the original algorithm was further improved by adding series of equations, that refine the detection of voxels of tissue with impaired BBB. We have also developed a parameter called the Extravasated Gd (gadolinium), that describes the severity of BBB dysfunction.

The proposed algorithm was used in part of our clinical study on 60 patients after cerebral ischemia and provided valuable insight into the relationship between the ischemic lesion and BBB impairment. In chapter 4.3.1, we have reported a strong correlation between volumes of both phenomena (lesion and BBB impairment). Further, we have described in detail the spatial distribution of BBB impairment over postischemic tissue. We have shown that BBB impairment is presented dominantly inside the ischemic lesion, more precisely in regions corresponding to ionic or vasogenic edema. Also, we have reported not negligible amount of Extravasated Gd outside the ischemic lesion and we have suggested a possible relationship with

acute ionic edema. As the pathophysiology of BBB disruption and its consequences are still not fully explored, such detailed analysis is an important step in the understanding of this phenomenon.

Analysis of BBB disruption is crucial also in the study of hemorrhage and hemorrhagic transformation (HT, blood leakage into the brain) after cerebral ischemia. Because HT represents severe and feared complications of reperfusion therapies (most common post-ischemic treatment), it is an important target of our future studies, where a developed pipeline for BBB analysis will serve as an essential tool.

The tractography, as a tool for segmentation and analysis of neuronal tracts, is the main subject of the third part of the thesis (chapter 5). The chapter presents an in-house tailored algorithm pipeline implemented for preprocessing and analysis of diffusion MRI data. We have adopted and combined several freely available software for purpose of this pipeline; MRtrix (Tournier *et al.*, 2019), dcm2niix (Li *et al.*, 2016), and FSL tool were used for data preprocessing, Diffusion Kurtosis Estimator (Tabesh *et al.*, 2011) for calculation of diffusion parameters and TractSeg software (Wasserthal, P. Neher and Maier-Hein, 2018) for tracts reconstruction and tractometry. The whole pipeline was tested on human brain data from both, healthy control and patients with cerebral ischemia, acquired in Motol hospital using two different MRI scanners; 3T Siemens Vida and 1.5T Phillips Ingenia scanner.

Tractography and tractometry (profile of diffusion parameters along the tract) appear to be very powerful tools for the detection of cellular changes of brain tissue that are the initial cause of functional changes and pathologies. The developed pipeline will be used in our future studies for monitoring variations in the brain tissue after cerebral stroke. We hypothesize that a better understanding of edematous processes (that manifest, among other things, by changes of diffusion parameters) by detailed analysis of diffusion MRI by proposed pipeline increases the chance of post-ischemic hemorrhagic transformation prediction. Another future use of our pipeline will be focused on variations in thalamocortical neuronal tracts after cerebral stroke with the aim to uncover pathophysiological processes leading to post-ischemic epilepsy.

The behavior of neuronal tracts reconstruction by the TractSeg tool on artificially modified human MRI data was further tested (chapter 5.3.1). The reason for such testing was to better understand how the software behaves in a non-standard situation such as in presence of structural pathologies (ischemic lesion, focal cortical dysplasia, tumor, etc.) intending to

correctly interpret those results at the cellular level. The used reconstruction technique is "only" a mathematical procedure fulfilling predefined tasks which were designed for. The numerical results are therefore closely bound to conditions of the environment in which were calculated. I.e. in the standard situation of healthy human brain tractography results can be interpreted in the standard way, although, when the environment is changed (for example by the presence of pathology), the results must be interpreted with caution. Therefore, prior knowledge of the algorithm behavior in well-defined (artificial) non-standard situations can make such an interpretation process significantly easier and more reliable.

In our tests, we have modified healthy brain data by the addition of artificial obstacles of different shapes, intensities and into different locations. We have reported the crucial role of obstacle location in relation to the beginning/ending masks of studied tracts. The TractSeg algorithm shows in general robust and stable results, however, in some of the reported cases, with varying size of the obstacle and the exact way how the original tract was disrupted by the obstacle, the algorithm provides too optimistic or too pessimistic results. Too optimistic results were shown in cases when the algorithm reconstructs tracts across the tissue, where the presence of healthy neuronal fibers is from physiological reasons unlikely (in cavernoma or glial scars after cerebral ischemia). On the other hand, too pessimistic results were reported, where the algorithm wasn't able to bridge tract across the obstacle and no neuronal fibers were found in the imaginary shade behind the obstacle. This situation can be also easily misinterpreted, because the results of the algorithm suggest total loss of fibers, although it is more likely "only" loss of connection between separated parts of the tract but not the absence of fibers in not-affected tissue. For more details see chapter 5.3.1. Described findings impel to interpret tractography results with caution and with attention to original data.

7. Conclusion

A battery of three algorithm pipelines for processing and analysis of data from magnetic resonance imaging was developed and tailored in this thesis. The first algorithm was designed to semi-automatically detect lesion of cerebral ischemia from FLAIR and DWI MRI. The algorithm was tested on human MRI data and its performance was compared with manual delineation by a neurologist (current golden standard). The sensitivity of the algorithm is 94 % with 70 % precision. The developed algorithm was further used in part of our clinical study where the spatial distribution of structural versus diffusional changes of the tissue over the lesion was described together with volumetric changes of the lesion between the acute and subacute phase of ischemia. Results of the study are concluded in chapter 3.2.

The second algorithm was developed for the analysis of blood-brain barrier disruption from MRI with a contrast agent. Results of the algorithm provide valuable insight into the relationship of BBB impairment and other pathophysiological processes in the brain, i.e. cerebral stroke, edema, hemorrhage, etc. The algorithm was used in our clinical study on 60 patients after cerebral ischemia. We have described in detail the spatial distribution of BBB impairment over postischemic tissue, we have shown that BBB impairment is presented dominantly inside the ischemic lesion, but also we have reported not negligible amount of Extravasated Gd outside the ischemic lesion where we have suggested a possible relationship with acute ionic edema.

The third introduced pipeline was tailored for the analysis of variations in white matter tracts. The pipeline consists of robust data preprocessing, calculation of important diffusion parameters of the tissue, and of tractography and tractometry step, where individual neuronal tracts are reconstructed and profile of diffusion parameters along those tracts is calculated. The proposed algorithm was tested on human MRI of both healthy controls and patients after stroke. The tractography algorithm was further tested on artificially modified data with the aim to describe its behavior in non-standard conditions (as in presence of brain pathology). Interpretation of results in different scenarios of input data was thoroughly discussed (Chapter 5.3.1).

The thesis accomplished all stated goals and fully fulfilled the thesis assignment.

7.1. Future work

In the first part of the thesis, our aim was to develop a method, that helps the radiologist to demark ischemic lesion in MR images mostly by reducing the time needed for this procedure. As a result, we have developed an algorithm pipeline that speeds up the demarcation process significantly, however, the presence of a skilled radiologist is still necessary. Fully automation of the algorithm with an increase or at least maintenance of the current precision is the next step in saving even more of the "human-needed" time and will be the future object of our focus. The fast evolution of artificial neuronal networks could provide the desired solution.

Detection of the lesion from MRI is a crucial step not only in the diagnosis of cortical ischemia but also in other pathologies as multiple sclerosis, focal cortical dysplasia, CADASIL, etc. and our future goal is to tune our algorithm for use in those diseases as well.

The same situation is for the blood-brain barrier disruption as it is a phenomenon commonly seen in several other neurological diseases. With the absence of clear knowledge of its pathophysiology and its consequences, BBB disruption is still of high scientific interest. Therefore, we plan to use the pipeline established in this thesis for routine analysis of BBB disruption by contrast-agent MRI in our patients.

In the last part of the thesis, we have introduced and tested an algorithm pipeline for neuronal tract reconstruction. The pipeline will be used in our future work focused on monitoring variations in thalamocortical neuronal tracts after cerebral stroke with the aim to uncover pathophysiological processes leading to post-ischemic epilepsy.

8. References

Abbott, N. J. and Friedman, A. (2012) 'Overview and introduction: The blood-brain barrier in health and disease', *Epilepsia*, 53, pp. 1–6. doi: 10.1111/j.1528-1167.2012.03696.x.

Abdullahi, W., Tripathi, D. and Ronaldson, P. T. (2018) 'Blood-brain barrier dysfunction in ischemic stroke: targeting tight junctions and transporters for vascular protection', *American Journal of Physiology-Cell Physiology*, 315(3), pp. C343–C356. doi: 10.1152/ajpcell.00095.2018.

Abo-Ramadan, U. *et al.* (2009) 'Post-ischemic leakiness of the blood-brain barrier: A quantitative and systematic assessment by Patlak plots', *Experimental Neurology*. Elsevier Inc., 219(1), pp. 328–333. doi: 10.1016/j.expneurol.2009.06.002.

Ahmmed, G. U. and Malik, A. B. (2005) 'Functional role of TRPC channels in the regulation of endothelial permeability', *Pflugers Archiv European Journal of Physiology*, 451(1), pp. 131–142. doi: 10.1007/s00424-005-1461-z.

Allen, L. M. *et al.* (2012) 'Sequence-specific MR Imaging Findings That Are Useful in Dating Ischemic Stroke', *RadioGraphics*, 32(5), pp. 1285–1297. doi: 10.1148/rg.325115760.

Araque, A. and Navarrete, M. (2010) 'Glial cells in neuronal network function', *Philosophical Transactions of the Royal Society B: Biological Sciences*, 365(1551), pp. 2375–2381. doi: 10.1098/rstb.2009.0313.

Ashburner, J. and Friston, K. J. (2005) 'Unified segmentation', *NeuroImage*, 26(3), pp. 839–851. doi: 10.1016/j.neuroimage.2005.02.018.

Bagher-Ebadian, H. *et al.* (2011) 'Predicting Final Extent of Ischemic Infarction Using Artificial Neural Network Analysis of Multi-Parametric MRI in Patients with Stroke', *PLoS ONE*. Edited by Y. He, 6(8), p. e22626. doi: 10.1371/journal.pone.0022626.

Brott, T. *et al.* (1989) 'Measurements of acute cerebral infarction: a clinical examination scale.', *Stroke*, 20(7), pp. 864–870. doi: 10.1161/01.STR.20.7.864.

Brown, R. C. and Davis, T. P. (2002) 'Calcium Modulation of Adherens and Tight Junction Function', *Stroke*, 33(6), pp. 1706–1711. doi: 10.1161/01.str.0000016405.06729.83.

Castejón, O. J. (1984) 'Formation of transendothelial channels in traumatic human brain edema', *Pathology Research and Practice*, 179(1), pp. 7–12. doi: 10.1016/S0344-0338(84)80054-0.

Chassidim, Y. *et al.* (2013) 'Quantitative imaging assessment of blood-brain barrier permeability in humans', *Fluids and Barriers of the CNS*, 10(1), p. 9. doi: 10.1186/2045-8118-10-9.

Chenevert, T. L., Brunberg, J. A. and Pipe, J. G. (1990) 'Anisotropic diffusion in human white matter: Demonstration with MR techniques in vivo', *Radiology*, 177(2), pp. 401–405. doi: 10.1148/radiology.177.2.2217776.

Daneman, R. and Prat, A. (2015) 'The Blood–Brain Barrier', *Cold Spring Harbor Perspectives in Biology*, 7(1), p. a020412. doi: 10.1101/cshperspect.a020412.

Danjo, S. *et al.* (2013) 'Pentylentetrazole-induced loss of blood–brain barrier integrity involves excess nitric oxide generation by neuronal nitric oxide synthase', *Brain Research*, 1530, pp. 44–53. doi: 10.1016/j.brainres.2013.06.043.

Dastidar, P. *et al.* (2000) 'Volumetric measurements of right cerebral hemisphere infarction: use of a semiautomatic MRI segmentation technique', *Computers in Biology and Medicine*, 30(1), pp. 41–54. doi: 10.1016/S0010-4825(99)00022-0.

Desikan, R. S. *et al.* (2006) 'An automated labeling system for subdividing the human cerebral cortex on MRI scans into gyral based regions of interest', *NeuroImage*, 31(3), pp. 968–980. doi: 10.1016/j.neuroimage.2006.01.021.

Durukan, A. *et al.* (2009) 'Post-ischemic blood–brain barrier leakage in rats: One-week follow-up by MRI', *Brain Research*, 1280, pp. 158–165. doi: 10.1016/j.brainres.2009.05.025.

Friedman, A. (2011) 'Blood-brain barrier dysfunction, status epilepticus, seizures, and epilepsy: A puzzle of a chicken and egg?', *Epilepsia*, 52, pp. 19–20. doi: 10.1111/j.1528-1167.2011.03227.x.

Galovic, M. *et al.* (2018) 'Prediction of late seizures after ischaemic stroke with a novel prognostic model (the SeLECT score): a multivariable prediction model development and validation study', *The Lancet Neurology*. Elsevier Ltd, 17(2), p. 117. doi: 10.1016/S1474-4422(17)30404-0.

Glenn, G. R. *et al.* (2015) 'Quantitative assessment of diffusional kurtosis anisotropy', *NMR in Biomedicine*. John Wiley and Sons Ltd, 28(4), pp. 448–459. doi: 10.1002/nbm.3271.

Griffis, J. C., Allendorfer, J. B. and Szaflarski, J. P. (2016) 'Voxel-based Gaussian naïve Bayes classification of ischemic stroke lesions in individual T1-weighted MRI scans', *Journal of Neuroscience Methods*, 257, pp. 97–108. doi: 10.1016/j.jneumeth.2015.09.019.

Guo, D. *et al.* (2015) 'Automated lesion detection on MRI scans using combined unsupervised and supervised methods', *BMC Medical Imaging*. BioMed Central, 15, p. 50. doi: 10.1186/S12880-015-0092-X.

Hagmann, P. *et al.* (2006) 'Understanding Diffusion MR Imaging Techniques: From Scalar Diffusion-weighted Imaging to Diffusion Tensor Imaging and Beyond', *RadioGraphics*, 26(suppl_1), pp. S205–S223. doi: 10.1148/rg.26si065510.

Hjort, N. *et al.* (2008) 'MRI detection of early blood-brain barrier disruption: Parenchymal enhancement predicts focal hemorrhagic transformation after thrombolysis', *Stroke*, 39(3), pp. 1025–1028. doi: 10.1161/STROKEAHA.107.497719.

Hu, X. *et al.* (2017) 'Cerebral Vascular Disease and Neurovascular Injury in Ischemic Stroke', *Circulation Research*, 120(3), pp. 449–471. doi: 10.1161/CIRCRESAHA.116.308427.

Ito, K. L., Kim, H. and Liew, S.-L. (no date) 'A comparison of automated lesion segmentation approaches for chronic stroke T1-weighted MRI data Author Names and Affiliations'. doi: 10.1101/441451.

Ivens, S. *et al.* (2007) 'TGF- receptor-mediated albumin uptake into astrocytes is involved in neocortical epileptogenesis', *Brain*, 130(2), pp. 535–547. doi: 10.1093/brain/awl317.

Jacobs, M. A. *et al.* (2000) 'Unsupervised segmentation of multiparameter MRI in experimental cerebral ischemia with comparison to T2, diffusion, and ADC MRI parameters and histopathological validation', *Journal of Magnetic Resonance Imaging*, 11(4), pp. 425–437. doi:

10.1002/(SICI)1522-2586(200004)11:4<425::AID-JMRI11>3.0.CO;2-0.

Jensen, J. H. and Helpern, J. A. (2010) 'MRI quantification of non-Gaussian water diffusion by kurtosis analysis', *NMR in Biomedicine*, 23(7), pp. 698–710. doi: 10.1002/nbm.1518.

Kala, D. *et al.* (2017) '/GD-Tracker/ A software for blood-brain barrier permeability assessment', *Lekar a Technika*, 47(2), pp. 43–48.

Lansberg, M. G. *et al.* (2001) 'Evolution of apparent diffusion coefficient, diffusion-weighted, and T2-weighted signal intensity of acute stroke', (April), pp. 637–644.

Li, X. *et al.* (2016) 'The first step for neuroimaging data analysis: DICOM to NIfTI conversion', *Journal of Neuroscience Methods*, 264, pp. 47–56. doi: 10.1016/j.jneumeth.2016.03.001.

Lu, H. *et al.* (2006) 'Three-dimensional characterization of non-gaussian water diffusion in humans using diffusion kurtosis imaging', *NMR in Biomedicine*, 19(2), pp. 236–247. doi: 10.1002/nbm.1020.

Maggio, N. *et al.* (2013) 'Treating seizures and epilepsy with anticoagulants?', *Frontiers in Cellular Neuroscience*, 7. doi: 10.3389/fncel.2013.00019.

Maier, O., Schröder, C., *et al.* (2015) 'Classifiers for ischemic stroke lesion segmentation: A comparison study', *PLoS ONE*, 10(12), pp. 1–16. doi: 10.1371/journal.pone.0145118.

Maier, O., Wilms, M., *et al.* (2015) 'Extra Tree forests for sub-acute ischemic stroke lesion segmentation in MR sequences', *Journal of Neuroscience Methods*. Elsevier B.V., 240, pp. 89–100. doi: 10.1016/j.jneumeth.2014.11.011.

Maier, O. *et al.* (2017) 'ISLES 2015 - A public evaluation benchmark for ischemic stroke lesion segmentation from multispectral MRI', *Medical Image Analysis*, 35, pp. 250–269. doi: 10.1016/j.media.2016.07.009.

Marchi, N. *et al.* (2007) 'Seizure-Promoting Effect of Blood?Brain Barrier Disruption', *Epilepsia*, 48(4), pp. 732–742. doi: 10.1111/j.1528-1167.2007.00988.x.

Minati, L., We, W. P. and Glarz, ˛ (2007) 'Physical Foundations, Models, and Methods of Diffusion Magnetic Resonance Imaging of the Brain: A Review', *Concepts Magn Reson Part A*, 30(5), pp. 278–307. doi: 10.1002/cmr.a.20094.

Mitchell, D. G. and Cohen, M. (2004) *MRI principles*. Saunders.

Mitra, J. *et al.* (2014) 'Lesion segmentation from multimodal MRI using random forest following ischemic stroke', *NeuroImage*. Elsevier B.V., 98, pp. 324–335. doi: 10.1016/j.neuroimage.2014.04.056.

Mokin, M. *et al.* (2017) 'ASPECTS (Alberta Stroke Program Early CT Score) Measurement Using Hounsfield Unit Values When Selecting Patients for Stroke Thrombectomy', *Stroke*, 48(6), pp. 1574–1579. doi: 10.1161/STROKEAHA.117.016745.

O'Brien, M. D. (1979) 'Ischemic cerebral edema. A review.', *Stroke*, 10(6), pp. 623–8. Available at: http://www.ncbi.nlm.nih.gov/pubmed/524402.

Rekik, I. *et al.* (2012) 'Medical image analysis methods in MR/CT-imaged acute-subacute ischemic stroke lesion: Segmentation, prediction and insights into dynamic evolution simulation models. A critical appraisal', *NeuroImage: Clinical*. The Authors, 1(1), pp. 164–178. doi: 10.1016/j.nicl.2012.10.003.

Rose, S. E. *et al.* (2004) 'Improving the prediction of final infarct size in acute stroke with bolus delay-corrected perfusion MRI measures', *Journal of Magnetic Resonance Imaging*, 20(6), pp. 941–947. doi: 10.1002/jmri.20216.

Satpathy, M. *et al.* (2004) 'Thrombin-induced phosphorylation of the regulatory light chain of myosin II in cultured bovine corneal endothelial cells', *Experimental Eye Research*, 79(4), pp. 477–486. doi: 10.1016/j.exer.2004.06.018.

Simard, J. M. *et al.* (2007) 'Isquemia Cerebral E Edema - Lancet Mar2007', pp. 1–11. Available at: papers2://publication/doi/10.1016/S1474-4422(07)70055-8.

Srinivasan, A. *et al.* (2006) 'State-of-the-Art Imaging of Acute Stroke 1 LEARNING OBJECTIVES FOR TEST 4 Recipient of a Certificate of Merit award for an education exhibit at the CME FEATURE', 48109, pp. 75–96. doi: 10.1148/rg.26si065501.

Stanimirovic, D. B. and Friedman, A. (2012) 'Pathophysiology of the Neurovascular Unit: Disease Cause or Consequence?', *Journal of Cerebral Blood Flow & Metabolism*, 32(7), pp. 1207–1221. doi: 10.1038/jcbfm.2012.25.

Stark, D. D. and Bradley, W. G. (1999) *Magnetic resonance imaging, Volume 1*. Mosby. Available at: http://books.google.ie/books/about/Magnetic_resonance_imaging.html?id=l3FrAAAAMAAJ&pgis=1 (Accessed: 3 April 2020).

Stejskal, E. O. and Tanner, J. E. (1965) 'Spin Diffusion Measurements: Spin Echoes in the Presence of a Time-Dependent Field Gradient', *The Journal of Chemical Physics*, 42(1), pp. 288–292. doi: 10.1063/1.1695690.

Stier, N. *et al.* (2015) 'Deep learning of tissue fate features in acute ischemic stroke', in *2015 IEEE International Conference on Bioinformatics and Biomedicine (BIBM)*. IEEE, pp. 1316–1321. doi: 10.1109/BIBM.2015.7359869.

Subbanna, N. K. *et al.* (2019) 'Stroke Lesion Segmentation in FLAIR MRI Datasets Using Customized Markov Random Fields', *Frontiers in Neurology*. Frontiers, 10, p. 541. doi: 10.3389/fneur.2019.00541.

van Swieten, J. C. *et al.* (1988) 'Interobserver agreement for the assessment of handicap in stroke patients.', *Stroke*, 19(5), pp. 604–607. doi: 10.1161/01.STR.19.5.604.

Tabesh, A. *et al.* (2011) 'Estimation of tensors and tensor-derived measures in diffusional kurtosis imaging', *Magnetic Resonance in Medicine*, 65(3), pp. 823–836. doi: 10.1002/mrm.22655.

Tiwari, Y. V. *et al.* (2017) 'Magnetic resonance imaging of blood–brain barrier permeability in ischemic stroke using diffusion-weighted arterial spin labeling in rats', *Journal of Cerebral Blood Flow and Metabolism*, 37(8), pp. 2706–2715. doi: 10.1177/0271678X16673385.

Tournier, J. D. *et al.* (2004) 'Direct estimation of the fiber orientation density function from diffusion-weighted MRI data using spherical deconvolution', *NeuroImage*, 23(3), pp. 1176–1185. doi: 10.1016/j.neuroimage.2004.07.037.

Tournier, J. D. *et al.* (2019) 'MRtrix3: A fast, flexible and open software framework for medical image processing and visualisation', *NeuroImage*. Elsevier Ltd, 202(January), p. 116137. doi: 10.1016/j.neuroimage.2019.116137.

Tournier, J. D., Calamante, F. and Connelly, A. (2007) 'Robust determination of the fibre

orientation distribution in diffusion MRI: Non-negativity constrained super-resolved spherical deconvolution', *NeuroImage*, 35(4), pp. 1459–1472. doi: 10.1016/j.neuroimage.2007.02.016.

Vezzani, A., Friedman, A. and Dingledine, R. J. (2013) 'The role of inflammation in epileptogenesis', *Neuropharmacology*, 69, pp. 16–24. doi: 10.1016/j.neuropharm.2012.04.004.

Wasserthal, J., Neher, P. F. and Maier-Hein, K. H. (2018) 'Tract orientation mapping for bundle-specific tractography', *Lecture Notes in Computer Science (including subseries Lecture Notes in Artificial Intelligence and Lecture Notes in Bioinformatics)*. Springer Verlag, 11072 LNCS, pp. 36–44. Available at: http://arxiv.org/abs/1806.05580 (Accessed: 8 April 2020).

Wasserthal, J., Neher, P. and Maier-Hein, K. H. (2018) 'TractSeg - Fast and accurate white matter tract segmentation', *NeuroImage*. Academic Press Inc., 183, pp. 239–253. doi: 10.1016/j.neuroimage.2018.07.070.

Zimmermann, A., Domoki, F. and Bari, F. (2008) 'Seizure-Induced Alterations in Cerebrovascular Function in the Neonate', *Developmental Neuroscience*, 30(5), pp. 293–305. doi: 10.1159/000142735.

A. List of Abbreviations

Medical abbreviations

MRI	Magnetic resonance
CT	Computer tomography
NIHSS	National Institute of Health Stroke Scale
mRS	Modified Ranking Scale
ACPECTS	Alberta Stroke Program Early CT Score
FPT	Fronto-pontine tract
ILF	Inferior longitudinal fasciculus
CSF	Cerebrospinal fluid
BBB	Blood-brain barrier
HT	Hemorrhagic transformation
WM/GM	White/Grey matter
CBF	Cerebral blood flow

Magnetic resonance sequences and parameters

T1w	T1 weighted
T2w	T2 weighted
FLAIR	Fluid Attenuation Inversion Recovery
DWI	Diffusion Weighted Imaging
DTI	Diffusion Tensor Imaging
SWI	Susceptibility Weighted Imaging
Gd	Gadolinium
TE	Echo time
FA	Flip angle
TR	Repetition time

Other symbols and abbreviations

IQR	Inter-quartile range
Voxel	Volumetric element (3D pixel)
FCNN	Fully convolutional neural network
fODF	Fiber Orientation Density Function
TOM	Tract Orientation Mapping
VOI	Volume of interest
FA	Fraction anisotropy
MD	Mean diffusivity
KFA	Kurtosis fraction anisotropy
MK	Mean kurtosis

Krad	Radial kurtosis
Kax	Axial kurtosis
TP	Number of true positive
P	Number of positive
FP	Number of false positive
S_{DWI}	DWI signal
S_0	Baseline signal measured with b=0
ADC	Apparent diffusion coefficient
AKC	Apparent kurtosis coefficient
b	Strength of effect of diffusion on tissue
$K_{1,2,3}$	Eigenvectors of diffusion kurtosis tensor
$\lambda_{1,2,3}$	Eigenvectors of diffusion tensor
$\Delta I(x,y,z)$	Intensity difference between pre- and post-contrast images
I_{post}	Post contrast image intensity
I_{pre}	Native image intensity
I_E	Normalization value for eyeball
I_V	Normalization value for vessel

B. List of Figures and Tables

Figure 1. MRI sequences most commonly used for the examination of cerebral ischemia 15
Figure 2. Scheme of inversion recovery method 17
Figure 3. Diffusion-weighted image and its metrics 19
Figure 4. Histogram of intensities of lesional (ischemic) and non-lesional tissue 23
Figure 5. Scheme of the proposed algorithm for detection of the ischemic lesion 24
Figure 6. Demonstration of segmentation and brain extraction technique 26
Figure 7. A precise atlas of cortical structures is used for parcellation in our pipeline 27
Figure 8. Usage of brain parcellation for improvement of brain extraction 28
Figure 9. Distributions of MR image intensities for lesional and non-lesional tissue 29
Figure 10. Manual preselection of part of the brain 29
Figure 11. Resulting segmentation of ischemic lesional tissue using proposed algorithm 30
Figure 12. Comparison of the proposed method with manual delineation 31
Figure 13. Clinical characteristics of 243 recruited patients 33
Figure 14. Image of lesional tissue was further parcellated 36
Figure 15. Size of the ischemic lesion in 175 patients 37
Figure 16. Correlation of volume of FLAIR and DWI regions 37
Figure 17. Our data shows time dynamics in the volume of defined VOIs in 11 patients 39
Figure 18. Proposed algorithm for detection and assessment of BBB impairment 42
Figure 19. Manual selection of eyeball and vessel and corresponding histograms 44
Figure 20. Detection of blood-brain barrier disruption by the proposed algorithm 45
Figure 21. Correlation between the volume of ischemic lesion and of BBB impairment 48
Figure 22. Image of lesional tissue was further parcellated (copy of Figure 15) 48
Figure 23. Distribution of the Extravasated Gd into different brain regions 49
Figure 24. Metrics of diffusion-weighted image 53
Figure 25. Signal decay curve from white matter tissue 56
Figure 26. Bundle of 5000 fibers as a representation of cerebrospinal neuronal tract 58
Figure 27. Scheme of algorithm for analysis of variations in white matter neuronal tracts 59
Figure 28. List of commands used in the algorithm for analysis of white matter tracts 61
Figure 29. Diffusion metrics of a patient with cerebral ischemia 63
Figure 30. Result of proposed pipeline applied at a patient with cerebral ischemia 64

Figure 31. Reconstruction of right fronto-pontine white matter tract 65
Figure 32. fODF peaks example 67
Figure 33. An artificial obstacle in the shape of a “wall” in the trajectory of the tract 68
Figure 34. TractSeg behavior during the reconstruction of fronto-pontine tract 69
Figure 35. Reconstruction of fronto-pontine tract 70
Figure 36. Demonstration of TractSeg behavior in several scenarious 72

Table 1. Number of patients selected for the study of ischemic lesion 35
Table 2. Number of patients selected for the study of blood-brain barrier impairment 47

C. Author's publications

C.1. Publications related to the thesis topic

C.1.1. Journal publications

[1] Svoboda, J; Litvinec, A; Kala, D; Pošusta. A; Vávrová, L; Jiruška, P; Otáhal, J. Strain differences in intraluminal thread model of middle cerebral artery occlusion in rats. *Physiological Research.* 2018, pp. 37–48. doi: 10.33549/physiolres.933958.

[2] Kala, D.; Svoboda, J; Litvinec, A; Pošusta, A; Lisý, J; Šulc, V; Tomek, A; Marusič, P, Jiruška, P, Otáhal, J. /GD-Tracker/ A software for blood-brain barrier permeability assessment. *Clinician and Technology.* 2017, 47(2), 43-48. ISSN 0301-5491.

[3] Janský, P., Růžičková, T., Olšerová, A., Reichl, J., Vosko, M., Šťovíčková, L., Paupasová-Schwabová, J., Šulc, V., Kalina, A., Magerová, H., Kala, D., et al. Occurrence and risk factors of unprovoked epileptic seizures in ischaemic stroke patients. *Česká a Slov Neurol a Neurochir.* 2020, 83/116:278–284.

[4] Kala, D., Šulc, V., Olšerová, A., Svoboda, J., Prysiazhniuk, Y., Pošusta, A., Kynčl, M., Šanda, J., Tomek, A., Otáhal, J. Evaluation of blood-brain barrier integrity by the analysis of dynamic contrast-enhanced MRI - a comparison of quantitative and semi-quantitative methods. *Physiological Research.* 2022 (accepted manuscript).

C.1.2. Conference and workshop publications

[1] Kala, D.; Pošusta, J; Šulc, V; Jánský, P; Tomek, A; Marusič, P, Jiruška, P, Otáhal, J. MRI maturation of brain ischemic tissue in human patients after stroke. In: Neuroscience Congress - Chicago, 2019 (abstract + poster)

[2] Kala, D.; Svoboda, J; Pošusta, A; Lisý, J; Šulc, V; Jánský, P; Tomek, A; Marusič, P, Jiruška, P, Otáhal, J. Parameters suitable as biomarker of postischemic epileptogenesis. In: 13th European Congress on Epilepsy - Wien. The International League Against Epilepsy, 2018. (abstrakt + poster)

[3] Kala, D.; Svoboda, J; Litvinec, A; Pošusta, A; Lisý, J; Šulc, V; Tomek, A; Marusič, P, Jiruška, P, Otáhal, J. Quantification of blood-brain barrier impairment as biomarker of epileptogenesis. In: 32nd International Congress on Epilepsy - Barcelona. The International League Against Epilepsy, 2017. (abstract + poster)

[4] Kala, D.; Svoboda, J; Litvinec, A; Pošusta, A; Lisý, J; Šulc, V; Tomek, A; Marusič, P, Jiruška, P, Otáhal, J. Detection of blood-brain barrier permeability impairment after stroke. In: 12th European Congress for Stereology and Image Analysis 2017. Ljubljana: International Society for Stereology, 2017. (abstract + poster)

[5] Kala, D.; Svoboda, J; Litvinec, A; Pošusta, A; Lisý, J; Šulc, V; Tomek, A; Marusič, P, Jiruška, P, Otáhal, J. Blood-brain barrier disruption after cerebral ischemia spatially exceed ischemic core. In: The Eleventh Conference of the Czech Neuroscience Society. Praha: Czech Neuroscience Society, 2017. (abstract + poster)

[6] Kala, D.; Svoboda, J; Litvinec, A; Pošusta, A; Lisý, J; Šulc, V; Tomek, A; Marusič, P, Jiruška, P, Otáhal, J. Rozsah poškození hematoencefalické bariery po cévní mozkové příhodě. In: 31. český a slovenský neurologický sjezd, 29. česko-slovenský epileptologický sjezd. Praha: Česká lékařská společnost J. E. Purkyně, 2017. ISSN 1802-4041. (abstrakt + poster)

[7] Kala, D., Olšerová, A., Šanda, J., Prysiazhniuk, Y., Svoboda, J., Kynčl, m., Tomek, A., Otáhal, J. Advanced MRI protocol for diagnosis and long-term monitoring of brain impairment in CADASIL patients. In The 13th Conference of the Czech Neuroscience Society, Prague, 2021 (abstract + poster)

[8] Kala, D., Svoboda, J., Prysiazhniuk, Y., Profantová, N., Kalina, A., Šanda, J., Marusič, P., Kynčl, M., Otáhal, J. Diffusion kurtosis parameters show higher difference between focal cortical dysplasia and healthy tissue than standard diffusion parameters. In The 14th European Epilepsy Congress, Geneva, 2022 (abstract + poster)

C.1.3. Preprints and extended versions

C.2. Publications not related to the thesis topic

C.2.1. Journal publications

[1] Kala, D; Krajca, V; Schaabova, H; Lhotska, L; Gerla, V. Optimal Parameters of Adaptive Segmentation for Epileptic Graphoelements Recognition. Radioengineering, 2017

[2] Kapoor, S., Kala, D., Svoboda, J., Brnoliakova, Z., Otáhal, J. The Effect of Sulphoraphane on Brain Glucose Uptake during Neonatal Hypoxic-Ischemic Encephalopathy in Newborn Rats. *European Pharmaceutical Journal*, 2021, 68(1), pp. 136–138. doi: 10.2478/afpuc-2021-0013.

[3] Daněk, J., Danačíková, Š., Kala, D., Svoboda, J., Kapoor, S., Pošusta, A., Folbergrová, J., Tauchmanová, K., Mráček, T., Otáhal, J. Sulforaphane Ameliorates Metabolic Changes Associated With Status Epilepticus in Immature Rats. *Frontiers in Cellular Neuroscience,* 16. 2022. doi: 10.3389/fncel.2022.855161.

D. Curriculum Vitae

David Kala finished his master's study in 2016 at the Faculty of Biomedical Engineering, Czech Technical University in Prague with a thesis called *Metody pro adaptivní segmentaci EEG signálů*.

Since 2016 he is a Ph.D. student at the Faculty of electrical engineering, CVUT in Prague, and at the Institute of Physiology, Czech Academy Of Sciences. Since 2020 he is a member of the Prague Epilepsy Research Center as neuroimaging analyst.

His scientific field is experimental neurology with a focus on epileptology and neurovascular diseases. He is an expert in image analysis of human brain data (MRI, CT, microscopy), processing of MRI diffusion data, tractography, and brain connectivity. He is also experienced in in-vivo microscopy of living animals and subsequent processing of 2D and 3D microscopic images.

He had two internships (in 2018 and 2020) at Liverpool Magnetic Resonance Imaging Centre, the University of Liverpool with a focus on tractography and its use for the identification of brain neuronal tracts and assessment of brain structural connectivity.

During his studies, he published seven scientific papers six in impacted journals (twice as the first author) and one in peer-reviewed journal (as the first author). He also attended several international and local congresses such as an annual poster presentation at the European/International Congress on Epileptology in 2016 - 2018, and 2022, a poster presentation at the Annual Meeting of Society for Neuroscience SFN in 2019, poster presentation at the International Society for Stereology Meeting, 2017, two oral presentations at Czech Physiological days in 2019 and the poster presentation at Czech Neuroscience meeting in 2021. He received the Best clinical research poster award at the 13th European Congress on Epileptology in Vienna, 2018.

In 2021 he was the main organizer of a scientific symposium *Diagnostic tools for imaging animal models.*